Karlsruhe Institute of Technology

Karlsruhe Institute of Technology
Fakultät für Physik
Physikalisches Institut

Development of a tunable transmon qubit in microstrip geometry

Entwicklung eines stimmbaren Transmon-Qubits in Mikrostripgeometrie

Master thesis of

Jochen Braumüller

12th December 2013

Reviewer:	Prof. Dr. Alexey V. Ustinov
Second reviewer:	Prof. Dr. Gerd Schön
Advisor:	Dr. Martin Weides

Jochen Braumüller: jochen.braumueller@student.kit.edu

Erklärung

Ich versichere wahrheitsgemäß, die Arbeit selbstständig angefertigt, keine anderen als die angegebenen Quellen und Hilfsmittel benutzt zu haben, die wörtlich oder inhaltlich übernommenen Stellen als solche kenntlich gemacht zu haben und die Satzung der Universität Karlsruhe (TH) zur Sicherung guter wissenschaftlicher Praxis beachtet zu haben.

Jochen Braumüller

Contents

Chapter I Introduction

Information processing of present computers being based on classical binary bits is described using the language of classical Newtonian mechanics [DiV00]. Pioneers of quantum computation like Deutsch [Deu85] and Feynman [Fey82] were triggered by the thought, that computers obeying the laws of quantum mechanics could have much greater computational power since Newtonian mechanics appears as a special limit of quantum mechanics [DiV00].

While iterative tasks can not be performed faster using a quantum computer [Bea01], some others are indeed sped up exponentially such as Shor´s algorithm for factoring an n-digit number [Sho97] or other algorithms exploiting "quantum parallelism" [Deu85]. This promises to employ a quantum computer in several computation power intensive applications in science, industry and medicine, to be able to solve problems faster or even in the first place. In addition, there are certain tasks that can be realized on a quantum machine without having a classical counterpart such as quantum cryptography [Ben84], for instance.

The main building block of a quantum computer is called a qubit. In contrast to a classical bit which is either in state zero or one, the state of a qubit can be any superposition $a|0\rangle + b|1\rangle$ of its fundamental states, usually denoted as $|0\rangle$, $|1\rangle$. Therefore it is a quantum mechanical two-level system like a spin $1/2$ particle and its state is intuitively described as a certain point on the Bloch sphere. In that respect, the qubit is considered as an artificial atom.

In general, the state of a system consisting of n qubits is a superposition of 2^n eigenstates. A quantum gate accepts such a superposition state as its input and computes the corresponding output for each eigenstate simultaneously. This is the mentioned quantum parallelism.

A physical device is identified as a qubit by verifying the "five [...] requirements for the implementation of quantum computation" by D. DiVincenzo [DiV00]. Accordingly a qubit needs to be sufficiently controllable allowing to write, manipulate or readout its state and hold quantum information for a certain time.

The dynamics of a qubit is characterized by its coherence times. Since the qubit is weakly coupled to its environment, it will decohere after some time. This mechanism is very fundamental, since it constitutes the link between quantum and classical behaviour [DiV00]. A qubit can only serve as a useful unit for a quantum computer, if the relevant decoherence times are long enough to perform a computational operation. Fortunately, it was shown [Sho95], that quantum error correction during such an operation is possible and can be applied for quantum computation. This means that the decoherence times of the employed qubit need to be $10^4 - 10^5$ times [DiV00] the typical time for performing a single quantum gate operation, which corresponds to the time necessary for successful error correction. While this places still challenging requirements on the qubits´ coherence times, it is in contrast to the duration of the total computational operation, which is thereby not limited.

Due to the intriguing prospects of quantum computation in general and the strong demand for qubits with increased coherence times, a great variety of approaches to build physical devices operating in the quantum mechanical regime have emerged in the last 15 years. Among suggestions and realizations of quantum hardware in quantum optics [Kni01], magnetic resonance spectroscopy [Kan98] and quantum dot research [Los98], a promising technology for qubit realization is based on superconducting devices and the Josephson effect [Cla08].

The main types of superconducting qubits are flux, charge and phase qubit, with their designation indicating the good quantum number to distinguish the fundamental qubit states. Their key element is the Josephson tunnel junction, which is a weak link of two superconducting electrodes allowing Cooper pairs to tunnel coherently. A Josephson junction behaves similar to a superconducting LC-resonator which can be regarded as quantum mechanical oscillator having distinct energy levels. However, since the Josephson junction is non-linear, the energy levels are not equidistant and therefore certain levels can unambiguously be identified with the qubit eigenstates $|0\rangle$, $|1\rangle$.

Finding new approaches to implement qubits with enhanced performance to enable quantum error correction is the ultimate aim of present research. During the past 15 years, the coherence times of superconducting qubits increased exponentially [Dev13], corresponding to a Moore´s law progression. Major improvements in qubit performance could be achieved by combining the advantages of existing types and avoid dominant decoherence channels. Among more advanced innovations such as the quantronium [Vio02] or fluxonium [Man09], the transmon [Koc07] is the most promising candidate. While the simple charge qubit developed around 2000 had a lifetime in the range of 5 ns, a transmon embedded in a three-dimensional cavity reached a coherence time of up to $100\,\mu s$ [Rig12] in 2012.

Superconducting qubits are very promising, not only when it comes to high coherence times. Connectivity and control of the qubits is accomplished comparatively easy and a possible tunability guarantees high flexibility in application. Thinking of future quantum computation, scalability of the quantum circuit becomes important, which is given in the case of two-dimensional quantum integrated circuits as demonstrated in [Bar13].

In this work, a frequency tunable transmon qubit together with its manipulation and readout circuit is designed, simulated and prepared. The employed microstrip design pulls the electric field lines into the low-loss substrate material due to a backside metallization and reduces the field strength at surface dielectrics. This promises an increased relaxation time of the investigated transmon. A similar approach but without tuning was taken by Sandberg *et al.* [San13].

A decisive advancement of the conventional charge qubit namely the insertion of a large shunt capacitance in parallel to the qubit´s Josephson junction shifts the operation point of the transmon into the phase regime. The qubit in this configuration is insensitive to charge noise not only at certain charge “sweet spots”. This leads to strongly enhanced dephasing times which is crucial when it comes to quantum error correction and the demand for a scalable quantum system.

Novel features of the microstrip transmon investigated in this work are the tunability, enabling frequency selective coupling to the readout resonator as well as flexibility concerning the measurement regime. The multi-plexed chip geometry allows for simultaneous qubit readout.

Josephson tunnel junctions are prepared using aluminum sputter deposition and a cross junction technique in a two-step optical lithography process, ensuring robustness of the fabrication process. Transport characterization is performed at room temperature as well as in a cryogenic environment.

Corresponding spectroscopic qubit measurements are carried out in a dilution refrigerator.

Chapter II Theory

1 The Josephson junction

The key element of the transmon investigated in this work is the Josephson tunnel junction. The effect of a current flowing across the junction without giving rise to a voltage drop, even though the two electrodes of the junction are not in direct contact, is strongly based on the properties of superconductivity.

The following sections give some important features of the microscopic theory of superconductivity, the Josephson equations are derived from a microscopic point of view and a simple model is presented to understand the characteristics of a Josephson junction.

1.1 Superconductivity

In 1911, H. Kammerlingh-Onnes measured the temperature dependence of the electrical resistivity of mercury. While decreasing the temperature, he found that the resistivity drops abruptly to exactly zero at a certain temperature [Kam11]. This phenomenon was later called superconductivity.

The property of undergoing such a phase transition from the normal to the superconducting state at a characteristic critical temperature can be observed in a wide range of metals. Besides the most striking effect of vanishing electrical resistance, superconductors behave as a perfect diamagnet when placed inside a magnetic field, which is referred to as the Meissner-Ochsenfeld effect.

The common theory of superconductivity requires a net attractive potential between electrons close to the Fermi surface of a conductor. Although the direct Coulomb interaction between two electrons is repulsive, ions as well as the other $N-2$ electrons in an N-electron system move in response to the electronic motion which leads to an "overscreening" of the Coulomb interaction [AsMe76]. Within the so called weak coupling theory, this effect is possible when the energy difference of two electrons is less or of the order of $\hbar\omega_D$ which is a typical phonon energy and ω_D the Debye frequency.

This net attractive interaction would be far too weak to lead to a bound state of two isolated electrons. L. N. Cooper however showed, that in the presence of a filled Fermi sphere, the formation of a bound state, a Cooper pair, is possible no matter how small the attraction might be [Coo56]. This is due to the Pauli exclusion principle.

Within the microscopic theory of superconductivity (BCS theory), developed by Bardeen, Cooper and Schrieffer [Bar57], all electrons within the region of $\pm\hbar\omega_D$ around the Fermi sphere are assumed to form Cooper pairs. Due to the bosonic nature of a Cooper pair, consisting of two electrons with opposite spin and momentum, each pair can occupy the same state. In analogy to a Bose-Einstein condensation, all Cooper pairs in a superconductor condensate into a common ground state which is called the BCS ground state and can be described by a single macroscopic wave function

$$\Psi(\vec{r}) = \Psi_0 e^{i\varphi(\vec{r})}. \tag{1}$$

Its absolute square $|\Psi_0|^2$ corresponds to the Cooper pair density while $\varphi(\vec{r})$ is the associated collective phase of the wave function.

The absolute value of the wave function $|\Psi|$ also appears in the phenomenological theory of superconductivity introduced by V. Ginzburg and L. Landau where it is called order parameter [Gin50]. According to the theory, the transition of a normal conductor to its superconducting state at a critical temperature T_c, is described as a second order phase transition from a thermodynamic point of view. This corresponds to a discontinuity of the specific heat at the phase transition, as is the case for instance at the second order phase transition of a paramagnet to a ferromagnet.

Another intriguing property of superconductivity is the quantization of magnetic flux, which is induced by the persistent current flowing in a superconducting ring. This can easily be derived using the London equation [Ann11]

$$\vec{j} \propto \vec{A}, \tag{2}$$

with $\vec{j}$ the current density and $\vec{A}$ the vector potential. From the claim of local gauge invariance, the vector potential is modified according to equation (3), employing the phase φ from equation (1).

$$\vec{A} \rightarrow \vec{A} + \frac{\hbar}{2e}\nabla\varphi \tag{3}$$

One now chooses an integration path along a closed loop in the superconducting ring well in excess of the penetration depth, which is a measure for the thickness of the surface layer of a superconductor, where screening currents are flowing. Thus the current density vanishes everywhere on the integration path.

$$0 = \oint \vec{A}\cdot \mathrm{d}\vec{r} + \frac{\hbar}{2e}\oint \nabla\varphi \cdot \mathrm{d}\vec{r} \tag{4}$$

Using Stokes´ theorem and the definition of magnetic flux Φ, the first term of equation (4) reduces to

$$\oint \vec{A}\cdot \mathrm{d}\vec{r} = \int \nabla \times \vec{A}\cdot \mathrm{d}\vec{S} = \int \vec{B}\cdot \mathrm{d}\vec{S} = \Phi, \tag{5}$$

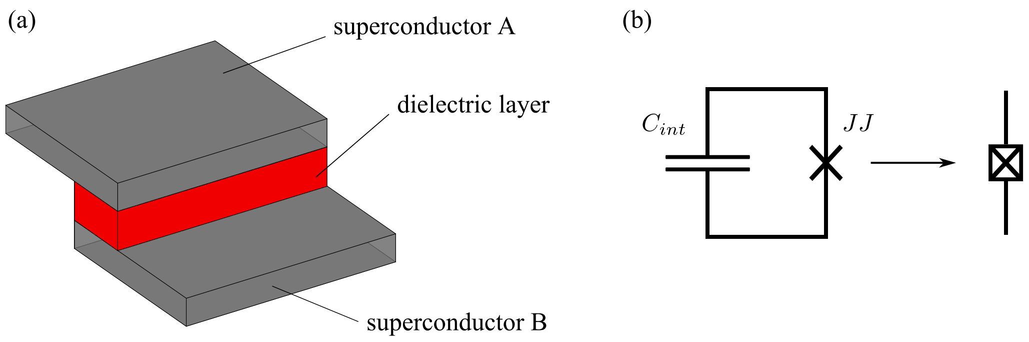

Figure 1: (a) Schematic of a Josephson tunnel junction. Two superconductors are separated by a dielectric layer which appears as a weak link. (b) Circuit model of a Josephson junction. Intrinsic capacitance due to the electrode plates and the ideal tunnel element can be regarded to be connected in parallel. A short notation is shown on the right.

$\vec{B}$ being the magnetic induction through an area S. Performing the scalar product, equation (4) gives

$$0 = \Phi + \frac{\hbar}{2e} \oint \mathrm{d}\varphi. \tag{6}$$

Since the wave function is single valued, φ has to be periodic in 2π and one can write

$$\Phi = \frac{\hbar}{2e} 2\pi n = \frac{h}{2e} n = n\Phi_0, \quad n \in \mathbb{Z}. \tag{7}$$

Therefore the flux through the superconducting ring can only take integer values of the flux quantum Φ_0, which is given by

$$\Phi_0 = \frac{h}{2e}. \tag{8}$$

It is notable that the charge $2e$ of a Cooper pair rather than the charge of a single electron occurs in the denominator, showing that the supercurrent is carried by pairs of electrons.

1.2 The Josephson equations

A Josephson tunnel junction consists of two superconductors being close together but separated by a thin insulating dielectric layer. It is schematically depicted in figure 1(a). The wave functions of the two superconductors partly penetrate into the dielectric layer due to the proximity effect [Sch97] and therefore can interfere, which corresponds to tunnelling of electrons through the barrier. Since the dielectric does not short the adjacent superconductors and at the same time enables interference of the wave functions, one calls it a weak link. According to equation (1), both superconductors A and B can be described by a single wave function, respectively. One has

$$\Psi_A(\vec{r}) = \Psi_0 e^{i\varphi_A(\vec{r})}, \quad \Psi_B(\vec{r}) = \Psi_0 e^{i\varphi_B(\vec{r})} \tag{9}$$

under the assumption of equal Cooper pair densities.

In 1962, B. Josephson predicted theoretically two fascinating effects to occur at such a tunnel junction when its electrodes are in the superconducting state. Therefore it is called a Josephson tunnel junction. These effects will be derived following the analysis of [Dev95].

As depicted in figure 1(b), a Josephson tunnel junction can be regarded as an ideal tunnel element connected in parallel with a capacitor. The capacitive contribution emerges from the parallel arrangement of the two electrode plates. Assuming that Cooper pairs with charge $-2e$ tunnel through the Josephson junction, the charge $\hat{Q}(t)$ of electrons having passed is

$$\hat{Q}(t) = -2e\hat{n}(t) \tag{10}$$

with $\hat{n}$ being the number operator of Cooper pairs which have tunnelled. The respective Hamiltonian $\hat{H}_C$ for the energy on the capacitor is

$$\hat{H}_C = \hat{Q}\hat{U} = -2e\hat{n}\hat{U}, \tag{11}$$

with $\hat{U}$ the voltage operator. For a quantum mechanical description, all relevant quantities are treated as operators.

According to [Dev95], one can write down a coupling Hamiltonian $\hat{H}_J$ for electrons tunnelling through the Josephson junction, given in equation (12). E_J is called the Josephson energy and it will turn out to be a characteristic macroscopic parameter to describe the properties of the Josephson junction.

$$\hat{H}_J = -\frac{E_J}{2}\sum_{n=-\infty}^{+\infty}\left[|n\rangle\langle n+1| + |n+1\rangle\langle n|\right] \tag{12}$$

Equation (12) can be motivated as follows: The summation is carried out over projection operators that either increment or decrement the number of Cooper pairs. This exactly corresponds to the event of a Cooper pair tunnelling through the barrier.

To evaluate the coupling Hamiltonian $\hat{H}_J$, a phase δ is introduced. It turns out that its corresponding operator $\hat{\delta}$ is the canonical conjugate of the number operator $\hat{n}$. This allows to write the new basis states $|\delta\rangle$ as a Fourier transform according to equation (13).

$$|\delta\rangle = \sum_n e^{in\delta}|n\rangle \tag{13}$$

Likewise, because of the periodicity of δ, it is

$$|n\rangle = \frac{1}{2\pi}\int_0^{2\pi} \mathrm{d}\delta e^{-in\delta}|\delta\rangle. \tag{14}$$

Plugging into equation (12), one gets the coupling Hamiltonian in phase basis.

$$\begin{aligned}
\hat{H}_J &= -\frac{E_J}{2}\frac{1}{(2\pi)^2}\sum_n \int_0^{2\pi} \mathrm{d}\delta \int_0^{2\pi} \mathrm{d}\delta' \left[e^{-in\delta}|\delta\rangle e^{i(n+1)\delta'}\langle\delta'| + e^{-i(n+1)\delta'}|\delta'\rangle e^{in\delta}\langle\delta|\right] \\
&= -\frac{E_J}{2}\frac{1}{(2\pi)^2}\int_0^{2\pi} \mathrm{d}\delta \int_0^{2\pi} \mathrm{d}\delta' \left[e^{i\delta} + e^{-i\delta}\right] 2\pi\delta(\delta-\delta')|\delta\rangle\langle\delta| \\
&= -\frac{E_J}{2}\frac{1}{2\pi}\int_0^{2\pi} \mathrm{d}\delta 2\cos\delta|\delta\rangle\langle\delta| \\
&= -E_J\cos\hat{\delta} \qquad (15)
\end{aligned}$$

In the last step, the operator representation

$$e^{i\hat{\delta}} = \frac{1}{2\pi}\int_0^{2\pi} \mathrm{d}\delta e^{i\delta}|\delta\rangle\langle\delta| \qquad (16)$$

was introduced. Using equation (13), one can verify the relations

$$e^{i\hat{\delta}}|n\rangle = |n-1\rangle, \quad e^{-i\hat{\delta}}|n\rangle = |n+1\rangle. \qquad (17)$$

Noting that only periodic functions of $\hat{\delta}$ like the exponential function used in equation (16) have non-ambiguous meaning, one can write a commutation relation for the two canonical conjugated operators:

$$\left[\hat{\delta}, \hat{n}\right] = i \qquad (18)$$

Using Heisenberg´s equation of motion and related algebraic relations allows to calculate the time evolution of the phase operator $\hat{\delta}$:

$$\frac{\mathrm{d}}{\mathrm{d}t}\hat{\delta} = \frac{1}{i\hbar}\left[\hat{\delta}, \hat{H}\right] = -\frac{1}{\hbar}\frac{\partial \hat{H}}{\partial \hat{n}} = \frac{2e}{\hbar}\hat{U} \qquad (19)$$

Evaluating similarly the current operator $\hat{I}$ gives

$$\begin{aligned}
\hat{I} &= \frac{\mathrm{d}}{\mathrm{d}t}\hat{Q} = -2e\frac{\mathrm{d}\hat{n}}{\mathrm{d}t} \\
&= -2e\frac{1}{i\hbar}\left[\hat{n}, \hat{H}\right] = \frac{2e}{\hbar}\frac{\partial \hat{H}}{\partial \hat{\delta}} = \frac{2e}{\hbar}E_J\sin\hat{\delta} \\
\Rightarrow \hat{I} &= I_c\sin\hat{\delta}. \qquad (20)
\end{aligned}$$

In both cases the full Hamiltonian $\hat{H} = \hat{H}_C + \hat{H}_J$ of the system from equations (11) and (15) is employed.

Equation (20) is the first, or dc-Josephson equation which states, that a Josephson junction can sustain a zero voltage supercurrent below the critical current I_c. If the current exceeds I_c, a voltage drop occurs which corresponds to the time evolution of the phase, as given in equation (19).

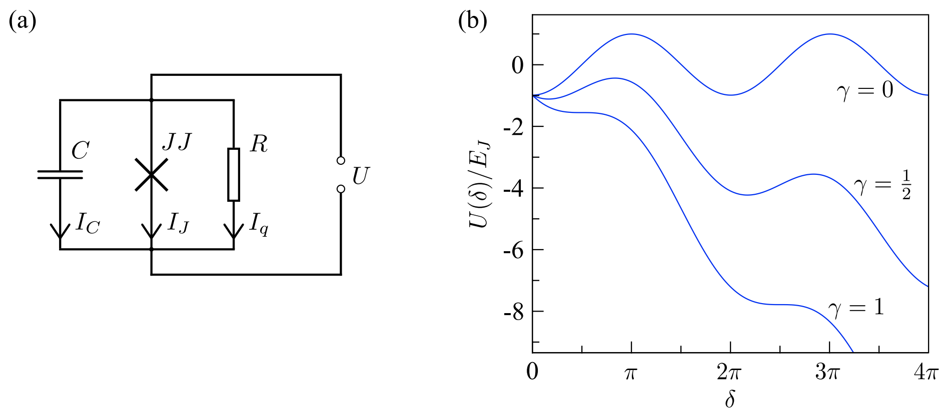

Figure 2: (a) Equivalent circuit diagram showing the RCSJ model of a Josephson tunnel junction. The cross symbolizes the ideal Josephson junction while C includes both, external and intrinsic Josephson capacitance. (b) "Washboard" potential $U(\delta)/E_J$ with respect to the phase difference δ for different bias currents γ. For $T = 0$ and for small currents ($\gamma \approx 0$), a virtual phase particle is trapped in one of the potential wells and the voltage U across the junction is zero. This is called the superconducting state. With increasing current, the potential gets tilted and for $I = I_c$ ($\gamma = 1$), the virtual particle can run down the "washboard" since the derivative of the potential is always non-positive. This corresponds to a voltage drop across the junction and is called the dissipative state [Dev95], see section 1.4.

It is crucial to note that the phase δ in the above equations corresponds to the phase difference $\Delta\varphi$ of the wave functions of the adjacent superconductors. It is

$$\Delta\varphi = \varphi_A - \varphi_B. \tag{21}$$

The phase difference $\Delta\varphi$ is not unambiguously defined for a certain physical situation since it is not a gauge-invariant quantity. To be explicitly related to physical quantities, it is replaced by the gauge-invariant phase δ.

Equation (20) also gives the definition of the critical current in terms of the Josephson energy E_J

$$I_c = \frac{2e}{\hbar} E_J = \frac{2\pi}{\Phi_0} E_J \tag{22}$$

where again the flux quantum Φ_0 from equation (8) enters.

The Josephson equations can also be obtained by a semi-phenomenological approach based on the Ginzburg-Landau theory. Derivations were given by Feynman [Fey65] and Aslamazov and Larkin [Asl65].

The critical current I_c depends on the properties of the superconductors forming the Josephson junction as well as on the sheet resistance of the dielectric layer. Formulas to estimate I_c from microscopic quantities are given in section III.1.

1.3 Resistively and capacitively shunted junction model

The Resistively and Capacitively Shunted Junction (RCSJ) model was introduced by W. Stewart and D. McCumber [Ste68, McC68] to describe the current-voltage characteristic (IV-characteristic) of a Josephson tunnel junction. It uses the simple equivalent circuit shown in figure 2(a) which is valid for small junction dimensions when $\delta = \delta(t)$ is not a function of space.

According to Kirchhoff´s rules, the total current I which is flowing through the Josephson junction is

$$I = I_J + I_q + I_C = I_J + \frac{U}{R} + C\dot{U}. \tag{23}$$

For the quasi-particle current, which is a current of single electrons, it is assumed that R is a constant. The capacitance C in the displacement current I_C is a sum of the external capacitance C_{ext} and the intrinsic Josephson capacitance C_J.

Inserting the Josephson equations (19) and (20) into equation (23) yields a differential equation for the phase difference δ:

$$0 = -I + I_c \sin\delta + \frac{1}{R}\frac{\Phi_0}{2\pi}\dot{\delta} + C\frac{\Phi_0}{2\pi}\ddot{\delta} \tag{24}$$

Comparing equation (24), normalized to energy units, with the differential equation of a classical damped harmonic oscillator

$$0 = m\ddot{x} + D\dot{x} + \frac{\partial U(x)}{\partial x} \tag{25}$$

with particle mass m, damping constant D and potential $U(x)$, one can identify

$$m = C\left(\frac{\Phi_0}{2\pi}\right)^2, \tag{26}$$

$$D = \frac{1}{R}\left(\frac{\Phi_0}{2\pi}\right)^2 \tag{27}$$

and

$$\begin{aligned} \frac{\partial U(\delta)}{\partial \delta} &= \frac{I_c \Phi_0}{2\pi}\left(-\gamma + \sin\delta\right) \\ \Rightarrow U(\delta) &= E_J\left(-\gamma\delta - \cos\delta\right) \end{aligned} \tag{28}$$

using the definition (22) of the Josephson energy E_J and the current normalization $\gamma = \frac{I}{I_c}$. Therefore, the Josephson phase δ behaves as a virtual particle of mass m according to equation (26). Equation (28) gives the so-called “washboard” potential, which is plotted in figure 2(b) for different bias currents γ.

Solving equation (24) yields the angular resonance frequency ω of the Josephson junction. For small damping, it is

$$\omega^2 = \frac{1}{m}\frac{\partial^2 U}{\partial x^2} \to \frac{2\pi I_c}{\Phi_0 C}\cos\delta \tag{29}$$

using equations (26), (28). It is convenient to write

$$\omega^2 = \omega_p^2 \cos\delta = \omega_p^2\sqrt{1 - \sin^2\delta} = \omega_p^2\sqrt{1 - \gamma^2} \tag{30}$$

where the plasma frequency

$$\omega_p = \sqrt{\frac{2\pi I_c}{\Phi_0 C}} \tag{31}$$

is introduced. From equation (30) one can see that the resonance frequency ω of the Josephson junction decreases with increasing current γ.

Using the common formula for the resonance frequency of an LC-resonator

$$\omega^2 = \frac{1}{LC} \tag{32}$$

with inductance L and capacitance C, one can define the Josephson inductance L_J using equation (30) to be

$$L_J = \frac{1}{\omega^2 C} = \frac{\Phi_0}{2\pi I_c \cos\delta}. \tag{33}$$

It is obvious that the Josephson inductance is non-linear in the phase difference δ. This property is of fundamental importance for the Josephson junction to serve as the key element of a qubit.

It is important to note that the inductance given in equation (33) is not a geometric inductance describing the capability of a circuit to store magnetic energy but rather a kinetic inductance originating from the inertia of charge carriers.

Conveniently, the damping of a Josephson junction is described by the Stewart-McCumber parameter β_c. It is defined as the square of the quality factor Q of a parallel LC-resonator [TiSc91, Tin04]:

$$\beta_c^{1/2} = Q = \omega_p RC \tag{34}$$

1.4 Tunnelling of Cooper pairs and quasi-particles

Josephson junctions which are employed for qubits are required to work in the underdamped regime where $\beta_c > 1$. According to equation (34), this can be achieved with a high parallel resistance R and a large enough capacitance C.

For temperatures close to $T = 0$, in the absence of thermal processes, a typical current-voltage characteristic (I-V characteristic) of a strongly underdamped Josephson junction is plotted in figure 3(a). Figure 3(b) shows schematic energy diagrams for different voltages U across the junction.

i) Increasing the bias current from $I = 0$, the voltage across the Josephson junction remains zero. This is the superconducting state described by the first Josephson equation (20) where Cooper pairs tunnel through the barrier coherently. There are no quasi-particles, since all electrons are condensed in the superconducting condensate. In the "washboard" model from section 1.3, this corresponds to the virtual phase particle being trapped in one of the potential wells.

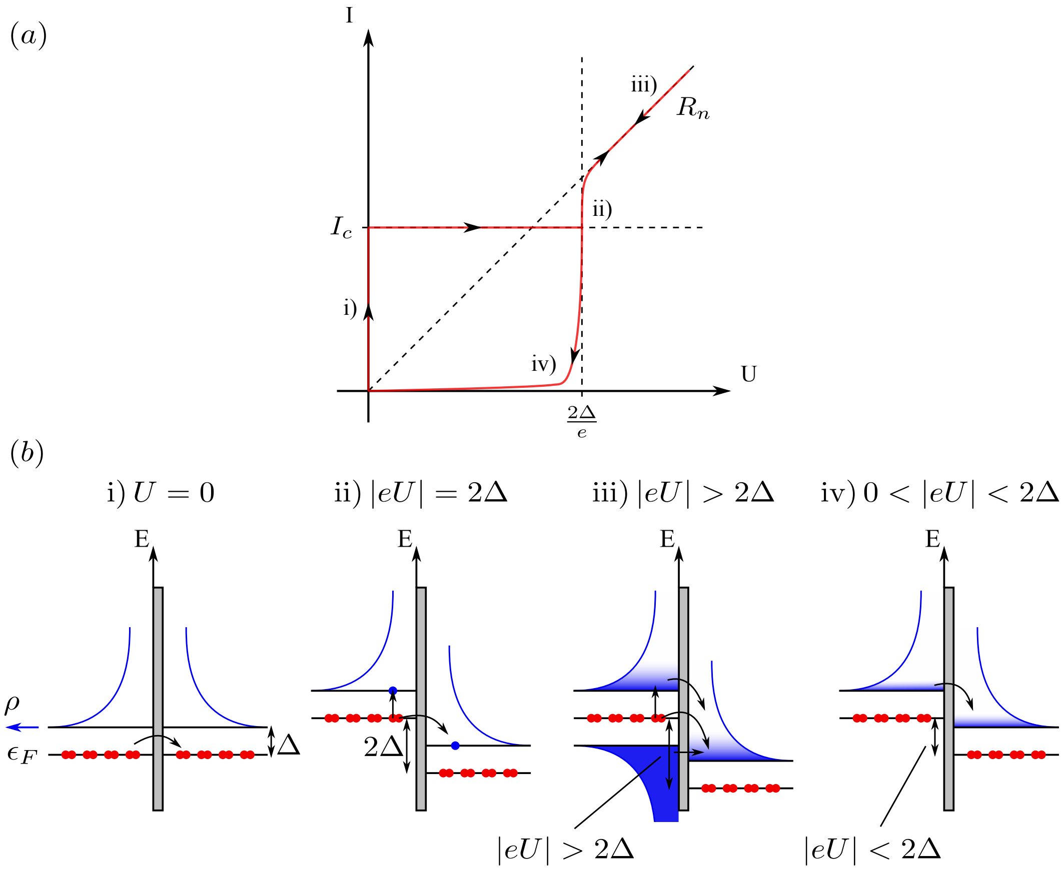

Figure 3: (a) Typical I-V characteristic of a current biased underdamped Josephson junction of electrodes with equal superconducting gap Δ. As explained in the text, a hysteresis appears. For voltages $eU \gg 2\Delta$, the junction shows ohmic behaviour with resistance R_n. (b) Schematic energy diagrams for different voltage regimes. The quasi-particle density of states ρ relative to the normal density of states is shown in blue, the barrier is depicted as a grey bar.

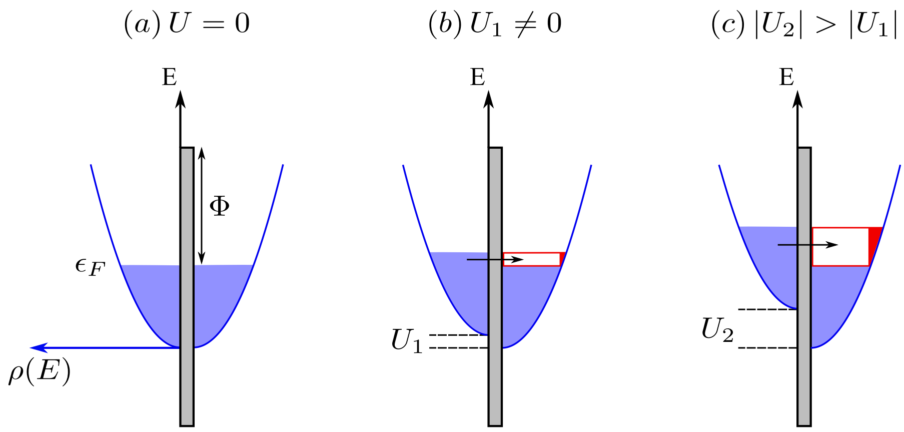

Figure 4: Schematic energy diagrams explaining the non-ohmic behaviour of the I-V characteristic of a tunnel junction for $U \gg \frac{2\Delta}{e}$. States below the Fermi level are coloured in blue, the finite barrier height is indicated. (a) For zero voltage, the net tunnelling rate vanishes. (b), (c) Free electron states available to scatter in are framed in red, red areas denote additional free states.

ii) When the bias current reaches the critical current I_c, the voltage jumps to the finite value $\frac{2\Delta}{e}$. Here the virtual phase particle runs down the "washboard" and the continuous change in phase leads to a voltage across the junction. Cooper pairs break up and the emerging quasi-particles tunnel through the barrier.

iii) A further increase in bias current leads to ohmic behaviour due to tunnelling of abundant free electrons.

iv) Reducing the bias current below I_c does not immediately lead to a vanishing voltage across the junction and a hysteresis opens up. In the "washboard" analogue this is due to the effect of inertia of the virtual phase particle. With its kinetic energy from running down the potential, it can overcome the potential wells appearing when tilting back the "washboard". The Josephson junction goes back in the zero voltage state when the bias current reaches the retrapping current $I_{re} \propto \beta_c^{-1/2}$ [Tin04]. For a strongly underdamped Josephson junction, I_{re} practically vanishes. The current in this domain is carried by quasi-particles, being not yet recondensed.

1.5 Tunnelling of electrons in a tunnel junction

For bias currents $I \gg I_c$, the current through a tunnel junction is not linear in the applied voltage. According to [Bri70, Sim63, Kai10],

$$I \propto \int \mathrm{d}E \rho(E)\rho(E - eV)P(E_x)\left[f(E) - f(E - eV)\right]. \tag{35}$$

ρ denotes the density of states in the electrodes, f is the usual Fermi distribution function and $P(E_x)$ is the tunnelling probability in x-direction which is chosen to be perpendicular to the barrier plane. $P(E_x)$ can be found using the WKB approximation [Bri70], giving an approximate solution of the stationary Schrödinger equation for a quasi-static potential and a barrier thickness d.

$$P(E_x) \propto \exp\left\{-\frac{2}{\hbar}\int_0^d \mathrm{d}x' \left[2m\left(\Phi(x',U)-E_x\right)\right]^{1/2}\right\} \tag{36}$$

Evaluating equation (35) assuming a mean potential barrier height $\bar{\Phi} = \bar{\Phi}(U)$, which is independent of x, gives an approximate equation for the tunnelling current I called the Simmons model [Sim63]

$$j_S(U) = j_0\left[\bar{\Phi}\exp\left\{-A\bar{\Phi}^{1/2}\right\} - \left(\bar{\Phi}+eU\right)\exp\left\{-A\left(\bar{\Phi}+eU\right)^{1/2}\right\}\right], \tag{37}$$

with $j = \frac{e}{2\pi h(\beta d)^2}$ and $A = \frac{4\pi\beta d}{h}(2m)^{1/2}$. d denotes the barrier thickness and β is a correction factor which can be set to unity assuming a homogeneous barrier. Since the barrier height $\bar{\Phi}$ is specified relative to the negatively biased electrode [Sim63+], only the regime where $U < 0$ in equation (37) is physically relevant.

A numerical approach modelling the conductance of aluminum tunnel barriers based on this model is given by Brinkman´s model [Bri70]. It states, that the current through a tunnel junction is in first order cubic in the applied voltage in the regime where $|U| \lesssim 0.2\,\mathrm{V}$. The voltage dependency of the conductivity $G(U)$ is consequently parabolic

$$\frac{G(U)}{G(0)} = 1 - \left(\frac{A_0 d}{16\bar{\Phi}^{3/2}}\right)eU + \left(\frac{9A_0^2}{128\bar{\Phi}}\right)(eU)^2, \tag{38}$$

with $A_0 = \frac{4d}{3\hbar}(2m)^{1/2}$ and $G(0) = 3.16\cdot 10^{10}\frac{\bar{\Phi}^{1/2}}{d}\exp\left\{-1.025\cdot d\bar{\Phi}^{1/2}\right\}$.

The deviation of the I-V characteristic from the ohmic branch arises when the voltage U across the Josephson junction approaches the mean potential barrier height $\bar{\Phi}$, and is also due to the increasing normal density of states $\rho(E)$ with energy

$$\rho(E) \propto E^{1/2}. \tag{39}$$

Qualitatively one could think that according to equation (39), more and more possible states for electrons to scatter in occur for an increasing voltage. This is schematically depicted in figure 4.

This effect allows to probe basic properties of a Josephson tunnel junction at room temperature such as the barrier uniformity or its sheet resistance R_n. Since $I_cR_n =$ const. and a function of Δ, as shown in section III.1.2, it is possible to directly infer the critical current I_c.

2 Basics of the transmon qubit

The state of a qubit as a quantum mechanical two-level system can be any superposition of the fundamental states $|0\rangle$ and $|1\rangle$, corresponding to the possible states

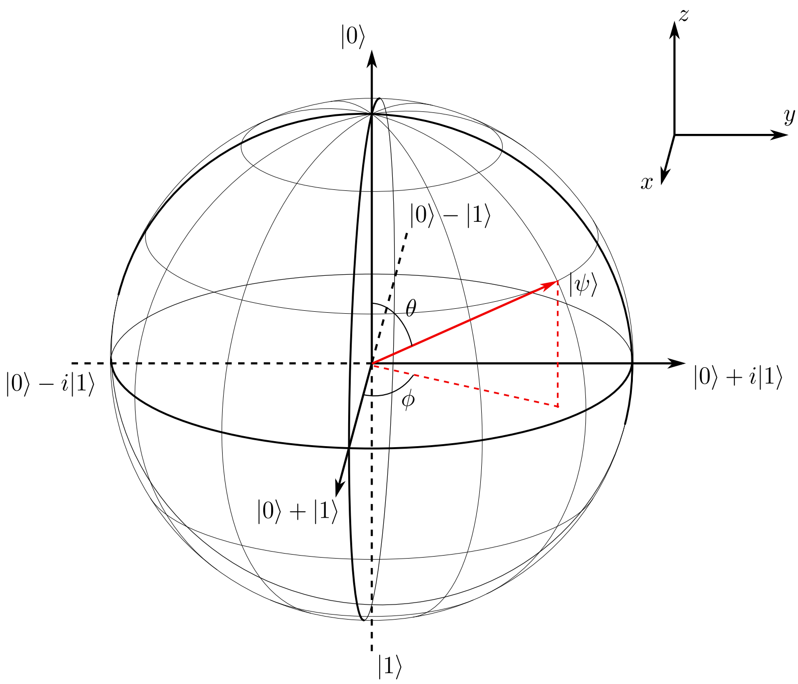

Figure 5: Schematic representation of the Bloch sphere. The fundamental qubit states $|0\rangle$, $|1\rangle$ correspond to the poles of the sphere. Any qubit state $|\psi\rangle$ can be represented in terms of the Euler angles θ, ϕ and is lying on the surface of the Bloch sphere.

of a classical bit. It is intuitive to represent the state $|\psi\rangle$ of a qubit as the position on the surface of the Bloch sphere as depicted in figure 5. The states along the axes x, y and z correspond to the eigenstates of the Pauli spin matrices $\hat{\sigma}_i$, respectively.

An arbitrary state $|\psi\rangle$ on the Bloch sphere can be written as

$$|\psi\rangle = \cos\frac{\theta}{2}|0\rangle + \sin\frac{\theta}{2}e^{i\phi}|1\rangle \tag{40}$$

employing the Euler angles ϕ and θ [Wen05, Sak68].

Expressing the fundamental states $|0\rangle$, $|1\rangle$ in terms of the eigenvectors of $\hat{\sigma}_z$,

$$|0\rangle = \begin{pmatrix} 1 \\ 0 \end{pmatrix}, \quad |1\rangle = \begin{pmatrix} 0 \\ 1 \end{pmatrix}, \tag{41}$$

equation (40) yields in vector notation

$$|\psi\rangle = \begin{pmatrix} \cos\frac{\theta}{2} \\ \sin\frac{\theta}{2}e^{i\phi} \end{pmatrix}. \tag{42}$$

This framework is used in the following sections to derive an elegant description of the transmon qubit and its interaction with its environment.

The key element to realize a qubit based on superconducting devices is the Josephson junction introduced in section 1. Within the RCSJ model, it can be considered as a small capacitor being connected in parallel with an inductor. The crucial point is the non-linearity of the inductance L, which can be manipulated externally. From an architectural point of view, the Josephson junction can be compared to a harmonic LC-resonator. However, while a quantum mechanical harmonic oscillator has energy levels of equal spacing, the energy levels of a Josephson junction are non-equidistant. It is this anharmonicity that allows the Josephson junction to work as a qubit since one can clearly identify the two lowest energy levels to correspond to the fundamental qubit states $|0\rangle$ and $|1\rangle$. This distinction would be impossible for a usual resonator of equidistant level spacing since all transitions between neighbouring states are degenerate.

A brief overview of the dynamical behaviour of a qubit is given in section 2.1. Section 2.2 concentrates on the Cooper pair box and gives a mathematical formulation to describe the important mechanisms. Since the transmon design is derived from that of the Cooper pair box, it is possible to treat the transmon on the same mathematical footing while considering another limiting case of the characteristic parameters. This is presented in section 2.3.

2.1 Dynamical behaviour of a qubit

By performing spectroscopy measurements, a qubit can be identified as a functioning device and a rough estimate concerning its coherence behaviour is possible. Relevant parameters of the qubit such as its resonance frequency or the excitation frequency are swept and the response on a readout device is registered.

Measurements in the time domain exactly determine the dynamical behaviour of the qubit, which is mainly characterized by two times T_1, T_2 [Cla08], in analogy to the definition in nuclear magnetic resonance (NMR) spectroscopy [Sli90]. Decoherence occurs due to the weak coupling of the qubit to its environment.

The relaxation time T_1 is the time in which the qubit relaxes from its excited state $|1\rangle$ to its ground state $|0\rangle$, corresponding to the Bloch vector going from the south to the north pole of the Bloch sphere, see figure 5. Spontaneous qubit transitions under photon emission or absorption constitute the major relaxation mechanism. T_1 is typically measured by exciting the qubit with a π-pulse and measuring its state after variable times.

The dephasing time T_2 is the time after which all information about the phase between qubit eigenstates of a certain qubit state is destroyed. It arises from fluctuations in the energy level splitting E_{01} between the two fundamental qubit states. Dephasing corresponds to a movement of the Bloch vector in the $x - y$ plane, relative to its rotation with the Larmor precession frequency. Since all phase information is lost at the poles of the Bloch sphere, the dephasing time T_2 is limited by the relaxation time T_1 according to equation (43).

$$\frac{1}{T_2} = \frac{1}{2T_1} + \frac{1}{\tau} \tag{43}$$

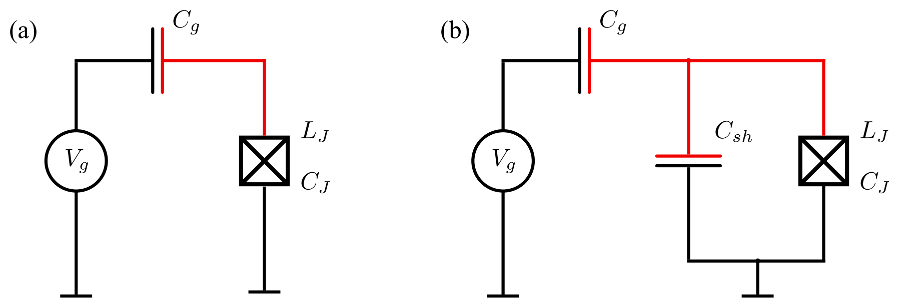

Figure 6: (a) Circuit diagram of a single Cooper pair box. The gate capacitance C_g couples the Josephson junction with intrinsic capacitance C_J and kinetic inductance L_J to the gate electrode of voltage V_g. The superconducting island is coloured in red. (b) Circuit diagram of a transmon. The additional shunt capacitance C_{sh} strongly increases the ratio E_J/E_C.

τ corresponds to pure dephasing [Cla08]. The dephasing time T_2 can be obtained in a Ramsey experiment [Ram49] or directly from the transition peak broadening in spectroscopy.

In a so called Rabi experiment [Rab38], decoherence induced by energy relaxation as well as dephasing is observed.

2.2 The single Cooper pair box

One very interesting type of qubit based on a Josephson junction circuit is the single Cooper pair box, depicted in figure 6(a). It consists of a small superconducting island (red) which is connected via a Josephson junction to a large superconducting reservoir [Nak99, Wen05]. In addition, the island is capacitively coupled via C_g to a massive gate electrode. A voltage source V_g controls the gate potential and therefore the offset charge n_g on the island.

The energy that is required to place a single charge e on the island at zero voltage is the charging energy [Cla08]

$$E_C = \frac{e^2}{2C_\Sigma}. \tag{44}$$

C_Σ is the total capacitance of the Cooper pair box

$$C_\Sigma = C_g + C_J \tag{45}$$

which is evident considering the equivalent circuit of figure 6(a). For E_C large compared to the Josephson energy E_J and the thermal energy k_BT, respectively, fluctuations of the charge on the island are suppressed [Nak99]. In the normal state, this corresponds to the Coulomb blockade regime [Gra91, Wen05], where electrons can only be transferred to the island one by one. k_B here denotes Boltzmann´s constant.

Charging steps on a superconducting island in units of $2e$ were experimentally first observed by P. Lafarge *et al.* [Laf93], operating the Cooper pair box with a charging energy E_C below the superconducting gap Δ.

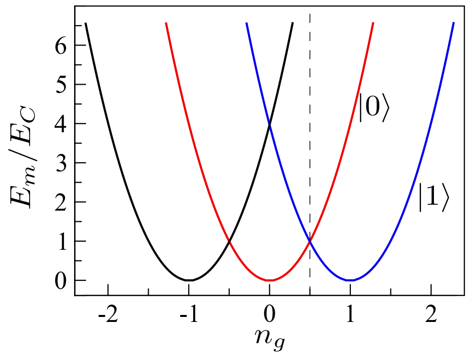

Figure 7: Eigenenergies E_m with respect to the offset charge n_g for different values of the Cooper pair number n. The first two charge states $|0\rangle$ and $|1\rangle$, which are the relevant states for a qubit, are shown in red and blue, respectively.

Due to the weak coupling to its environment, the state of the island can be described by the macroscopic state $|n\rangle$, using the number operator $\hat{n}$ which counts the number of additional Cooper pairs on the island with respect to the offset charge n_g in units of Cooper pairs. The two qubit states can then be associated with two adjacent Cooper pair number states $|n\rangle$ and $|n+1\rangle$ [Cla08, Nak99]. This is why the Cooper pair box is referred to as a charge qubit.

From figure 6(a), it is straightforward to write down the total energy H of the system comprising the electrostatic energy stored by the total capacitance C_Σ and the magnetic energy stored in the non-linear inductor formed by the Josephson junction. Using operators for the Cooper pair number $\hat{n}$ and the phase difference $\hat{\delta}$, employing the Josephson potential U_J from equation (28) at zero current γ and the definition of E_C from equation (44) yields

$$\begin{aligned}\hat{H} &= \frac{1}{2C_\Sigma}\left[2e(\hat{n}-n_g)\right]^2 + U_J\,|_{\gamma=0} = \frac{1}{2C_\Sigma}\left[2e(\hat{n}-n_g)\right]^2 - E_J\cos\hat{\delta} \\ &= 4E_C\,(\hat{n}-n_g)^2 - E_J\cos\hat{\delta}. \end{aligned} \tag{46}$$

For a Cooper pair box operating in the charge regime where $E_J \ll E_C$, the Josephson term can be neglected and the eigenenergies of the Hamiltonian (46) are parabolas when plotted against the offset charge n_g, see figure 7. At certain values of the offset charge, neighbouring parabolas intersect and therefore the corresponding charge eigenstates are degenerate. Switching on a small Josephson coupling as a perturbation lifts the degeneracy and distinct energy bands form [Wen05], shown in figure 8(a).

The qubit Hamiltonian in matrix representation is obtained by projecting the Hamiltonian (46) on the qubit charge states $|0\rangle$, $|1\rangle$ and using the representation (41) as well as the definition (17).

$$\hat{H} = \begin{pmatrix} 0 & -\frac{E_J}{2} \\ -\frac{E_J}{2} & 4E_C\,(1-2n_g) \end{pmatrix} \tag{47}$$

Note that $\left(\hat{n}^2 - 2\hat{n}n_g + n_g^2\right)|n\rangle = n\,(1-2n_g)\,|n\rangle$ omitting a constant. Diagonalization of (47) gives the qubit eigenenergies (48) valid close to the degeneracy point

$n_g = \frac{1}{2}$.

$$E_{0/1} = \pm\frac{1}{2}\sqrt{\left(4E_C\left(1-2n_g\right)\right)^2 + E_J^2} \tag{48}$$

The level separation at the degeneracy point equals the Josephson energy E_J and the qubit eigenstates are cat states $|0\rangle \pm |1\rangle$.

2.3 Properties of the transmon qubit

The Cooper pair box presented in the previous section has had its main significance in demonstrating the isolation of single charges [Dev92] before it was considered as a charge qubit [Nak99]. Like the other fundamental types of superconducting qubits, the phase qubit and the flux qubit, it has major drawbacks when it comes to coherence time, which is the crucial property of a qubit.

A new approach in qubit design is the transmission line shunted plasma oscillation qubit, called *transmon* [Koc07]. Its architecture is strongly based on the Cooper pair box, see figure 6. Adding a large shunt capacitance C_{sh} in parallel to the Josephson junction significantly increases the ratio of Josephson energy E_J to charging energy E_C. Therefore the transmon is operated in the phase regime, where the phase difference δ across the Josephson junction is the relevant degree of freedom and consequently the good quantum number to describe the system.

The aim of the transmon design is to maintain the insensitivity of the Cooper pair box to critical current and flux noise [Koc07] but at the same time also highly reduce its sensitivity to charge noise, which is the main weakness of the conventional charge qubit. While strongly increasing the ratio E_J/E_C leads to a levelling of the qubit energy splittings, a sufficiently large anharmonicity of the transmon is to be preserved.

Due to the lack of qualitative changes in the architecture, the effective Hamiltonian of the transmon takes the exact form of the Cooper pair box system, see equation (46)

$$\hat{H} = 4E_C\left(\hat{n} - n_g\right)^2 - E_J\cos\hat{\delta}. \tag{49}$$

According to figure 6(b), the total capacitance C_Σ for calculating the charging energy $E_C = \frac{e^2}{2C_\Sigma}$ is given by

$$C_\Sigma = C_g + C_J + C_{sh}, \tag{50}$$

including the shunt capacitance C_{sh}. For large C_{sh}, the charging energy is reduced and the ratio E_J/E_C is increased.

The characteristic properties of the transmon system can be extracted from an exact solution of the Hamiltonian (49). Following the approach of [Koc07], one can write the corresponding Schrödinger equation in the phase basis using the operator equivalence $\hat{n} = -i\frac{\mathrm{d}}{\mathrm{d}\delta}$,

$$\left[4E_C\left(-i\frac{\mathrm{d}}{\mathrm{d}\delta} - n_g\right)^2 - E_J\cos\delta\right]\psi(\delta) = E\psi(\delta). \tag{51}$$

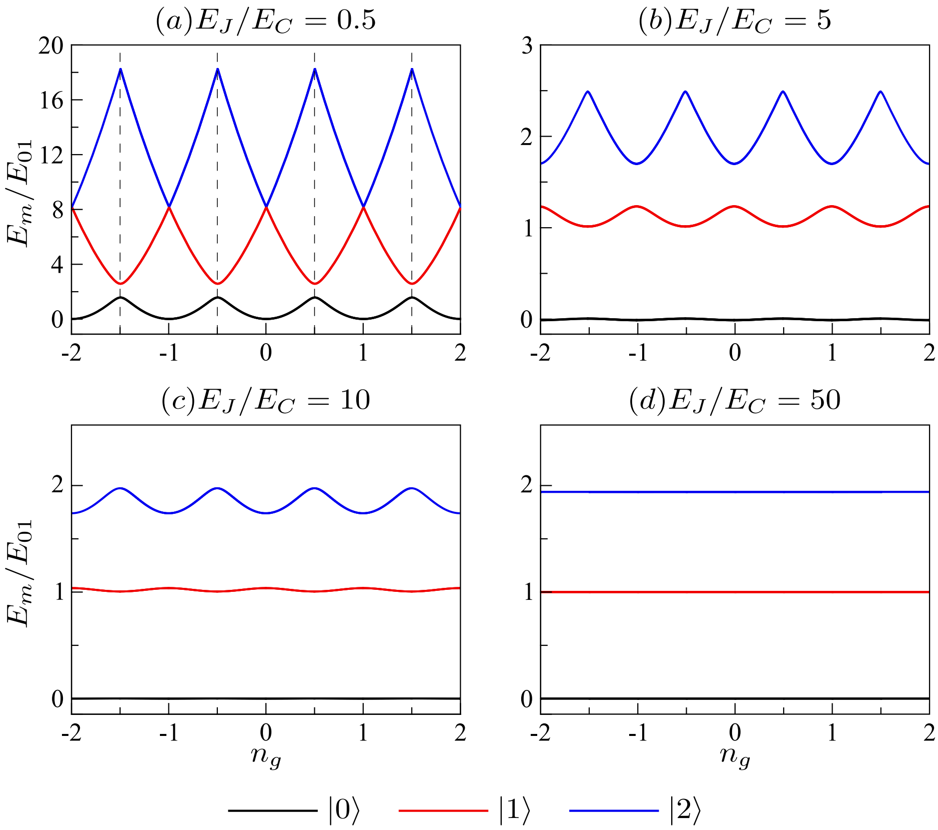

Figure 8: Eigenenergies E_m of the transmon Hamiltonian (49) with respect to the offset charge n_g for the lowest three levels $m = 0, 1, 2$ and for different ratios E_J/E_C. The eigenenergies are normalized to the transition energy $E_{01} = \sqrt{8E_JE_C}$ between the ground state and the first excited state and an offset is subtracted so that $E_0(0) = 0$. (a) Typical E_J/E_C ratio for a conventional charge qubit. Dashed lines mark the sweet spots at half-integer n_g. (d) Typical energy dispersion in the transmon regime. Plots are inspired by [Koc07].

Identifying $\delta \to 2x$ and introducing $g(x) = e^{-2in_g x}\psi(2x)$, equation (51) can be rewritten as

$$g''(x) + \left(\frac{E}{E_C} + \frac{E_J}{E_C}\cos(2x)\right) g(x) = 0 \tag{52}$$

and takes the typical form of Mathieu´s differential equation [Ast64]

$$y''(x) + [a - 2q\cos(2x)]\, y = 0. \tag{53}$$

Due to the periodicity of the wave function $\psi(\delta + 2\pi) = \psi(\delta)$, the solution of equation (52) can be expressed in the Floquet form [Ast64]

$$g(x) = e^{i\nu x} P(x) \tag{54}$$

with $P(x)$ π-periodic in x. Consequently, one can write the first part in brackets of equation (52), $\frac{E}{E_C}$, in terms of Mathieu´s characteristic value $a_\nu(q)$ with characteristic exponent $\nu = -2n_g$ and $q = -\frac{E_J}{2E_C}$ [Wol13], comparing equations (52), (53). The eigenenergies of the Hamiltonian (49) are therefore given by

$$E_m(n_g) = E_C a_{-2n_g + k_m}\left(-\frac{E_J}{2E_C}\right). \tag{55}$$

The integer number k_m appropriately sorts the eigenvalues [Koc07] to cover a certain range of n_g. Figure 8 shows the eigenenergies $E_m(n_g)$ of the Hamiltonian (55) with respect to the offset charge n_g and Josephson energy to charging energy ratio E_J/E_C.

The total charge dispersion corresponding to the width of the energy bands and being a direct measure of the qubit´s charge noise sensitivity, decreases with increasing ratio E_J/E_C. In fact, according to [Koc07], the charge dispersion decreases exponentially with $\sqrt{E_J/E_C}$. Therefore, operating the qubit in the phase regime, where $E_J/E_C \gtrsim 50$, the qubit is extremely stable with respect to charge noise.

Figure 8(a) shows the typical charge dispersion of a conventional charge qubit. To avoid the qubit to be strongly sensitive to charge noise, it is biased to one of the so called “sweet spots” which are the degeneracy points at half-integer n_g. Since the slope of E_m vanishes at these sweet spots, linear noise contributions do not lead to dephasing of the qubit. However it is experimentally very challenging and sometimes impossible to keep the system exactly at one of these sweet spots.

According to figure 8, when $E_J \gg E_C$, the charge dispersion flattens out, which leads to a suppression of charge noise even in higher order. It is not necessary to bias the system by a gate voltage to a certain point since basically there is a charge sweet spot everywhere. In addition, the application of an external flux bias is not necessary. This is the reason why the transmon is called self-biased.

A comparison of the charge noise sensitivity of the transmon being operated at $E_J/E_C = 100$, with second order charge noise sensitivity $\frac{\partial^2 E_{01}}{\partial n_g^2}$ using the eigenenergies (48) for the charge qubit at $E_J/E_C = 0.1$ yields a relative factor of up to 10^{10}.

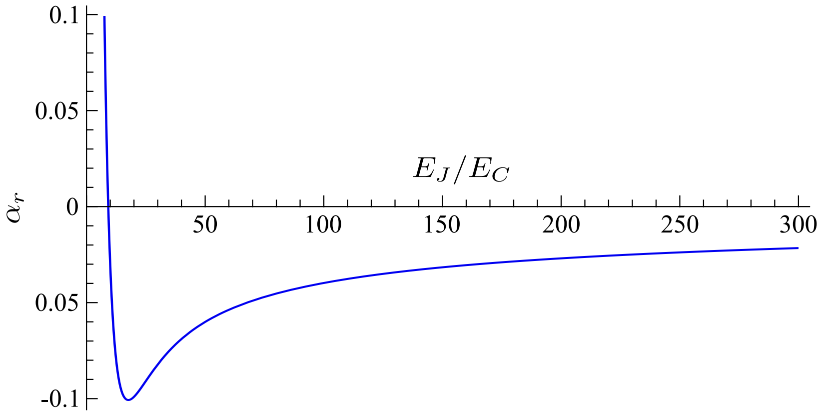

Figure 9: Relative anharmonicity α_r with respect to the ratio E_J/E_C. After passing a local extremum at $E_J/E_C \approx 20$, it approaches zero asymptotically for $E_J/E_C \to \infty$. For $E_J/E_C \approx 300$, the relative anharmonicity is reduced to approximately 2.5%.

In addition, it can be observed, that the level anharmonicity at the degeneracy points is decreasing with increasing ratio E_J/E_C. The absolute anharmonicity α can be defined as

$$\alpha = E_{12} - E_{01}, \tag{56}$$

where $E_{ij} = E_j - E_i$. Normalized to the level spacing E_{01} of the relevant levels corresponding to qubit eigenstates $|0\rangle$, $|1\rangle$, the relative anharmonicity α_r is defined as

$$\alpha_r = \frac{\alpha}{E_{01}}. \tag{57}$$

Figure 9 shows the relative anharmonicity α_r with respect to the ratio E_J/E_C. Beyond the minimum it obeys a weak power law, asymptotically approaching zero for $E_J/E_C \to \infty$.

Finding the charge dispersion to decrease exponentially and the level anharmonicity to increase only algebraically with increasing ratio E_J/E_C is very convenient. It allows to design the transmon to be highly insensitive to charge noise while preserving a large enough anharmonicity to operate it as a qubit at the same time. Typical values for the ratio of Josephson energy to charging energy are in the range 50..400.

In the limit $E_J \gg E_C$, the eigenenergies of the transmon Hamiltonian can be approximated using perturbation theory in E_C/E_J [Koc07]. Neglecting the charging energy term in the Hamiltonian (49) and expanding the cosine around zero up to fourth order in the phase difference δ yields

$$\hat{H} \approx -E_J + E_J \frac{\hat{\delta}^2}{2} - E_J \frac{\hat{\delta}^4}{24}. \tag{58}$$

Using the representation of the phase difference $\hat{\delta}$ in terms of bosonic creation and annihilation operators $\hat{b}$, $\hat{b}^\dagger$ [Koc07] of the transmon system

$$\hat{\delta} = \frac{1}{\sqrt{2}} \left(\frac{8E_C}{E_J} \right)^{1/4} \left(\hat{b} + \hat{b}^\dagger \right) \tag{59}$$

and inserting into equation (58) gives

$$\hat{H} \approx -E_J + \sqrt{8E_C E_J}\left(\hat{b}^\dagger \hat{b} + \frac{1}{2}\right) - \frac{E_C}{12}(\hat{b} + \hat{b}^\dagger)^4. \tag{60}$$

Projecting the Hamiltonian (60) on arbitrary qubit states and keeping only terms that are conserving particle number yields the approximate eigenenergies

$$E_m \approx -E_J + \sqrt{8E_C E_J}\left(m + \frac{1}{2}\right) - \frac{E_C}{4}(2m^2 + 2m + 1). \tag{61}$$

Here, the qubit´s resonance frequency $\omega_R = \frac{1}{\hbar}\sqrt{8E_C E_J}$ appears and equals the Josephson plasma frequency ω_P defined in equation (31).

From equation (59), it is clear that $\Delta\delta$ is small in the limit $E_J \gg E_C$, confirming its good nature as a quantum number in the present regime.

With the eigenenergies from equation (61), the absolute and relative anharmonicity of the transmon take the approximate form

$$\alpha \approx -E_C, \quad \alpha_r = -\sqrt{\frac{E_C}{8E_J}}. \tag{62}$$

3 Circuit QED for the transmon qubit

One of the fundamental processes in nature is the interaction of matter and light [Wal04]. Thus, for several decades it was the aim of atomic physics and quantum optics to study the interaction of a single atom with discrete photon modes. This established the branch of cavity quantum electrodynamics (CQED) [Har06].

With the invention of the first qubits based on superconducting circuits, the relevance of CQED for quantum information processing has been discovered. The concept of on-chip implementation of a CQED system consisting of a transmission line resonator and a qubit serving as an artificial atom is also termed circuit quantum electrodynamics [Wal04, Bla04].

An ideal candidate for performing CQED is the Cooper pair box due to its large dipole moment $\vec{d}$ [Wal04]. Playing the role of an artificial atom, the Cooper pair box is coupled to a transmission line resonator. The number of photons being carried by the resonator corresponds to its discrete energy level. Since the effective mode volume of the resonator is very small, the electric field $\vec{E}$ is large, and the strong coupling limit [Bla04], where

$$\hbar g \propto \vec{d} \cdot \vec{E} \gg \left[\frac{h}{T_1}, \hbar\kappa\right] \tag{63}$$

can be reached. g is the coupling constant between resonator and qubit, T_1 the qubit relaxation time and κ the photon loss rate of the resonator.

The reason why CQED plays such an important role in quantum information processing is the possibility of controlling the qubit without substantially decreasing the qubit´s lifetime. Under certain conditions, even a quantum non-demolition measurement of the qubit state is possible. While it is an intrinsic property of a quantum measurement that the measured quantum state collapses into one of its eigenstates, a quantum non-demolition measurement means a projection measurement of the qubit state, where the qubit state after the measurement equals the measurement outcome.

Of course the above considerations hold when the Cooper pair box is operated in the transmon regime.

In the following, the Jaynes-Cummings Hamiltonian is derived and the relevant control and readout mechanisms for the qubit on resonance with its readout resonator and in the dispersive regime are given. In the end of the section, the transmon´s coherence times are estimated, regarding the implementation of the qubit in CQED.

3.1 Jaynes-Cummings model

The Hamiltonian describing the full CQED system is

$$\hat{H} = \hat{H}_{res} + \hat{H}_q + \hat{H}_{int}. \tag{64}$$

$\hat{H}_{res}$ describes the energy of the transmission line resonator and takes the familiar form of a harmonic oscillator

$$\hat{H}_{res} = \hbar\omega_r \left(\hat{a}^\dagger \hat{a} + \frac{1}{2}\right), \tag{65}$$

with resonance frequency ω_r and bosonic creation and annihilation operators $\hat{a}^\dagger$, $\hat{a}$.

In analogy to other two-level systems such as a spin 1/2, the qubit Hamiltonian can be written in terms of the Pauli spin matrix $\hat{\sigma}_z$ and the transition frequency ω_q:

$$\hat{H}_q = \frac{\hbar}{2}\omega_q \hat{\sigma}_z \tag{66}$$

The point of zero energy is set in the middle of the two levels described by the Hamiltonian (66).

According to [Har06], the interaction Hamiltonian $\hat{H}_{int}$ is given by

$$\hat{H}_{int} = -\hat{\vec{d}} \cdot \hat{\vec{E}}, \tag{67}$$

with dipole operator $\hat{d} \propto \left(\hat{\sigma}^+ + \hat{\sigma}^-\right)$ of the qubit and electric field $\hat{E} \propto \left(\hat{a}^\dagger + \hat{a}\right)$ of the resonator. $\hat{\sigma}^\pm$ are the atomic ladder operators, bringing the qubit from the ground state into the excited state or vice versa. Therefore the interaction Hamiltonian can be written as

$$\hat{H}_{int} = \hbar g \left(\hat{\sigma}^+ + \hat{\sigma}^-\right)\left(\hat{a}^\dagger + \hat{a}\right), \tag{68}$$

with g being again the coupling constant. Terms corresponding to the excitation of the qubit and simultaneous creation of a photon $\hat{\sigma}^+\hat{a}^\dagger$, and the inverse process $\hat{\sigma}\hat{a}$,

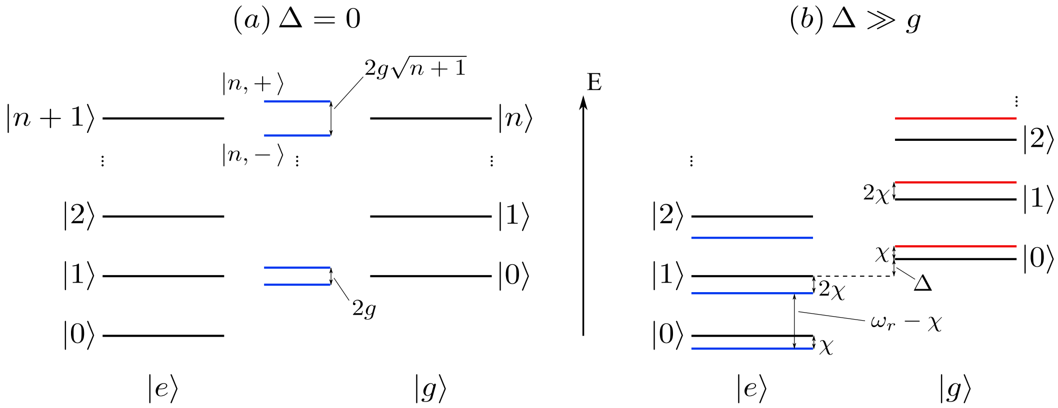

Figure 10: (a) Energy spectrum of the qubit-resonator system. The resonator Fock state is denoted by $|n\rangle$, while the qubit state is either $|g\rangle$ or $|e\rangle$, meaning ground and excited state, respectively. The degeneracy of the states of equation (71) is indicated. Dressed qubit-resonator states are depicted in blue. (b) Energy spectrum in the dispersive regime. The degeneracy is lifted by the detuning Δ and one can see the detuning of the resonator´s energy levels dependent of the qubit state (blue and red).

can be neglected, as they violate energy conservation [Cri91] and are highly non-resonant [Har06]. In analogy to a spin 1/2 being subject to an oscillating magnetic field, the Bloch vector precesses around the z-axis due to the time evolution of the qubit state $|\psi\rangle$, given in equation (40). The Bloch sphere is conveniently considered in this rotating frame, rotating with the qubit´s Larmor frequency with respect to the rest system. This is called the rotating wave approximation, valid in case of the resonator frequency ω_r being close to the qubit transition frequency ω_q. As will become clear in section 1, this is indeed the case for the system considered in this work.

As a result, one can write down the Jaynes-Cummings Hamiltonian

$$\hat{H} = \hbar\omega_r \left(\hat{a}^\dagger \hat{a} + \frac{1}{2}\right) + \frac{\hbar}{2}\omega_q \hat{\sigma}_z + \hbar g \left(\hat{\sigma}^+ \hat{a} + \hat{\sigma}^- \hat{a}^\dagger\right). \tag{69}$$

It is named after E. Jaynes and F. Cummings, who formulated it in a similar form to apply it to their beam maser [Jay63].

Calculating the energy spectrum of the Hamiltonian (69) gives an understanding of the remarkable benefits of this qubit-resonator system.

One has to distinguish two different regimes. The crucial parameter is the qubit-resonator detuning Δ, which is defined as

$$\Delta = \omega_q - \omega_r. \tag{70}$$

3.1.1 Zero detuning

In case of zero detuning $\Delta = 0$, it is $\omega_q = \omega_r$. The interaction part $\hat{H}_{int}$ in the Jaynes-Cummings Hamiltonian (69) can be regarded as a perturbation, since $g \ll$

ω_q, ω_r. One can easily verify, that there exist degenerate states of the unperturbed Hamiltonian, namely

$$\begin{aligned} |\psi_{n,g}\rangle &= |n\rangle \otimes |g\rangle = |n, g\rangle \\ |\psi_{n+1,e}\rangle &= |n+1\rangle \otimes |e\rangle = |n+1, e\rangle. \end{aligned} \tag{71}$$

Here, n denotes the Fock state of the resonator and $|g\rangle$, $|e\rangle$ correspond to the qubit eigenstates $|0\rangle$, $|1\rangle$, respectively. This notation is chosen to avoid confusion of states in the two spaces.

In terms of degenerate perturbation theory [Sak68], one has to diagonalize the full Hamiltonian (69) in the subspace spanned by the degenerate eigenstates (71). Calculating the matrix elements yields

$$\hat{H} = \begin{pmatrix} \omega_r\left(n+\frac{1}{2}\right)+\frac{\omega_q}{2} & g\hat{a} \\ g\hat{a}^{\dagger} & \omega_r\left(n+\frac{3}{2}\right)-\frac{\omega_q}{2} \end{pmatrix} \tag{72}$$

and diagonalization gives the general expression

$$E_n^{\pm} = \hbar\omega_r(n+1) \pm \frac{\hbar}{2}\sqrt{\Delta^2 + 4g^2(n+1)}. \tag{73}$$

Under the assumption $\Delta = 0$, equation (73) reduces to

$$E_n^{\pm} = \hbar\omega_r(n+1) \pm \hbar g\sqrt{n+1}. \tag{74}$$

The corresponding dressed eigenstates [Bla04] describing the whole CQED system are

$$\begin{aligned} |n,+\rangle &= \frac{1}{\sqrt{2}}\left(|n+1,e\rangle + |n,g\rangle\right) \\ |n,-\rangle &= \frac{1}{\sqrt{2}}\left(|n+1,e\rangle - |n,g\rangle\right). \end{aligned} \tag{75}$$

Therefore the degeneracy of the unperturbed Hamiltonian is lifted by switching on the qubit-resonator interaction. The energy spectrum of the uncoupled resonator-qubit states and corresponding dressed states are shown in figure 10(a).

3.1.2 Large detuning: The dispersive limit

The aim of CQED applied in quantum computation is coherent control and readout of the qubit. It has been demonstrated, that this is especially possible when operating a Cooper pair box system in the dispersive limit [Bla04]. In this case, the qubit-resonator detuning Δ is large, in particular

$$\frac{g}{\Delta} \ll 1. \tag{76}$$

Making a canonical transformation with the transformation matrix [Bla04]

$$\hat{U} = \exp\left\{\frac{g}{\Delta}\left(\hat{a}\hat{\sigma}^{+} - \hat{a}^{\dagger}\hat{\sigma}^{-}\right)\right\}, \tag{77}$$

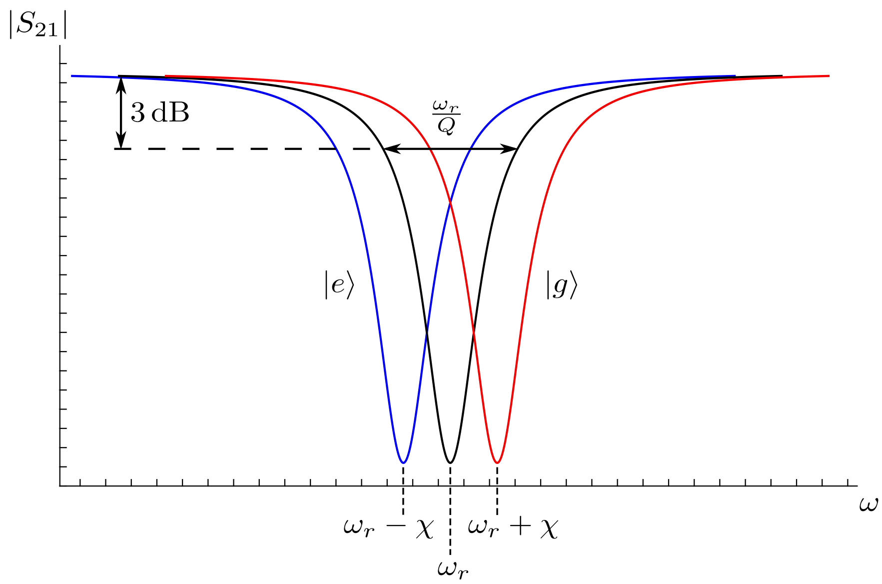

Figure 11: Transmission amplitude spectrum of the resonator for large detuning. Dependent on the qubit´s state and the sign of Δ, the resonator´s resonance frequency is increased or decreased by the dispersive shift χ.

one can eliminate the qubit-resonator coupling g in first order and write down an effective Hamiltonian $\hat{H}_{eff}$ for the whole system:

$$\begin{aligned} \hat{H}_{eff} &= \hat{U}\hat{H}\hat{U}^{\dagger} \\ &= \hbar\left[\omega_r + \frac{g^2}{\Delta}\hat{\sigma}_z\right]\hat{a}^{\dagger}\hat{a} + \frac{\hbar}{2}\left[\omega_q + \frac{g^2}{\Delta}\right]\hat{\sigma}_z \\ &= \hbar\left[\omega_r + \chi\hat{\sigma}_z\right]\hat{a}^{\dagger}\hat{a} + \frac{\hbar}{2}\left[\omega_q + \chi\right]\hat{\sigma}_z \end{aligned} \tag{78}$$

To obtain equation (78), terms of the order $O\left(\left(\frac{g}{\Delta}\right)^2\right)$ occurring in the expansions of the exponential functions are neglected, according to the condition in equation (76), and constant terms are omitted. In the last step, the dispersive shift χ is introduced, defined as

$$\chi = \frac{g^2}{\Delta}. \tag{79}$$

Hence, when the qubit-resonator system is operated in the dispersive regime, the effective resonance frequencies of both the qubit and the resonator are shifted by χ, according to the Hamiltonian (78). Particularly, the resonance frequency of the resonator depends on the state of the qubit due to the $\hat{\sigma}_z$ operator in equation (78). Performing a measurement by exciting the resonator with photons induces a collapse of the qubit superposition state into one of its eigenstates $|0\rangle$, $|1\rangle$. The state of the qubit after this measurement equals the measured state with a fidelity of almost one. This constitutes indeed a quantum non-demolition measurement, which is crucial to implement fast qubit gate operations.

A typical transmission amplitude spectrum of a resonator dispersively coupled to a qubit is shown in figure 11.

It is important to note, that it is possible to infer the superposition state of the qubit by applying statistics. Preparing the qubit in the same superposition state and measuring it several times leads to a probability distribution of the qubit eigenstates. Applying suitable gates before measuring the qubit such as a rotation moreover allows to restore the phase information of the initial superposition state.

The effective Hamiltonian in equation (78) can be rewritten to highlight the effect of the resonator on the qubit [Sch07] as

$$\hat{H}_{eff} = \hbar\omega_r \hat{a}^\dagger \hat{a} + \frac{\hbar}{2}\left[\omega_q + 2\chi\hat{a}^\dagger\hat{a} + \chi\right]\hat{\sigma}_z. \tag{80}$$

In this ordering, the resonance frequency ω_r of the resonator seems to be not altered, while the qubit frequency is additionally shifted by 2χ per photon in the readout resonator. Since this contribution is dependent on the electric field of the resonator seen by the qubit, it is called ac-Stark shift, in analogy to atomic physics. In that framework, the constant dispersive contribution χ can be regarded as vacuum noise [Sch07] and is therefore called Lamb shift.

The fact that both perspectives coexist and the mutual back-action of the qubit-resonator system is required, reflects the ultimate principle of a quantum measurement, imposed by Heisenberg´s uncertainty.

It was shown by [Koc07], that these concepts are valid in the transmon regime. Because of the reduced anharmonicity of the transmon, higher excitations are to be taken into account. This leads to a slightly modified effective dispersive shift χ_{eff}. χ_{eff} reduces to the dispersive shift given in equation (79) for $\Delta \ll E_C$.

In the limit of vanishing anharmonicity, the dispersive shift χ also approaches zero. However, this effect is compensated for the transmon system by an increased coupling strength g, which is seen from the definition (79) of χ. The increase in g originates from the relation [Koc07]

$$g \propto \left(\frac{E_J}{E_C}\right)^{1/4}. \tag{81}$$

In conclusion, the dispersive shift of the transmon is comparable to that of a conventional Cooper pair box. Therefore, there is no contradiction between strong coupling and vanishing charge noise sensitivity for the transmon system.

An energy spectrum of the CQED system in the dispersive regime is shown in figure 10(b).

3.2 The Purcell effect

Among various potential noise channels leading to relaxation of the transmon such as dielectric losses at surface oxides or quasi-particle tunnelling, the so called Purcell effect [Pur46] has to be taken into account when designing a CQED circuit.

The Purcell effect describes a modification of the spontaneous emission rate of a two-level system such as a qubit, when coupled to a resonator or cavity. For the transmon, operated in the dispersive limit, a Purcell-induced relaxation rate γ_P occurs which is given [Koc07] by

$$\gamma_P = \kappa \frac{g^2}{\Delta^2}. \tag{82}$$

κ is the average photon loss rate of the resonator and g, Δ the coupling constant and the detuning of transmon and resonator, respectively. The Purcell relaxation rate in equation (82) leads to an upper bound of the transmon´s relaxation time T_1, given by

$$T_P = \frac{2\pi}{\gamma_P}. \tag{83}$$

4 Resonator theory applied to microstrip geometry

The relevant frequencies for quantum information processing using superconducting devices are lying in the region of several GHz, corresponding to microwaves. Typical devices to transmit high-power microwaves with a very high bandwidth and low loss are coaxial cables [Poz98]. However, when it comes to the implementation of complex microwave circuits, coaxial cables are too bulky and a planar structure allowing microwaves to propagate is required [Gup96].

Among more complex geometries, the coplanar waveguide and the microstrip structure are favoured. In case of the coplanar waveguide, a center strip is surrounded by a ground plane, leaving a small gap in between. This two-dimensional geometry is structured on a substrate with an optional ground plane added below the substrate. The electric field lines will partly be in the substrate and above the structured layer, but mostly focussed in between the center strip and the enclosing ground plane.

In this work, the qubit system is implemented in microstrip geometry. A detached strip is structured on top of a substrate with a single ground plane below the substrate, see figure 12(a) or 15(b). In this case, the electric field lines are located partly above the substrate in the vacuum region but mostly in the substrate. The ground plane literally “pulls” the field lines into the substrate. Since the loss tangent δ in a typical substrate material such as silicon is below 10^{-6} [Vis10], this microstrip geometry promises high quality factors and good coherence times for the qubit. As the distance between center strip and ground plane is large compared to a coplanar geometry, the electric fields are much smaller. This leads to a reduction of losses caused by surface or interface defect states.

In the following sections, relevant parameters for a microstrip transmission line are given and the necessary theory for resonator characterization is presented.

4.1 Relevant parameters for a microstrip transmission line

Figure 12(a) shows a schematic of a microstrip line of width W and substrate thickness d. The dielectric constant of the substrate is ϵ_r, the region above the substrate

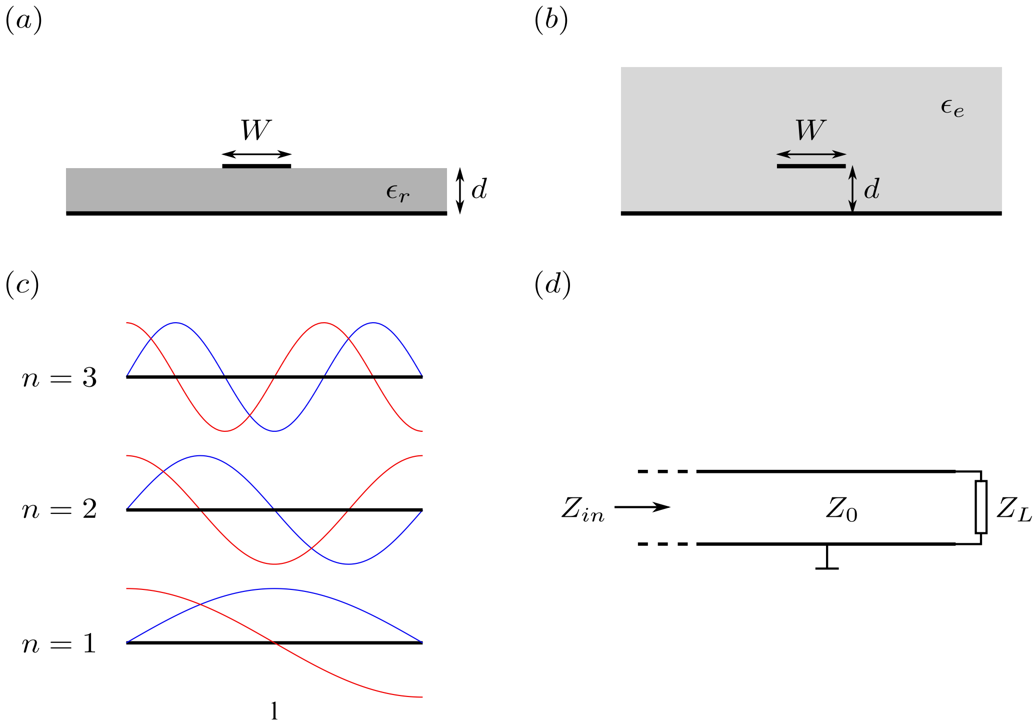

Figure 12: (a) Schematic depiction of a microstrip transmission line of width W. The substrate thickness is d and its dielectric constant ϵ_r. The region above is vacuum. (b) Equivalent geometry of the microstrip line. All space is homogeneously filled with a material of dielectric constant ϵ_e. (c) $\frac{\lambda}{2}$-resonator with voltage (red) and current distribution (blue). There are voltage antinodes and current nodes at the ends of the resonator. $n = 1$ for the fundamental mode. (d) Schematic representation of a transmission line with characteristic impedance Z_0, load impedance Z_L and input impedance Z_{in}.

is considered as vacuum. To calculate characteristic parameters of the microstrip line, it is convenient to specify an effective dielectric constant ϵ_e. It can be interpreted as the dielectric constant of a homogeneous material fully surrounding the strip as shown in figure 12(b). According to [Poz98], it is

$$\epsilon_e = \frac{\epsilon_r + 1}{2} + \frac{\epsilon_r - 1}{2} \frac{1}{\sqrt{1 + 12d/W}}. \tag{84}$$

Using equation (84), the phase velocity v_P in the medium becomes

$$v_P = \frac{c}{\sqrt{\epsilon_e}} \tag{85}$$

and the modified propagation constant β becomes

$$\beta = k\sqrt{\epsilon_e}. \tag{86}$$

c is the speed of light and k the propagation constant in vacuum, respectively.

4.2 Resonator theory

The resonator employed in this work for the CQED transmon system is a half-wavelength resonator, or in short notation a $\frac{\lambda}{2}$-resonator. This means, that both ends of the resonator strip are floating, thus there is no short to ground. Accordingly, there are always voltage anti-nodes at the ends of the resonator, which allows a capacitive coupling to nearby conductors. For the fundamental mode, the voltage vanishes in the middle of the $\frac{\lambda}{2}$-resonator. Since the current of the transmission line is shifted relative to the voltage by $\frac{\pi}{2}$ in phase, current nodes appear at the resonator´s ends, where inductive coupling is therefore disabled. Figure 12(c) shows a $\frac{\lambda}{2}$-resonator with qualitative voltage and current distribution.

From the above considerations, it is straightforward to write down the resonance frequency f of a $\frac{\lambda}{2}$-resonator, using the common relation between frequency f and wavelength λ and employing the phase velocity from equation (85).

$$f = \frac{v_P}{\lambda} = \frac{nc}{2l\sqrt{\epsilon_e}} \tag{87}$$

In equation (87), l denotes the length of the resonator strip, and

$$l = \frac{\lambda}{2} n \tag{88}$$

is used. n is the mode number and it is $n = 1$ for the fundamental mode.

Each transmission line has a certain characteristic impedance Z_0, which is defined as the ratio of maximum voltage to maximum current according to Ohm´s law. In general, the transmission line is terminated at one or both of its ends with a load impedance Z_L, being the resistance to ground, see figure 12(d). In case of a $\frac{\lambda}{2}$-resonator, $Z_L = \infty$, since the current at the ends vanishes.

For further analysis, it is expedient to calculate the input impedance Z_{in}, which is the impedance “seen” by a microwave when looking into the transmission line. Thus Z_{in} is the effective impedance, originating from the superposition of incident and reflected wave. According to [Poz98],

$$Z_{in} = \frac{Z_0}{i \tan(\beta l)} \tag{89}$$

for a $\frac{\lambda}{2}$-resonator. β is the propagation constant from equation (86) and l the length of the transmission line.

Since Z_{in} needs to diverge if the resonator is resonant, one can write

$$\beta l = \pi \left(1 + \frac{\omega - \omega_0}{\omega_0}\right), \tag{90}$$

introducing the angular frequency ω and the angular resonance frequency ω_0. Substitution into equation (89) yields for $\omega \approx \omega_0$

$$Z_{in} = \frac{Z_0 \omega_0}{i\pi(\omega - \omega_0)}. \tag{91}$$

This result can be compared [Gop08] to the impedance Z of an ordinary lumped-element parallel LC-resonator.

$$Z = \left(i\omega C + \frac{1}{i\omega L}\right)^{-1} = \frac{i\omega L}{1 - \omega^2 LC} = \frac{i\omega L}{1 - \frac{\omega^2}{\omega_0^2}} \overset{\omega\approx\omega_0}{\approx} \frac{i\omega L}{2\left(1 - \frac{\omega}{\omega_0}\right)} \approx \frac{1}{2iC(\omega - \omega_0)} \tag{92}$$

Here the Taylor expansion $x^2 \approx 2x - 1$ around $x_0 = 1$ is performed and the relation

$$\omega_0 = 1/\sqrt{LC} \tag{93}$$

is used. Comparing equations (91) and (92) gives

$$\begin{aligned} C &= \frac{1}{2}\mathcal{C}l \\ L &= \frac{2}{\pi^2}\mathcal{L}l. \end{aligned} \tag{94}$$

In these relations, the capacitance and inductance per unit length $\mathcal{C}$, $\mathcal{L}$ are introduced. Equations (94) can then be obtained with the relation $Z_0 = \sqrt{\mathcal{L}/\mathcal{C}}$ [Gop08]. As a result one can write

$$Z_0 = \frac{\pi}{2}\sqrt{\frac{L}{C}}. \tag{95}$$

Similar to equation (93), it is

$$\mathcal{C}\mathcal{L} = \frac{1}{v_P^2}. \tag{96}$$

The fact that $\mathcal{C}\mathcal{L}$ is a material constant is plausible since no information about the length l of the resonator is included in equation (96).

Another important parameter of a resonator is its quality factor Q, defined as [Poz98]

$$Q = \omega \frac{E}{P}, \tag{97}$$

with resonator angular frequency ω, the average energy stored in the resonator E and the energy dissipation rate P. Q is a measure of the loss of a resonator and therefore the lifetime of resonator modes.

The quality factor of the resonator itself is called the unloaded Q, or internal quality factor Q_i. In practice, the resonator is coupled to an external circuit, which produces additional losses. The total Q of the coupled resonator is called loaded quality factor Q_L and can be expressed as

$$Q_L^{-1} = Q_i^{-1} + Q_C^{-1}. \tag{98}$$

Q_C^{-1} denotes the loss contribution due to coupling of the resonator to its environment.

In the following, an expression that links the coupling quality factor Q_C and the coupling capacitance C is derived, which is very useful for designing a CQED system. A similar analysis is done in [Maz04].

Modelling a microwave resonator as a lumped-element parallel LC-resonator, which is valid close to its resonance, the average energy E stored in the resonator is just the sum of the energies E_C, E_L stored in the capacitor C_l and the inductor of the resonator, respectively. Since half of the total energy is stored in the capacitor and half is stored in the inductor on average, it is

$$E = E_C + E_L = 2 \cdot \frac{1}{2} C_l \langle V^2 \rangle = \frac{1}{2} C_l V_0^2. \tag{99}$$

One factor $\frac{1}{2}$ in equation (99) accounts for averaging the voltage square along the resonator line. The dissipation power P can be obtained by calculating the current flowing into the load [Maz04] of the resonator. For a resonator being capacitively coupled only on one end to a load of impedance Z_0, it is

$$P = \langle I_0^2 \rangle Z_0 = \frac{1}{2} \omega_0^2 C^2 V_0^2 Z_0. \tag{100}$$

It is assumed that the absolute value of the coupling impedance is dominated by the coupling capacitor.

Inserting into equation (97) yields for $\omega \approx \omega_0$

$$Q_C = \frac{\omega_0 C_l}{Z_0 \left(\omega_0 C\right)^2} = \frac{\sqrt{C_l / L}}{Z_0 \left(\omega_0 C\right)^2} = \frac{l}{v_P Z_{res} Z_0 \left(\omega_0 C\right)^2} = \frac{\pi}{Z_{res} Z_0 \left(\omega_0 C\right)^2}, \tag{101}$$

using equations (93), (96) and denoting the characteristic resonator impedance with Z_{res}. Equation (101) holds for a $\frac{\lambda}{2}$-wavelength resonator.

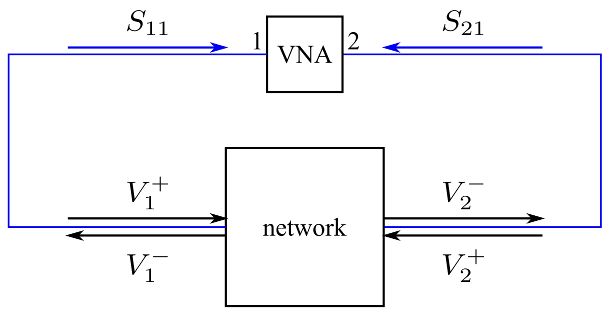

Figure 13: Typical measurement setup of a two-port network using a vector network analyzer (VNA), with microwaves being applied at port 1. Incident and originating voltage amplitudes $V_i^{\pm}$ as well as the corresponding scattering matrix elements are depicted.

4.3 Resonator characterization using the scattering matrix

A very convenient representation for the characterization of multi-port networks is given by the scattering matrix $\overline{\overline{S}}$. In contrast to an impedance matrix approach, where voltages and currents at the ports are considered, incident and reflected voltage waves on the ports of a network are related [Poz98]. For this reason, the scattering matrix representation is closely linked to direct measurements of a multi-port network, for instance with a vector network analyzer (VNA).

For the usual case of a two-port network,

$$\begin{pmatrix} V_1^- \\ V_2^- \end{pmatrix} = \begin{pmatrix} S_{11} & S_{12} \\ S_{21} & S_{22} \end{pmatrix} \begin{pmatrix} V_1^+ \\ V_2^+ \end{pmatrix}, \tag{102}$$

with V_i^+ the voltage amplitude of an incident wave on port i and V_i^- the voltage amplitude of a wave originating from port i. Since the amplitudes $V_i^{\pm}$ are complex values in general, both amplitude and phase information is contained in the scattering description.

The characterization of a notch-type resonator is carried out using a feedline to which the resonator is coupled. The ends of the feedline may be ports 1, 2 of the network. For a typical measurement, a VNA is connected in such a way, that a wave is applied at port 1. For no wave being applied at port 2, equation (102) reduces to

$$\begin{pmatrix} V_1^- \\ V_2^- \end{pmatrix} = \begin{pmatrix} S_{11}V_1^+ \\ S_{21}V_1^+ \end{pmatrix}. \tag{103}$$

Now one can measure either the reflection of the wave back to port 1, S_{11}, or the transmitted wave signal to port 2, S_{21}. Figure 13 shows a typical measurement setup of a two-port network using a VNA for this scenario.

In the present work, a transmission line resonator is coupled to a feedline, which is connected to a VNA. The feedline can be regarded as a transmission line as well. Its characteristic impedance is $50\,\Omega$, equal to the impedance of the coaxial cables

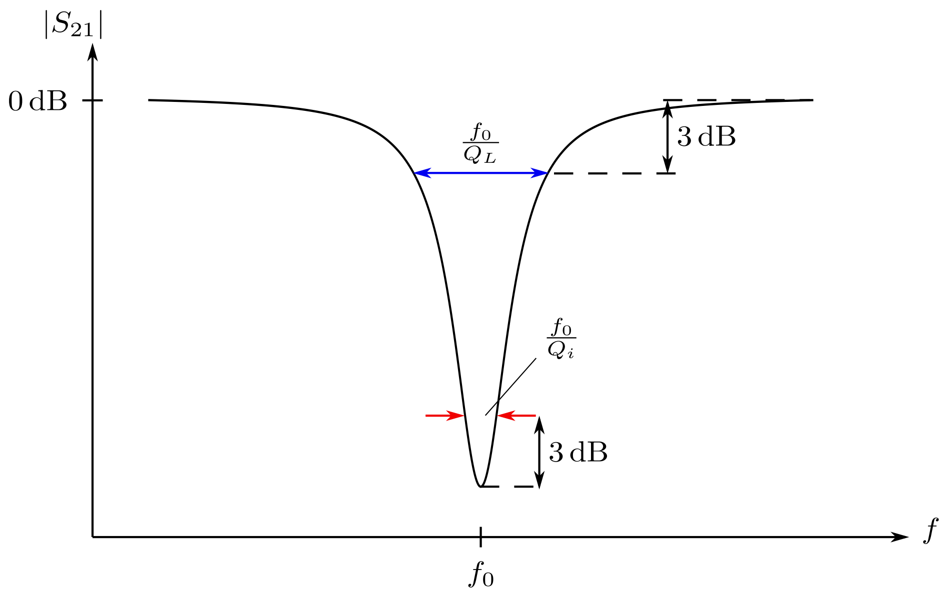

Figure 14: Typical transmission amplitude spectrum $|S_{21}|$ of a notch-type resonator capacitively coupled to a feedline. The loaded quality factor Q_L is calculated from the bandwidth at $\sqrt{2}$ times or 3 dB below the baseline of unity transmission, corresponding to 0 dB. The internal quality factor Q_i is calculated from the bandwidth at $\sqrt{2}$ times or 3 dB above the minimum of the dip.

connected, to avoid wave reflections at the ends of the feedline due to an impedance mismatch. The resonator is characterized by measuring reflection or transmission of microwaves at the feedline.

Measuring the transmission amplitude spectrum $|S_{21}|$ of such a notch-type resonator, a dip occurs at its resonance frequency. This is due to photon modes being excited in the resonator and reradiated into the feedline. Since these waves originating from the resonator are travelling in both directions of the feedline, the transmitted signal is attenuated. Modes of other frequencies than the resonance frequency do not couple to the resonator and are fully transmitted. In this respect, the configuration works as a notch filter.

The width of the observed dip corresponds to the quality factor Q of the respective resonator. According to [Poz98], the internal quality factor Q_i and the loaded quality factor Q_L can be measured at $\sqrt{2}$ times above the minimum of S_{21} and $\sqrt{2}$ times below the baseline corresponding to unity transmission, respectively. Figure 14 shows a typical transmission spectrum of a notch-type resonator.

Chapter III Experiment

1 Design and simulation of the transmon CQED system

The transmon CQED system investigated in this work is schematically depicted in figure 15(a). As mentioned in section II.4, the device is designed in microstrip geometry. All components are essentially located in two dimensions, which is the plane just above the substrate. Since a crucial part of electric field lines penetrates the bulk substrate, this geometry is sometimes called “2.5 dimensional”.

The substrate material employed is intrinsic silicon due to its large internal quality factor $Q_i > 10^6$ [Vis10]. The reason is the small concentration of two-level systems in the dielectric, which is the main limitation of Q_i. For the structured metal layer as well as the ground plane below the substrate, aluminum is used. It is known to be highly performant when it comes to high Q_i resonators [Wan09], promising increased coherence times of the qubit. A schematic chip profile is shown in figure 15(b).

To avoid an impedance mismatch at the ends of the feedline, its impedance is designed to be close to $50\,\Omega$, which is the wave impedance of the connected coaxial cables. The appropriate width W can be calculated according to [Poz98] as

$$W = d\frac{8e^A}{e^{2A}-2}, \quad A = \frac{Z_0}{60\,\Omega}\sqrt{\frac{\epsilon_r+1}{2}} + \frac{\epsilon_r-1}{\epsilon_r+1}\left(0.23+\frac{0.11}{\epsilon_r}\right), \tag{104}$$

with d the substrate thickness, Z_0 the given characteristic impedance of $50\,\Omega$ and ϵ_r the dielectric constant of the substrate. For $d = (350 \pm 5)\,\mu$m and $\epsilon_r = 11 \pm 0.2$ for silicon, equation (104) yields $W = (305 \pm 7)\,\mu$m, assuming a Gaussian error propagation. The effective dielectric constant ϵ_e for the parameters given in figure 15 is according to equation (84)

$$\epsilon_e = 6.24. \tag{105}$$

In the present design, a $\frac{\lambda}{2}$-resonator is capacitively coupled to the feedline via the capacitance C_{in}.

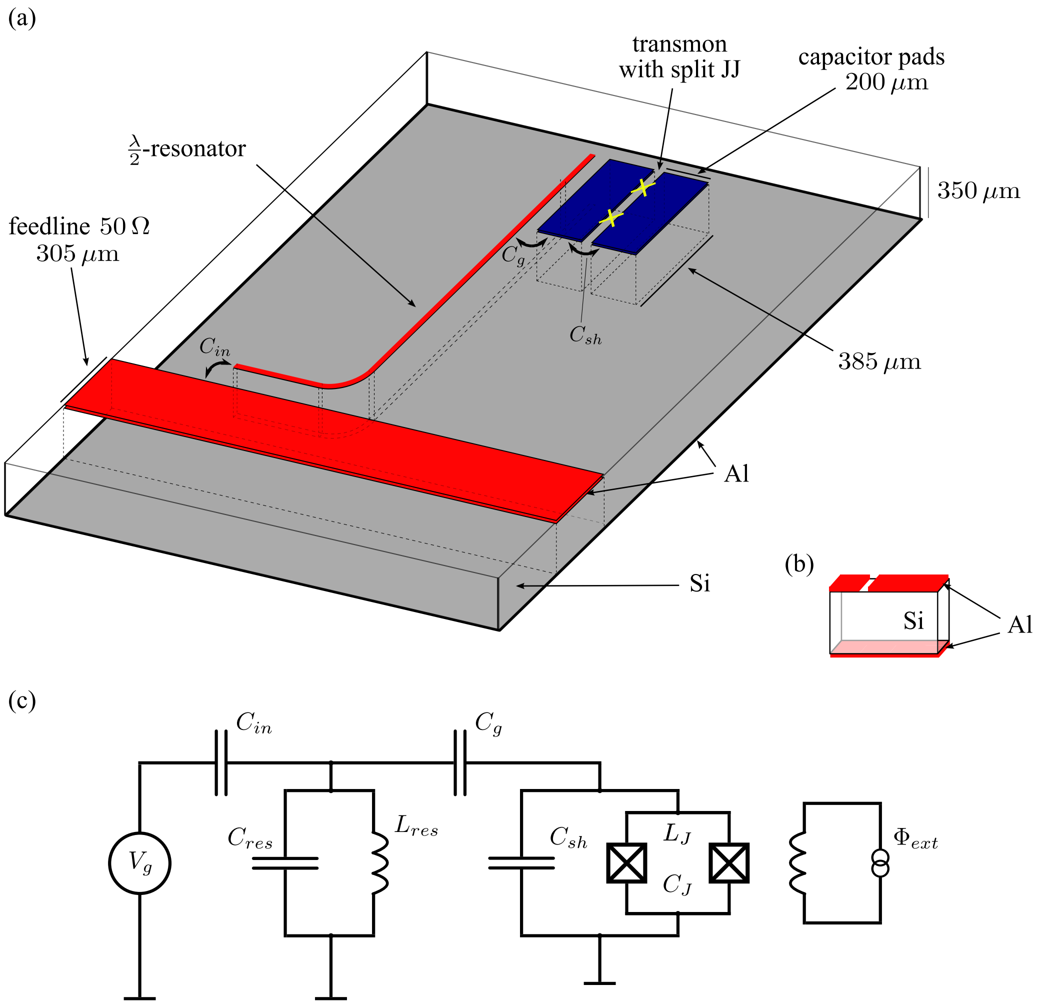

Figure 15: (a) Schematic of the transmon CQED system investigated in this work. Feedline and readout resonator are shown in red, the transmon with its capacitor pads in blue. Josephson junctions are depicted as yellow crosses. (b) Chip profile. The structured layer on top as well as the ground plane below the silicon substrate is patterned with aluminum. (c) Equivalent circuit diagram. The feedline is identified with a gate voltage V_g and the resonator with a lumped-element LC-resonator. An external flux loop for tuning the transmon is depicted as well.

The large shunt capacitance of the transmon is realized by two adjacent pads. This configuration can be mapped to a parallel plate capacitor with a mutual capacitance that partly features the shunt capacitance C_{sh}. The dominant contribution however arises from the capacitive coupling of the two pads to the ground plane and therefore to each other by means of the electric field. The large size and spacing of the capacitor pads reduce the surface loss contribution by reducing the electric field strength at the surface.

The capacitor pads are connected by two Josephson junctions depicted as yellow crosses in figure 15(a). This so called split Josephson junction setup corresponding to a dc-SQUID allows the transmon to be tunable in its resonance frequency via external flux.

The transmon as a whole likewise couples to the resonator via the gate capacitance C_g.

An equivalent circuit diagram of the CQED system is depicted in figure 15(c). The feedline is identified with a gate voltage V_g and the $\frac{\lambda}{2}$-resonator is approximated by a lumped-element parallel LC-oscillator. The external magnetic flux Φ_{ext} induces a current in the dc-SQUID loop and alters the effective critical current of the split Josephson junction.

Since the London penetration depth λ_L of aluminum is roughly in the range of the thickness of the ground plane of the chip, concerns regarding a possible magnetic screening by the backplane are dispelled.

The behaviour of the transmon CQED system depends strongly on the chosen design and fabrication parameters. In the following, design parameters to operate the transmon in the desired regime together with chip simulations to determine the relevant frequencies and quality factors are given. The simulations are mainly performed with Sonnet [Son11], which is a simulation software for high frequency circuits.

1.1 Design parameters of the readout resonators

Figure 16(a) shows a micrograph of the transmon chip prepared in this work with an edge length of 5 mm. It comprises the feedline traversing the chip in the middle and four pairs of readout resonators with associated transmon.

While each transmon on the chip is identical, the resonators are mutually detuned with resonance frequencies in the range from 6 GHz to 9 GHz. This allows to choose the readout resonator most suitable for a certain measurement.

According to Sonnet simulations, the resonance frequencies turn out to be higher than expected from equation (87). The reason is the meander geometry of the resonators that leads to partial cancellation mainly of the inductance of the resonators´ striplines.

The simulated reflection amplitude spectrum is given in figure 17(a).

The loaded quality factors Q_L of the resonators are calculated according to figure 14 from the dips in the simulated transmission amplitude $|S_{21}|$, shown exemplarily

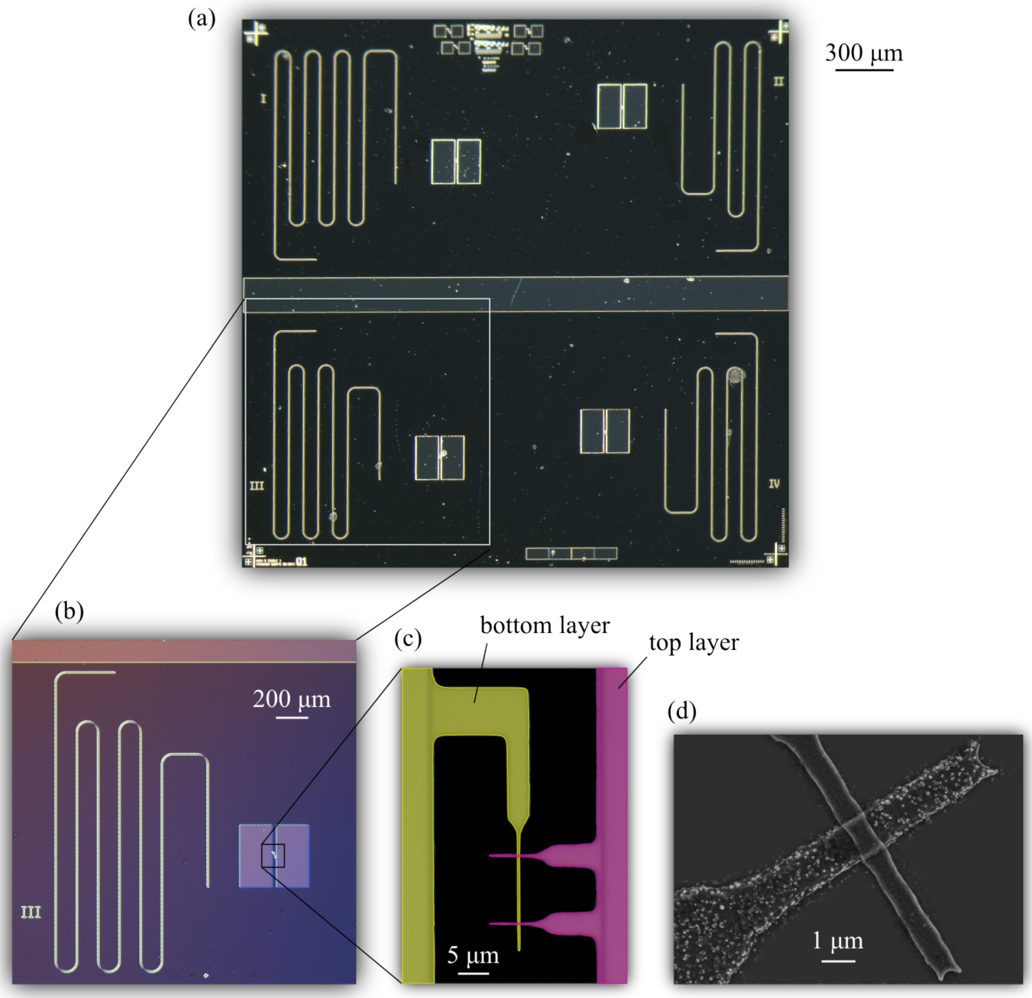

Figure 16: Micrograph of the transmon CQED system prepared and investigated in this work. (a) Whole chip with feedline traversing in the middle and four pairs of transmon qubits with associated readout resonator. (b) Enlarged section of the chip showing the 7 GHz resonator with transmon qubit. (c) Optical image of a split Josephson junction with an inner area of 120 μm^2. Bottom layer (yellow) and top layer (pink) are coloured. (d) Detailed scanning electron microscope (SEM) image of a Josephson junction (S. Meißner). Bright spots on the bottom electrode can be ascribed to a contamination during the stripping process.

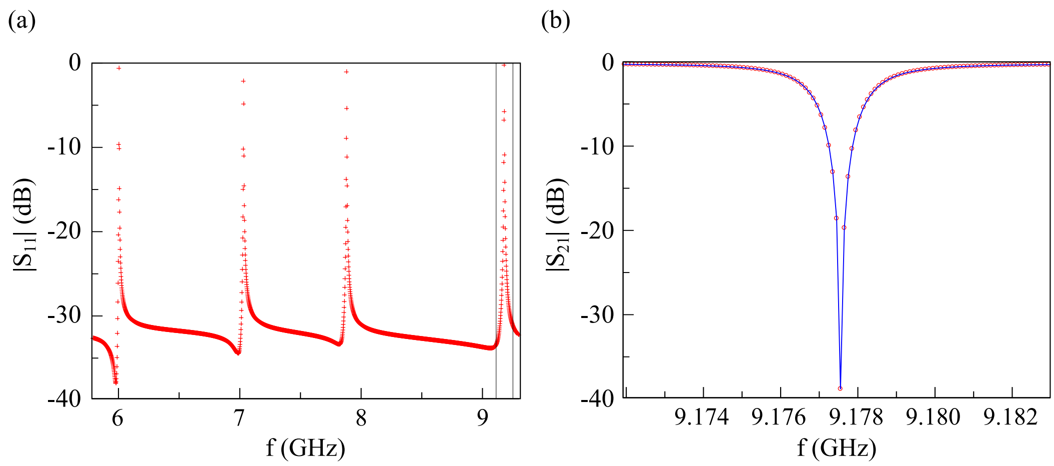

Figure 17: (a) Simulated reflection amplitude $|S_{11}|$ of the readout resonators. The quality factors Q_L given in table 1 are calculated from the respective transmission spectra due to a defined base line. (b) Enlarged view of the transmission amplitude $|S_{21}|$ of the 9 GHz resonator.

Table 1: Resonance frequencies f_0 and loaded quality factors Q_L of the readout resonators according to a simulation of the transmission amplitude spectrum $|S_{21}|$. Q_L is determined according to figure 14.

resonator	f_0 (GHz)	Q_L (10^3)
1	6.01	5.5
2	7.04	5.0
3	7.88	5.3
4	9.18	5.1

in figure 17(b). The target value is $Q_L = 5000$. Table 1 gives an overview of the simulated resonance frequencies and the loaded quality factors Q_L of the four readout resonators. To achieve an equal coupling for all resonators, the distance of the coupler to the feedline needs to be adjusted due to the varying maximum voltage in the coupler for different resonator lengths.

Since the internal loss of the resonators vanishes under ideal conditions that are assumed in the simulation, $Q_i \to \infty$ and $Q_L = Q_C$ according to equation (98). Therefore Q_L is a direct measure of the coupling between feedline and resonator.

The resonator width is $W_{res} = 10\,\mu\text{m}$. Employing the inverse of equation (104) [Poz98], the off-resonance characteristic impedance Z_{res} of the resonators is

$$Z_{res} = (135 \pm 3)\,\Omega. \tag{106}$$

Using equation (96) and $Z_{res} = \sqrt{\mathcal{L}/\mathcal{C}}$, the capacitance $\mathcal{C}$ and inductance $\mathcal{L}$ per unit length of the resonators can be calculated. Equations (93) and (95) give the capacitance C and the inductance L of the resonators when identified with lumped-element LC-resonators for a certain resonance frequency f_0. The parameters for the 8 GHz resonator are

$$\begin{aligned} C &= 231\,\mathrm{fF}, \\ L &= 1.7\,\mathrm{nH}. \end{aligned} \tag{107}$$

1.2 Design parameters of the transmon

The properties of the transmon are strongly dependent on the parameters of the employed Josephson junctions.

For a target Josephson junction area of $A = 0.5\,\mu\mathrm{m}^2$, the intrinsic capacitance C_{int} of a single Josephson junction is

$$C_{int} = 25\,\mathrm{fF}, \tag{108}$$

assuming a specific capacitance of $50\,\frac{\mathrm{fF}}{\mu\mathrm{m}^2}$ for $\mathrm{AlO_x}$, which is the utilised material of the tunnelling barrier. The resistance-area product R_nA, which is a characteristic parameter of the oxide barrier, has to be

$$R_nA = 2000\,\Omega\mu\mathrm{m}^2. \tag{109}$$

With the relation from Ambegaokar and Baratoff [Amb63, Tin04] for the I_cR_n-product of tunnel junctions,

$$I_cR_n = \frac{\pi\Delta}{2e}\tanh\left(\frac{\Delta}{2k_BT}\right), \tag{110}$$

the critical current I_c of the Josephson junction can be calculated to be

$$I_c = 65\,\mathrm{nA}. \tag{111}$$

In equation (110), $R_n = R_nA/A$ is the sheet resistance of the Josephson junction, Δ is the superconducting gap of aluminum and T is the measuring temperature, which is assumed to be 15 mK.

According to equation (33), the inductance L_J of the split Josephson junction for vanishing external flux is

$$L_J = 2.5\,\mathrm{nH}. \tag{112}$$

To simulate the transmon with Sonnet, the split Josephson junction needs to be substituted by an ideal capacitance $C_J = 2C_{int}$ together with an ideal inductance L_J with the values from equations (108) and (112), respectively.

To work out the transmon frequency f_T, its readout resonator is regarded as a feedline with the transmon as lumped-element LC-resonator being capacitively coupled to. The ports at the ends of the feedline are grounded by a load corresponding to the resonator´s characteristic impedance Z_{res} given in equation (106). Measuring the transmission amplitude spectrum $|S_{21}|$ yields the transmon frequency f_T as well as the loaded quality factor $Q_{L,q}$ of the transmon. Analogously, $Q_{L,q}$ gives the coupling $Q_{C,q}$ between resonator and transmon.

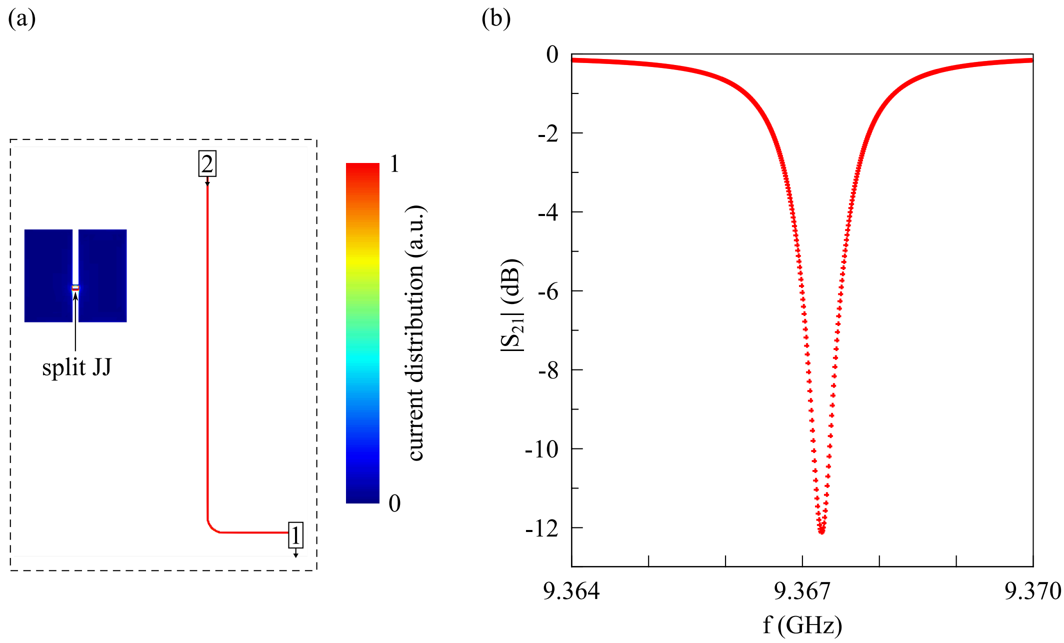

Figure 18: (a) Geometry used for simulating the transmon frequency f_T and its coupling Q_C to the resonator with colours indicating the current distribution. As the current vanishes on the capacitor pads, inductive coupling between resonator and transmon for this simulation can be excluded. (b) Transmission amplitude $|S_{21}|$ of the geometry shown in (a). The simulated transmon frequency is $f_T = 9.37\,\mathrm{GHz}$ and the loaded quality factor is $Q_L = 10.4 \cdot 10^3$.

Figure 18(a) shows the simulated current distribution on the resonator and the transmon. Since the current is zero on the capacitor pads, inductive coupling can be excluded and the measured $Q_{L,q}$ directly translates into the gate capacitance C_g.

The transmission amplitude shown in figure 18(b) indicates a transmon frequency of

$$f_T \approx 9.37\,\mathrm{GHz} \tag{113}$$

and a loaded quality factor for the transmon of

$$Q_{L,q} \approx 10^4. \tag{114}$$

Assuming that the inductance of the split Josephson junction L_J is large compared to the inductance of the capacitor pads, the total transmon capacitance C_Σ can be calculated using equation (93):

$$C_\Sigma = 115\,\mathrm{fF} \tag{115}$$

Inserting the parameters from equations (112), (115) into equations (22), (44), the Josephson energy E_J and charging energy E_C as well as their ratio can be calculated to be

$$\begin{aligned} E_J &= 0.27\,\mathrm{meV} \\ E_C &= 0.70\,\mu\mathrm{eV} \\ E_J/E_C &= 386. \end{aligned} \tag{116}$$

1.3 The split Josephson junction

Since the transmon in the current design employs two Josephson junctions, the effective critical current $I_{c,eff}$ of this split Josephson junction is the relevant quantity. With zero external magnetic flux applied, it is $I_{c,eff} = 2I_c$.

According to figure 19(a) and the Josephson equation (20), the total current flowing through a symmetric split Josephson junction is

$$I_{tot} = I_1 + I_2 = I_c\left(\sin\delta_1 + \sin\delta_2\right) = 2I_c \cos\left(\frac{\delta_1 - \delta_2}{2}\right)\sin\left(\frac{\delta_1 + \delta_2}{2}\right). \tag{117}$$

Integration around the loop formed by the two Josephson junctions while taking into account the direction of the currents yields the applied external magnetic flux Φ_{ext} due to flux conservation shown in section I.1.1.

$$\delta_1 + (-\delta_2) = 2\pi\frac{\Phi_{ext}}{\Phi_0} \tag{118}$$

Inserting equation (118) into equation (117) gives the maximum effective critical current of the split Josephson junction $I_{c,eff}$ dependent on external magnetic flux Φ_{ext}:

$$I_{c,eff} = 2I_c \cos\left(\pi\frac{\Phi_{ext}}{\Phi_0}\right) \tag{119}$$

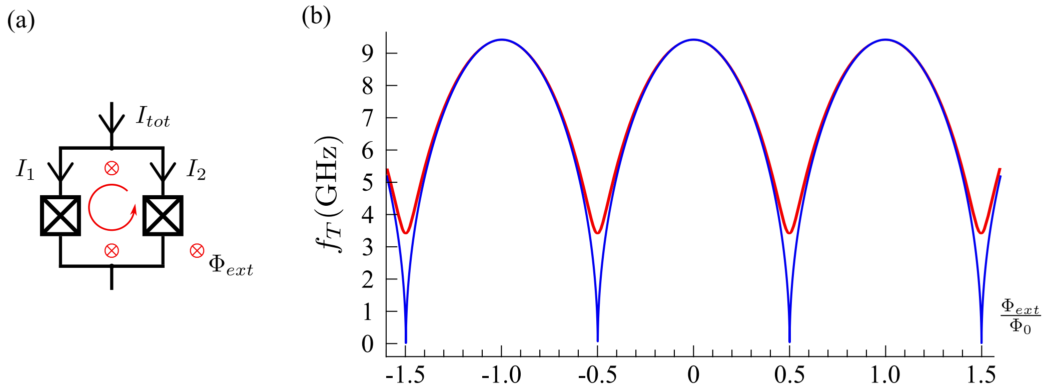

Figure 19: (a) Split Josephson junction with total current I_{tot}. While integrating around the loop indicated in red, the phase jumps δ_i at the Josephson junctions need to sum up to the overall phase of the loop evoked by the external flux Φ_{ext}. (b) Dependence of the transmon frequency f_T on the externally applied flux Φ_{ext}, normalized to the flux quantum Φ_0. By inducing integer multiples of $\frac{\Phi_0}{2}$ in the loop, the qubit frequency ideally vanishes for a symmetric split Josephson junction (blue). An asymmetry of the split Josephson junction by 15% leads to a reduced tuning range, shown in red.

The tunability of the transmon´s resonance frequency f_T by applying an external magnetic flux Φ_{ext} is depicted in figure 19(b). Since f_T has its maximum for vanishing Φ_{ext}, the resonance frequency of the transmon is designed to be slightly above the resonances of the readout resonators. This allows to operate the transmon in the dispersive regime for large detuning as well as to observe an avoided level crossing when sweeping the transmon on resonance with its readout resonator.

In the case where the split Josephson junction is asymmetric, the total current I_{tot} takes the form

$$\begin{aligned} I_{tot} &= I_{c,1}\sin\delta_1 + I_{c,2}\sin\delta_2 \\ &= I_{c,1}\sin\delta_1 + I_{c,1}\sin\delta_2 - I_{c,1}\sin\delta_2 + I_{c,2}\sin\delta_1 - I_{c,2}\sin\delta_1 \\ &\quad + I_{c,2}\sin\delta_2 + I_{c,1}\sin\delta_1 + I_{c,2}\sin\delta_2 - I_{tot} \\ &= 2\left(I_{c,1}+I_{c,2}\right)\cos\left(\pi\frac{\Phi_{ext}}{\Phi_0}\right)\sin\delta \\ &\quad + 2\left(I_{c,2}-I_{c,1}\right)\cos\delta\sin\left(\pi\frac{\Phi_{ext}}{\Phi_0}\right) - I_{tot}. \end{aligned} \tag{120}$$

Solving for I_{tot} yields

$$\begin{aligned} I_{tot} &= I_{c,\Sigma}\left[\cos\left(\pi\frac{\Phi_{ext}}{\Phi_0}\right)\sin\delta + d\cos\delta\sin\left(\pi\frac{\Phi_{ext}}{\Phi_0}\right)\right] \\ &= I_{c,\Sigma}\cos\left(\pi\frac{\Phi_{ext}}{\Phi_0}\right)\left[\sin\delta + d\cos\delta\tan\left(\pi\frac{\Phi_{ext}}{\Phi_0}\right)\right], \end{aligned} \tag{121}$$

where $I_{c,\Sigma} = I_{c,1} + I_{c,2}$, $\delta = \frac{1}{2}(\delta_1 + \delta_2)$ and $d = \frac{I_{c,2}-I_{c,1}}{I_{c,\Sigma}}$, being the asymmetry parameter.

Applying cosine´s addition theorem to isolate the phase δ in a factor that can be eliminated afterwards [Koc07] gives

$$I_{c,eff} = 2I_c \cos\left(\pi\frac{\Phi_{ext}}{\Phi_0}\right)\sqrt{1 + d^2\tan^2\left(\pi\frac{\Phi_{ext}}{\Phi_0}\right)}, \tag{122}$$

with $I_{c,\Sigma} \approx 2I_c$.

Due to the correction term in equation (122), which becomes unity for a symmetric split Josephson junction with $d = 0$, the transmon frequency cannot be tuned to zero frequency, which is shown in figure 19(b) in red.

The designed inner area of the split Josephson junction is $120\,\mu\text{m}^2$.

1.4 Design parameters of the CQED system

According to [Koc07], the coupling constant g between resonator and transmon can be expressed as

$$g_{ij} = \frac{2\beta e}{\hbar}V_{rms}\langle i|\hat{n}|j\rangle \tag{123}$$

with i, j being transmon states. The relevant quantity to insert in equation (69) is g_{01}, corresponding to the transition between the transmon eigenstates $|0\rangle$, $|1\rangle$. Expressing the number operator $\hat{n}$ in terms of qubit creation and annihilation operators yields

$$g_{01} = \frac{\sqrt{2}\beta e V_{rms}}{\hbar}\sqrt{\frac{E_J}{8E_C}}. \tag{124}$$

V_{rms} is the root-mean-square voltage of the resonator corresponding to its vacuum fluctuations. It can be extracted by equating the energy stored in the capacitor of the resonator $\frac{1}{2}C_{res}V^2 = C_{res}V_{rms}^2$ and the vacuum fluctuation of a harmonic oscillator $\frac{1}{2}\hbar\omega_{res}$. One obtains

$$V_{rms} = \sqrt{\frac{\hbar\omega_{res}}{2C_{res}}}. \tag{125}$$

β in equation (123) is defined as

$$\beta = \frac{C_g}{C_\Sigma} \tag{126}$$

with C_g the gate capacitance and C_Σ to total transmon capacitance. The gate capacitance C_g can be calculated using equation (101) and $Q_{L,q}$ from equation (114) to be

$$C_g = 2.1\,\text{fF}. \tag{127}$$

Putting things together, equation (124) yields for the 8 GHz resonator

$$g_{01} = 149\,\text{MHz}. \tag{128}$$

The effective dispersive shift χ_{eff} can be calculated according to [Koc07] as

$$\chi_{eff} = -\left(\beta e V_{rms}\right)^2 \sqrt{\frac{E_J}{2E_C}} \frac{E_C}{\hbar\Delta(\hbar\Delta - E_C)} \tag{129}$$

which gives

$$\chi_{eff} = 2.34\,\mathrm{MHz}. \tag{130}$$

The effective loss tangent δ of the transmon with split Josephson junction is approximately

$$\delta = \frac{2C_{int}}{C_\Sigma}\delta_{AlO_x} + \left(1 - \frac{2C_{int}}{C_\Sigma}\right)\delta_{Al} \approx \frac{2C_{int}}{C_\Sigma}\delta_{AlO_x}, \tag{131}$$

assuming $\delta_{Al} \ll \delta_{AlO_x} \approx 3\cdot 10^{-3}$ [Pai10]. The relaxation time T_1 of the investigated transmon is estimated to be

$$T_1 \approx \frac{1}{\delta\, f_T} = \frac{C_\Sigma}{2C_{int}\delta_{AlO_x} f_T} \approx 0.1\,\mu\mathrm{s}. \tag{132}$$

For the single junction version of the transmon, a relaxation time up to $0.3\,\mu$s is expected due to the smaller effective junction area and no magnetic flux noise sensitivity.

The upper bound T_1^P of the transmon´s relaxation time given rise by the Purcell effect can be estimated using equation (83) to be

$$T_1^P = 53\,\mu\mathrm{s} \tag{133}$$

which does not constitute a limitation in the present case.

Using equation (61) for the eigenenergies E_m of the transmon Hamiltonian, the anharmonicity α of the transmon system defined in equation (56) can be calculated to be

$$\alpha = 169\,\mathrm{MHz}. \tag{134}$$

According to equation (57), this corresponds to a relative anharmonicity of

$$\alpha_r \approx 1.8\,\%. \tag{135}$$

Since $\alpha \gg 1/T_2 \approx 1/T_1$, which roughly corresponds to the excitation peak broadening, this is sufficient to distinguish the fundamental transmon transition from higher level excitations.

2 Sample fabrication

All samples investigated in this work are fabricated at the Karlsruhe Institute of Technology. The only metal employed for the samples, including the electrodes of the Josephson junctions, is aluminum which is deposited using the sputter deposition tool “Plasma 1” of the Physikalisches Institut. Structuring of the metal layers

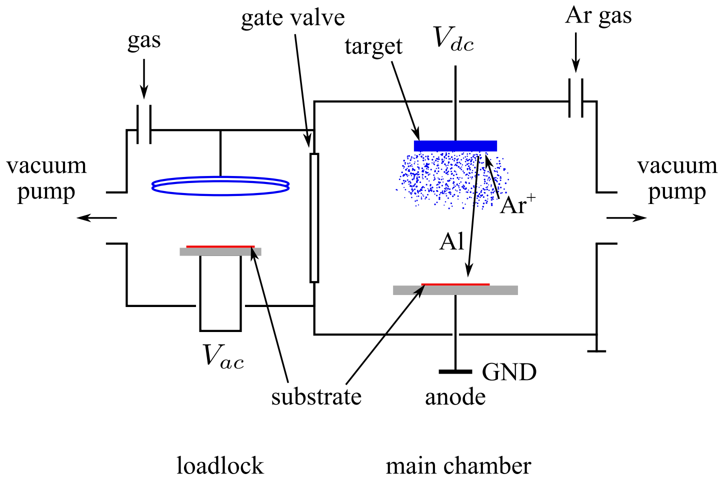

Figure 20: Schematic of the magnetron sputter deposition tool employed for sample preparation. The loadlock is shown on the left, where sputter cleaning and oxidation take place. The additional top ground plane inserted to improve the cleaning process is depicted in blue. The main chamber is shown on the right, with sampleholder (grey) and target (blue). The substrate is depicted in red and the chambers are separated by a gate valve.

is performed by optical lithography in the cleanroom of the Center for Functional Nanostructures (CFN).

The crucial and also most challenging part in fabricating a qubit based on superconducting devices is the preparation of Josephson junctions. To figure out fabrication procedures and parameters as well as to characterize the Josephson junctions used for the transmon investigated in this work, samples comprising only Josephson junctions of different size and design were prepared.

Since fabricating the transmon samples does not require any technological advancement relative to fabricating Josephson junctions only, the following sections focus on Josephson junction preparation.

2.1 Sputter deposition and argon cleaning

A schematic of the magnetron sputter deposition tool employed for sample preparation is depicted in figure 20.

Metal deposition takes place in the main chamber. In general, the previously evacuated chamber is filled with argon gas up to 0.1 mbar and a high negative dc-voltage is applied at the metal target, also called gun. Due to the high electric field between substrate and target, the argon atoms are spontaneously ionized and therefore a plasma is ignited. The positively charged ions are accelerated onto the target and ballistically scatter with the metal atoms. These sputter atoms leave the target and are partly deposited on the substrate.

In magnetron sputtering, a magnetic field is applied parallel to the target´s surface [Was04]. This leads to a trapping of electrons in the glow discharge region of the plasma which in turn increases the collision rate between electrons and argon atoms. Due to this increased ionisation rate, the sputtering pressure can be lowered down to typically 10^{-3} mbar which reduces the scattering probability of the sputter atoms while travelling to the substrate. This results in a highly increased deposition rate. Since the scattering angle between incident argon ion and scattered atom is predictable, the deposition rate is further increased by means of the magnetic field due to a focusing of the argon ions from a certain angle.

The aluminum deposition rate for the extended gun was determined to be about $0.4\,\frac{\mathrm{nm}}{\mathrm{s}}$, with a sputter power of 300 W and a dynamically pumped chamber pressure during deposition of $1.3 \cdot 10^{-3}$ mbar. The chamber background pressure is $3 \cdot 10^{-8}$ mbar.

The left part in figure 20 shows the loadlock of the sputter deposition tool where the RF-sputter clean process takes place. As the term suggests, it can be regarded as an opposite sputtering process.

As depicted in figure 20, the sample and sampleholder are connected to a high ac-voltage of 13.56 MHz after filling the loadlock chamber with argon gas. This again leads to ionisation and an acceleration of the argon ions which scatter with metal atoms on the sample. Due to the momentum transfer, they leave the sample and the result is an erosion of the sample´s metal layer corresponding to an etching process.

There are two major challenges one has to deal with during this process. First of all, redeposition on the sample of eroded material as well as material from the chamber walls, the copper stamp and the substrate holder has to be avoided. While this is achieved by ensuring a high net cleaning rate, one can get rid of oxygen or hydrogen traces by an increased pumping power while maintaining the chamber pressure. A second challenge is to focus the argon plasma to the region where the sample is located. Otherwise particle erosion taking place elsewhere can ultimately lead to a net deposition rate on the substrate.

In the course of optimizing parameters, the sputter clean rate was measured to be marginal and a substantial amount of material was redeposited inhomogeneously on the substrate. A first reason for that was a stainless steel shield beneath the substrate stamp that magnetised progressively over time and thus redirected the plasma away from the sample. The key improvement of the cleaning rate was induced by a ground plane with a diameter of 13 cm which was inserted about 5 cm above the sampleholder. Before, the chamber walls were the only ground reference for the plasma. Since they were nearest below the sampleholder, the plasma was mainly located there. The close ground plane above the sample now focuses the plasma just on top of the sampleholder and largely increases its homogeneity. In addition, no metal redeposition is observed or measured after the modification. The enhanced cleaning rate $R_c \approx 3.3\,\mathrm{nm/min}$ due to the increased effective area A_G of the ground plane accords with the relation

$$R_c \propto \left(\frac{A_G}{A_s}\right)^4 \tag{136}$$

from [Ohr02], with A_s being the area of the sampleholder.

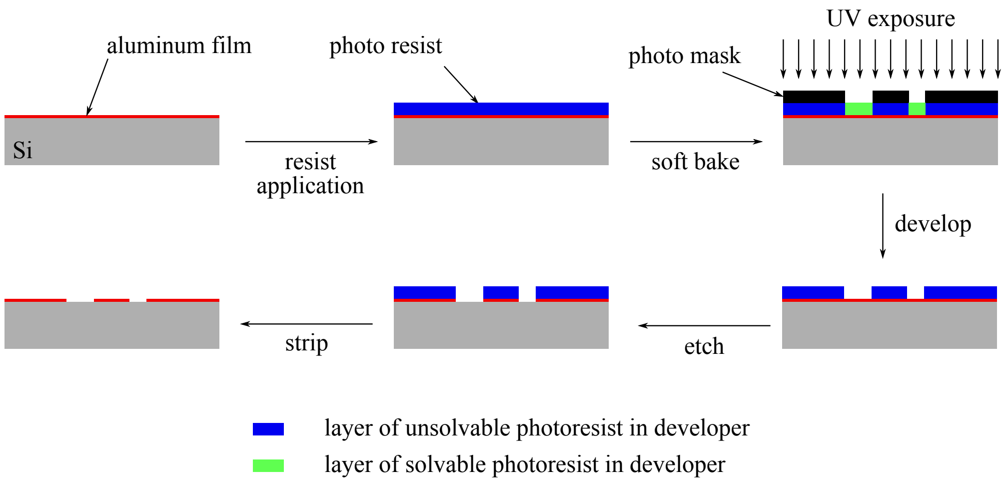

Figure 21: Schematic representation of the positive optical lithography process used for structuring the samples. The photoresist (blue) is applied and structured on top of the deposited aluminum film. Exposed regions (green) are developed and the aluminum is removed at regions not protected by the photoresist in a subsequent etching process. Finally, the photoresist is stripped.

Since the sample is heated up to about 80°C during continuous cleaning in spite of water cooling, regular pauses are necessary to avoid a crystal structure degrading. In addition, such high sample temperatures would have a severe influence on the subsequent oxidation process. For this purpose, the cleaning process is automated by the implementation of software control including monitoring the reflected power of the RF source. In a further step, continuous pressure readout and logging for loadlock and main chamber are implemented to enable process reproducibility.

Exact sputter deposition and cleaning parameters are given in appendix A.2.

2.2 Optical lithography

The optical lithography process used to structure the deposited aluminum films is schematically depicted in figure 21.

The employed photoresist is AZ5214E, which is applied on top of the aluminum film in a two-step process using the spin coater. In the first step, the whole chip is covered homogeneously with a low spinning frequency of $500\,\frac{1}{\text{min}}$, while the thickness of the photoresist is adjusted in a second step with higher frequency. The desired thickness of about $1\,\mu$m corresponds to a spinning frequency of $6000\,\frac{1}{\text{min}}$ for 60 s. Remaining solvents in the applied photoresist are removed in a subsequent softbake step that also further increases the mechanical stability [Mic12].

The actual structuring is done using a chrome photomask which is written with direct write laser lithography (DWL). The photo mask is aligned above the substrate with a mask aligner from Carl Süss and brought in direct contact with the substrate. During the exposure process with ultra violet light in the range of 400 nm,

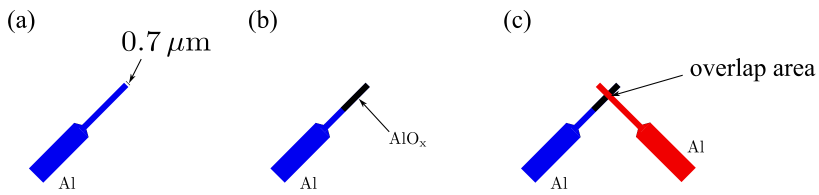

Figure 22: Principle sketch of the Josephson junction fabrication process using the cross junction technique. The first aluminum layer (blue) is structured and oxidized in a controlled way before patterning a second tip (red) on top, rotated by 90°.

intermolecular bonds in the photoactive compound are destroyed and exposed regions become soluble in the subsequent development step. Development is carried out with MIF726.

This process is called positive lithography, since direct mask reproduction on the photoresist takes place.

The structure in the photoresist layer is imaged to the aluminum film below in a dry etching process employing an inductively coupled plasma (ICP), which is a form of reactive ion etching (RIE). The process uses argon for physical ballistic etching as well as a small admixture of chlorine to avoid the formation of edge spikes.

In a final stripping process, the resist is removed from the sample.

Exact lithography parameters used for sample fabrication are given in appendices A.3 to A.6.

2.3 Josephson junction fabrication using the cross junction technique

The utilised substrate material is ultra-pure intrinsic double-side polished silicon with a thickness of 350 μm. To obtain the geometry shown in figure 1(a), the cross junction technique depicted in figure 22 is used.

In this two-step process, a first aluminum layer is prepared as a thin bar with a width of about 0.7 μm. Since structuring is carried out ex-situ, an oxide layer is formed at the surface of the aluminum film. This native oxide is removed in a cleaning step described in section 2.1 and the aluminum film is reoxidized in a controlled way. This layer of aluminum oxide with a thickness of about 2 nm forms the dielectric of the Josephson junction.

Subsequently, another aluminum layer is sputtered on top in-situ, structured as a finger rotated by 90°. The resulting overlap region of the aluminum layers is the Josephson junction area with an objective size of 0.5 μm^2.

The structuring of the aluminum layers is carried out in the way described in section 2.2.

To guarantee a proper contact between the two aluminum films and to avoid a disconnection of the second layer due to steep edges in the first layer, a positive edge profile in the first aluminum film needs to be assured. This can be achieved in a positive lithography process combined with etching as described above or by negative lithography combined with a lift-off process. The latter was used in the beginning, but the former is favoured now since a better resolution is achieved and the pre-structured photoresist is excluded as a source of contamination during the cleaning process.

The sputter clean step before depositing the second aluminum layer turned out to be one of the major obstacles in fabricating a good Josephson junction. Since it is crucial that the interface between electrode and dielectric of the Josephson junction is free from other substances such as copper, semiconducting materials or polymers, a substantial cleaning rate as well as a minimum of material redeposition during the cleaning process needs to be guaranteed.

Several micrographs of the fabricated Josephson junctions are shown in figure 16.

3 Experimental setup

Transport characterization of the prepared Josephson junctions is carried out using a dc-setup to measure current-voltage characteristics (I-V characteristics). This is done at room temperature with the probe station as well as at cryogenic temperatures using a ^{3}He refrigerator. The dc-setup is described in section 3.1.1, section 3.1.2 gives an overview of the functional principle of the utilized ^{3}He refrigerator.

Qubit measurements are performed in a dilution refrigerator whereby base temperatures of about 20 mK are reached. Its operation principle is briefly explained in section 3.2.1. Section 3.2.2 describes the microwave setup and experimental wiring and an overview of mounted samples in the cryostat is given in section 3.2.3.

3.1 Josephson junction transport characterization

3.1.1 Dc-setup

Figure 23 shows a schematic of the employed dc-setup for Josephson junction transport characterization. To obtain an I-V characteristic, the current through the Josephson junction is swept by combining a voltage generator (G) and a current source (CS). The amplified (Amp) voltage across the Josephson junction as well as the voltage corresponding to the driving current are plotted with an oscilloscope in xy-mode. This data is recorded with a computer using GoldExI [Gol97].

The setup corresponds to a four-point measurement with respect to cable resistances connected to the sample. Under room temperature conditions, the lead resistance in the structured sample is added to the measured total resistance as a series resistance. If the sample is cooled so that the aluminum film gets superconducting, the lead resistance vanishes and one ends up with an ideal four-point measurement of the tunnel junction.

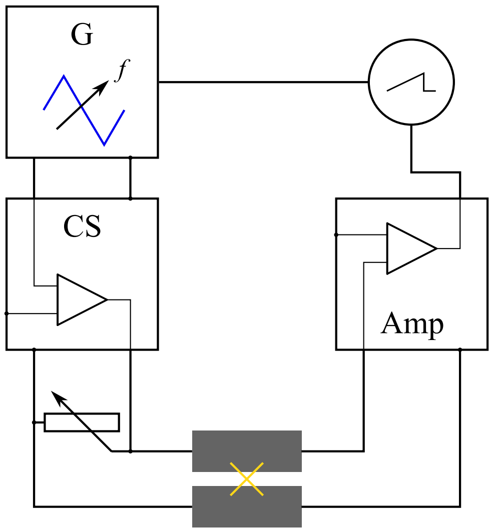

Figure 23: Schematic circuit diagram of the dc-setup employed for Josephson junction transport characterization. A voltage generator (G) generates a triangular voltage which is transformed to a current (CS). The amplified (Amp) voltage across the Josephson junction is plotted against the current sweep on an oscilloscope. A variable shunt resistor connecting the output lines of the current source is depicted.

To contact the tunnel junction pads at room temperature, the probe station is used, providing a fast and easy way to measure the critical current I_c and observe the typical non-ohmic behaviour of the I-V characteristic.

At cryogenic temperatures, the measurement electronics shown in figure 23 is connected to dc-lines of the employed dipstick, which are in turn wire bonded to the sample. To reduce noise in the measurement signal, all dc-lines in the dipstick are low-pass filtered by means of a simple RC network with a cut-off frequency of about 15 kHz.

3.1.2 ^{3}He refrigerator

To observe the effect of Josephson tunnelling, the investigated sample needs to be cooled below its critical temperature for superconductivity. For bulk aluminum, this is achieved with temperatures below 1 K.

Figure 24 shows the dipstick of a typical ^{3}He refrigerator used in this work for transport measurements of the prepared Josephson junctions.

The sample to be cooled is mounted close to the ^{3}He pot to guarantee good thermal contact. A cryoperm shield is attached to protect the sample against electromagnetic and thermal radiation. In addition, the dipstick is hosted in an internal vacuum chamber (IVC) which is framed by a copper cylinder. The dipstick is mounted in a bath of liquid helium.

While cooling down the cryostat, the sorption pump stage is kept at about 45 K by heating while the 1K pot is pumped to reduce the vapour pressure of the ^{4}He

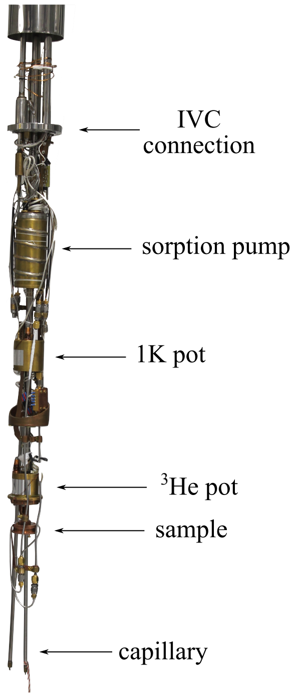

Figure 24: Typical dipstick of a ^{3}He refrigerator. One can see the different temperature stages. When the cryostat is at base temperature, the sorption pump stage has a temperature of about 3 K and the 1K pot roughly 1 K. ^{3}He condenses in the ^{3}He pot and its vapour pressure is reduced by pumping down to about 0.26 K. Pumping is performed with the capillary at the end of the dipstick which is immersed into liquid ^{4}He. All stages are located inside the internal vacuum chamber (IVC). In order to perform dc-measurements, the dipstick is equipped with several filtered dc-lines.

inside. By that, the boiling temperature of ^{4}He drops from 4.2 K to about 1.7 K. At these temperatures, all the ^{3}He inside a closed system of the cryostat condenses into the ^{3}He pot.

In a subsequent step, the heating of the sorption pump is switched off which leads to a cooling to about 3 K. By pumping at the ^{3}He pot, its vapour pressure is reduced, leading to a decrease in boiling temperature down to the base temperature of the cryostat of about 0.26 K.

3.2 Qubit measurements

3.2.1 Dilution refrigerator

Qubit measurements are usually carried out at temperatures less than 30 mK. Since the smallest relevant frequencies of about 3 GHz correspond to about 140 mK, this guarantees the suppression of dissipation due to thermal quasi-particles.

Such low temperatures are reached with a dilution refrigerator. In the present work, a wet dilution refrigerator from High Precision Devices (HPD) is used.

Its operation principle is based on the phase separation of a ^{4}He - ^{3}He isotope mixture when cooling below 0.5 K by pumping [Ens00]. The extractable cooling power originates from the dilution of ^{3}He atoms from the ^{3}He rich phase into the dilute phase, consisting of superfluid ^{4}He and ^{3}He behaving as a Fermi liquid. This process takes place in the so called mixing chamber. To sustain a cyclic cooling

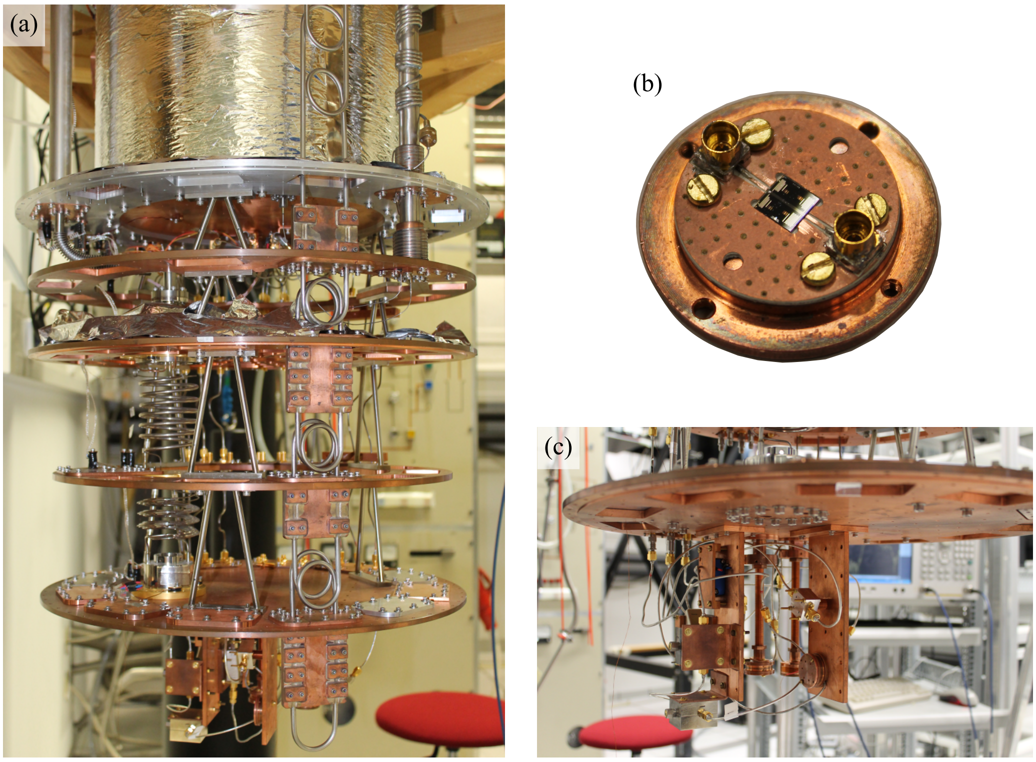

Figure 25: (a) Dilution refrigerator used in the present work for qubit measurements. The various temperature stages are visible. (b) Mounted and wire bonded tunable transmon sample on the sampleholder. (c) Enlarged view of the base plate of the cryostat. All sample boxes including the microwave switch and circulators are visible.

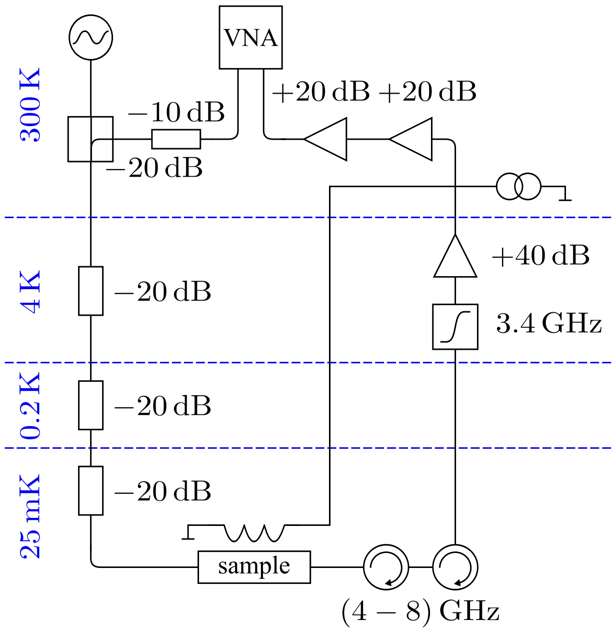

Figure 26: Schematic diagram of the microwave setup and experimental wiring used for qubit spectroscopy.

process, the mixing chamber is continuously supplied with ^{3}He, while helium from the dilute phase is extracted and purified to ^{3}He in the still.

Figure 25(a) shows the inside of the employed dilution refrigerator.

3.2.2 Microwave setup for spectroscopy and experimental wiring

A schematic diagram of the employed microwave setup including the experimental wiring in the cryostat and at room temperature is given in figure 26.

The manipulation tone from a microwave generator and the probe tone from the vector network analyzer (VNA) are combined by means of a directional coupler. The VNA is connected with the −20 dB coupled port and the microwave line going into the cryostat is connected to the input port of the directional coupler.

In the cryostat, the microwave signal is attenuated at various temperature stages to thermalize the inner conductor before it reaches the feedline of the sample. Together with the measured cable attenuation in the line going to the sample of about −10 dB and an additional attenuation of the VNA signal before entering the directional coupler, the net attenuation of the probe tone corresponds to −100 dB.

The outgoing signal passes two cryogenic circulators with their third port shunted to 50 Ω, respectively, to avoid backscattering of thermal noise from above temperature stages, in particular noise produced by the amplifier. At the 4K stage, the signal is high-pass filtered and amplified with a Low Noise Factory high electron mobility transistor (HEMT).

Before entering the second port of the VNA, the signal is amplified in two stages at room temperature.

To enable flux tuning of the transmon, a superconducting coil with 500 windings is attached around its sample box. The coil is controlled with a galvanically decoupled electronics.

3.2.3 Sample mounting

Figure 25(c) shows the base plate of the dilution refrigerator with all samples mounted.

A sample comprising tunable transmon qubits is mounted on the sample holder shown in figure 25(b), which is compatible with the flux coil sample box. The microwave setup depicted in figure 26 corresponds to the measurement line of this sample. A cryoperm cylinder which is attached around the sample box ensures magnetic shielding.

A non-tunable transmon sample with a single Josephson junction connecting the capacitor pads is mounted in a aluminum sample box, also depicted in figure 25(c). Since the aluminum box is superconducting at base temperature, proper magnetic shielding is guaranteed. In this measurement line, only one circulator is installed.

To enable easy qubit detection and fast measurements due to a better signal to noise ratio, the mounted transmon samples feature strongly coupled readout resonators to the feedline and a stronger qubit to resonator coupling. The designed and simulated parameters of the mounted samples are a coupling quality factor of $Q_C = 1000$ and a loaded qubit quality factor of $Q_{L,q} = 3000$. The increased resonator-qubit coupling does not lead to a Purcell induced limitation of the transmon´s relaxation time.

A third measurement line is equipped with a sample featuring four weakly coupled microstrip resonators. Those allow to measure the internal quality factor of the resonators and therefore the quality of the patterned aluminum films.

4 Experimental results

This section summarizes the experimental results obtained in the present work.

Section 4.1 gives the results of atomic force microscopy (AFM) measurements, carried out to investigate the surface roughness of patterned aluminum films. Tunnel junction characterization at room temperature and Josephson junction transport measurements are presented in section 4.2. Structured microstrip resonators are investigated in section 4.3 and section 4.4 gives the obtained results in spectroscopic qubit measurements.

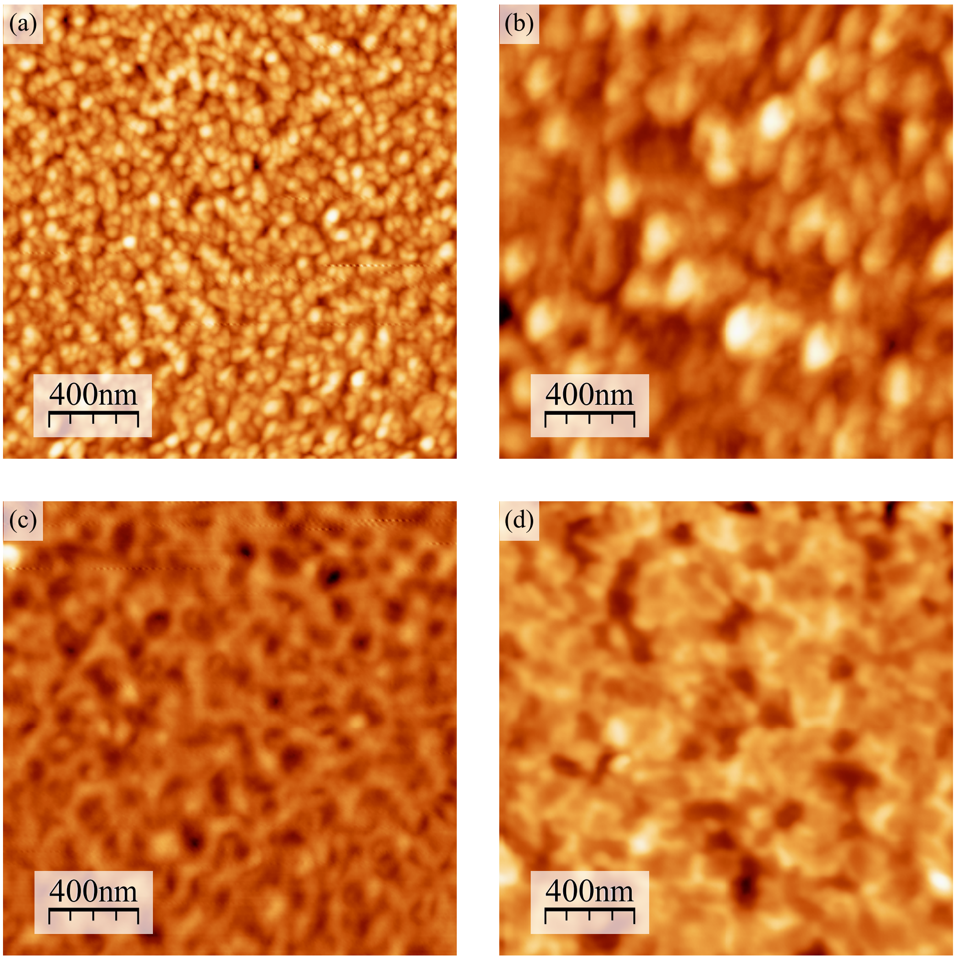

Figure 27: Atomic force microscopy pictures of prepared aluminum films on intrinsic silicon. (a) Sputter deposited aluminum film with a thickness of 70 nm, $\Delta z = 16\,\text{nm}$, $R_{RMS} = 2.0\,\text{nm}$. (b) Sputter deposited aluminum film with a thickness of 120 nm, $\Delta z = 15\,\text{nm}$, $R_{RMS} = 2.4\,\text{nm}$. (c) Film surface after a typical argon clean step without thoroughly evacuating the chamber before, $\Delta z = 14\,\text{nm}$, $R_{RMS} = 1.2\,\text{nm}$. (d) Film surface after a typical argon clean step (22 min effective) with evacuating the chamber to $5 \cdot 10^{-7}$ mbar, $\Delta z = 33\,\text{nm}$, $R_{RMS} = 3.8\,\text{nm}$. [Hor07]

4.1 AFM data of the patterned aluminum films

The properties of the deposited aluminum films in terms of crystal structure, surface roughness and homogeneity are decisive for the behaviour of the patterned Josephson junction and the corresponding qubit, as well as the internal quality factor of the resonators.

Aluminum films which are sputtered under the conditions presented in section 2.1 are polycrystalline. To obtain a good quality qubit, metal films need to be very clean and homogeneous. This is achieved by sputter depositing aluminum with a comparably high power for only a short time in the range of several minutes, to avoid a heating of the substrate which would increase the atom mobility and lead to larger inhomogeneity. By that, the surface of the aluminum film becomes as smooth as possible which is important to avoid the formation of pinholes in the tunnel barriers of the fabricated Josephson junctions.

Figure 27 shows atomic force microscopy (AFM) pictures of prepared aluminum films. Comparing figures 27(a) and 27(b) shows the modification of the granularity as well as the film roughness with increasing thickness.

In figure 27(d), the film of figure 27(b) is cleaned as done for qubit fabrication. The RMS roughness increases by about 1.5 nm, which is mainly due to a large scale roughening rather than single peaks emerging. This local smoothness prevents pinholes to occur which may short the Josephson junction.

It is important to note, that the cleaning process is highly dependent on the background pressure conditions in the loadlock. Figure 27(c) shows the surface of a cleaned aluminum film without evacuating the loadlock to about $5 \cdot 10^{-7}$ mbar. The roughness is strongly decreased. Measuring the aluminum erosion during such a cleaning step however reveals, that the cleaning is highly inefficient. Both observations can be explained by water and oxygen remnants in the chamber leading to a constant reoxidation and a saturation of the plasma ions.

4.2 Tunnel junction characterization

In the course of building the tunnel junction in this work, several major challenges needed to be overcome.

Preparing the first samples, the attention was focused on the roughness of the patterned aluminum films. While optimizing deposition parameters, experiments with a small oxygen admixture during film growth to decrease the surface roughness were carried out. Since it did not introduce crucial advantages and oxygen implantation modifies the superconducting parameters of the aluminum film, this approach was dropped.

After fabricating the first tunnel junctions it became evident, that the native oxide is not removed entirely during the cleaning step just before oxidation. After realizing the malfunction of the sputter deposition tool and fixing it as described in section 2.1, results improved quickly.

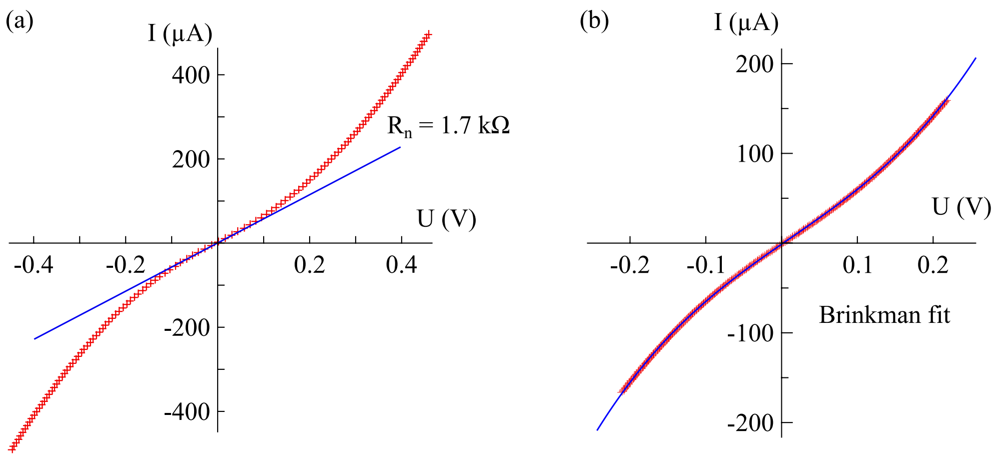

Figure 28: Room temperature transport characteristics of the prepared tunnel junctions. (a) I-V characteristic of a tunnel junction of resistance $R_n = 1.7\,\mathrm{k}\Omega$ (blue) and a junction area of $1.5\,\mu\mathrm{m}^2$. The corresponding critical current density is $j_c = 10.4\,\frac{\mathrm{A}}{\mathrm{cm}^2}$. The non-ohmic behaviour is clearly visible. (b) Enlarged view of (a) for the range $|U| \lesssim 0.2\,\mathrm{V}$, where Brinkman´s model (blue curve) for the tunnelling conductance applies. Extracted values from the model are a barrier thickness $d = 2.6\,\mathrm{nm}$ and a mean potential barrier height $\bar{\Phi} = 1.1\,\mathrm{eV}$.

Further adapting parameters regarding film thickness and oxidation exposure finally led to the results presented in sections 4.2.1 and 4.2.2.

4.2.1 Room temperature characteristics

Figure 28(a) shows the room temperature I-V characteristic of a prepared tunnel junction. From the linear regime at $|U| \lesssim 0.05\,\mathrm{V}$, the resistance $R_n = 1.7\,\mathrm{k}\Omega$ can be extracted. The junction area is $1.5\,\mu\mathrm{m}^2$, corresponding to a critical current density of $j_c = 10.4\,\frac{\mathrm{A}}{\mathrm{cm}^2}$. A deviation of the I-V characteristic from the linear ohmic branch due to tunnelling effects described in section II.1.5 is clearly visible.

According to Brinkman´s model for electron tunnelling through a thin barrier, the barrier thickness of the tunnel junction is $d = 2.6\,\mathrm{nm}$ and the mean potential barrier height is $\bar{\Phi} = 1.1\,\mathrm{eV}$, taking into account data points with $|U| \lesssim 0.2\,\mathrm{V}$. In addition, the model suggests a barrier asymmetry of $\Delta\Phi = 0.19\,\mathrm{eV}$, showing a small difference in interface quality of the tunnel junction.

The value of the mean barrier height $\bar{\Phi}$ is close to the maximum voltages applied in the experiment, which explains the considerable deviation of the I-V characteristic from the ohmic branch. The fitted curve is shown in blue in figure 28(b).

In figure 29(a), the resistance-area product R_nA is plotted against the junction area A. Since $R_nA \approx$ const., scaling of the tunnel junctions with their size is validated. This property is directly related to the quality and purity of the tunnel barriers and their interfaces.

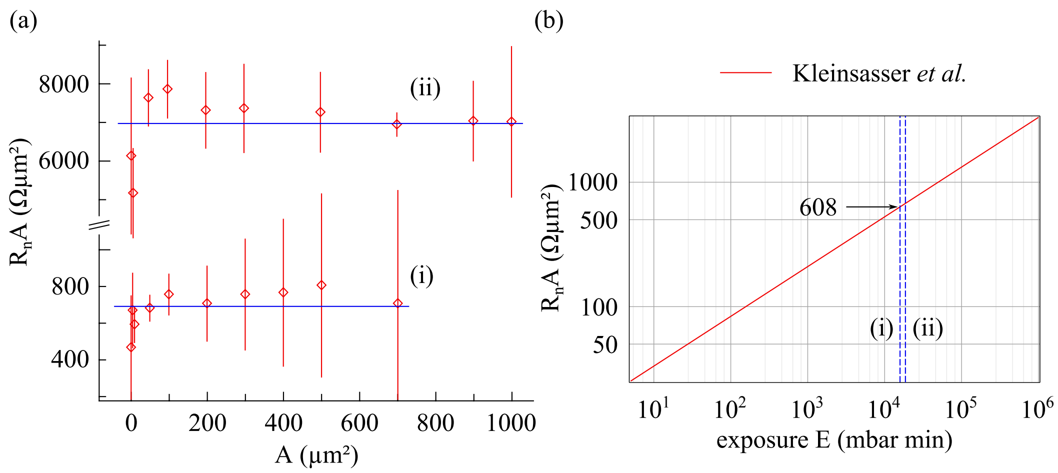

Figure 29: (a) Validation of the scaling of the sheet resistance R_n with junction area A for samples with different oxygen exposure (i), (ii). The mean value of R_nA is shown in blue for both samples. (b) R_nA with respect to oxygen exposure. The red line shows the expectation from Kleinsasser *et al.* [Kle95]. Blue lines correspond to exposure parameters chosen to prepare samples (i), (ii).

A resistance of 2.5 Ω is subtracted from the measured R_n to account for the lead resistance of the sample given rise by the effective two-point measurement technique. Error bars occur due to uncertainties in measuring R_n as well as determining A.

The mean values of R_nA for the samples prepared with different oxygen exposure are depicted in blue.

Figure 29(b) shows the Kleinsasser expectation (red) of R_nA with respect to oxygen exposure E, following a power dependence

$$R_nA \propto E^{0.4}. \tag{137}$$

While the measured R_nA of sample (i) deviates from the expectation only by about 10%, a larger discrepancy of roughly one order of magnitude occurs for sample (ii). This is most likely due to a heating of the sample during the cleaning process to about 60 °C, leading to higher oxygen mobility and therefore an enhanced oxidation process.

Since values higher than expected from figure 29(b) were observed in more samples with similar oxygen exposure, it is evident that R_nA of the prepared Josephson junctions does not strictly follow the dependence given in equation (137) in the present exposure regime.

The breakdown voltage of the prepared tunnel junctions is in the range (0.6 − 0.8) V, depending on the thickness of the tunnel barrier. These values are characteristic for aluminum tunnel junctions [Sch11] and therefore give strong evidence for electron tunnelling.

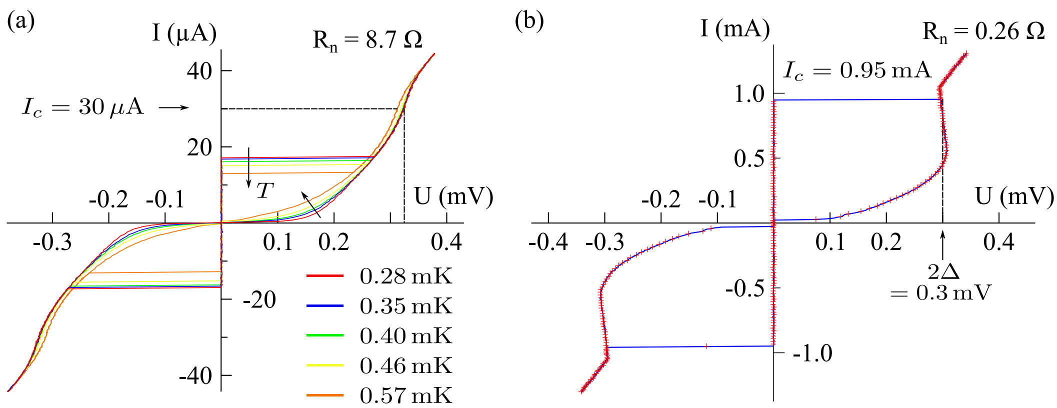

Figure 30: I-V characteristics of prepared Josephson junctions measured at cryogenic temperatures. (a) A 2Δ-kink is visible but smeared out. I_c is suppressed and strongly scales with measurement temperature. The strong smearing of the voltage branch indicates subgap states in the electrodes. (b) Characteristic of a recent Josephson junction. The 2Δ-kink is very sharp and the characteristic heating effect at 2Δ is visible.

4.2.2 Josephson junction transport characterization

Figure 30 shows I-V characteristics of prepared Josephson junctions measured at cryogenic temperatures.

The characteristic of the sample given in figure 30(a) shows a smeared kink around 2Δ, corresponding to ohmic tunnelling of quasi-particles. The measured critical current I_c is suppressed with respect to the value corresponding to the given R_n, depicted by the horizontal dashed line. The strong smearing of the voltage branch indicates subgap states in the electrodes which might be due to defects in the interfaces. The pronounced rounding of the voltage branch together with the depicted scaling of its shape and I_c with measurement temperature can be explained by a large quasi-particle abundance caused by poor superconducting properties of one or both electrodes. This claim is supported by the fact, that a critical current can be observed only up to 0.9 K and superconductivity of the electrodes up to 1.0 K.

It is important to recognize though, that the subgap current of the Josephson junction is less than 1% of the measured I_c for $|U| < 0.08\,\mathrm{mV}$, which is the relevant region of the Josephson junction when operated as a qubit.

The characteristic of the latest fabricated Josephson junction is depicted in figure 30(b). The measured I_c and R_n match the calculation by Ambegaokar and Baratoff given in equation (110) to a high degree.

The 2Δ-kink is very sharp and pronounced and the strong temperature dependence of I_c is not observed, indicating proper superconducting behaviour of the electrodes. Superconductivity as well as a critical current can be measured until 1.13 K, which is close to the literature value of 1.18 K [Nor06] for the critical temperature of bulk aluminum.

In the voltage branch where $|U| \approx 2\Delta$, a characteristic heating effect is observed,

Table 2: Overview of the measured high power quality factors Q_i, Q_L of the different microstrip resonator designs.

Q_C (10^3)	50	5	1
Q_i (10^3)	14.7 ± 0.6	24.9 ± 0.9	24 ± 6
Q_L (10^3)	8.96 ± 0.22	3.648 ± 0.021	0.669 ± 0.007

which appears as an increase in voltage with decreasing current. The reason for this effect is thermal activation of quasi-particles, leading to an enhanced tunnelling probability.

The smearing of the voltage branch between Δ and 2Δ is most likely caused by defects in the interfaces. Since the effect is increased by thermal quasi-particles, an improved performance of the Josephson junction operating as a qubit at base temperature of the dilution refrigerator can be expected.

The measured subgap current is roughly 2.5% of I_c in the region where $|U| < 0.1\,\mathrm{mV}$, indicating the desired strong underdamping of the Josephson junction.

4.3 Resonator measurements

In this section, characteristic parameters of the prepared microstrip resonators are investigated. Measurements are carried out with the samples mounted in the dilution refrigerator.

Measurements with the sample comprising the weakly coupled microstrip resonators, presented in section 4.3.1, allow to extract information about the internal quality factor Q_i of the resonators and aluminum film quality. In section 4.3.2, a resonator on the transmon sample is analysed to obtain primarily the coupling quality factor Q_C, which defines the proper measurement regime for qubit measurements.

All power specifications given in the present section are to be understood as VNA settings. An additional attenuation of $-30\,\mathrm{dB}$ is installed in the measurement line entering the cryostat. Microwave wiring inside the cryostat leading to the sample is identical for all lines.

4.3.1 Weakly coupled microstrip resonators

To extract several characteristic parameters of a transmission line resonator, usually a circle fitting method in the complex Gauß plain is applied. The fitting model used in the present work is based on the analysis given by [Gao08, Kha12], the fitting algorithm is provided by [Pro13].

Since the internal quality factor Q_i, that can be extracted from such a model is limited by the coupling quality factor Q_C to a certain extend, an exact value for Q_i is obtained only for weak coupling, where $Q_C \approx Q_i$.

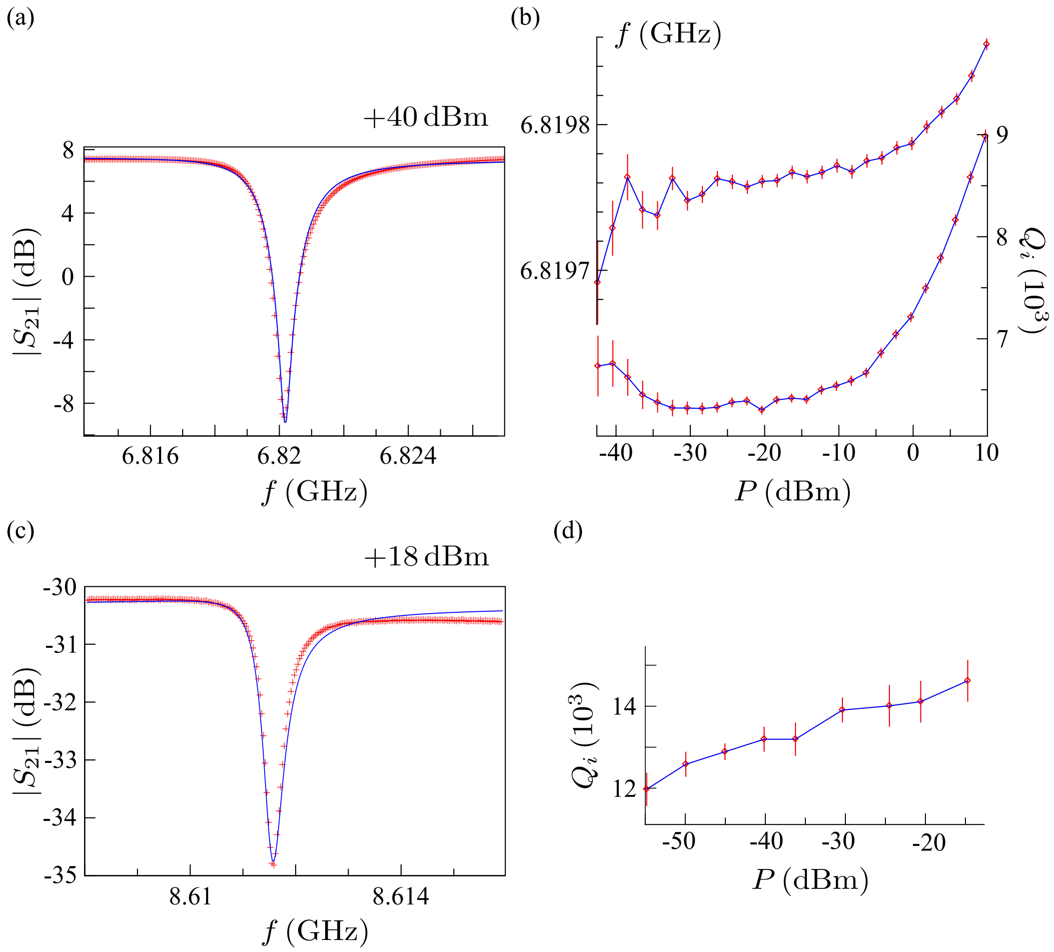

Figure 31: (a) High power transmission amplitude $|S_{21}|$ (red) of a microstrip resonator with a designed coupling $Q_C = 5 \cdot 10^3$. The fitted amplitude deduced from a circle fit is shown in blue. The extractable resonator characteristics are $Q_i = (24.9 \pm 0.9) \cdot 10^3$ and $Q_L = 3648 \pm 21$. (b) Power dependence of the resonator frequency f and the internal quality factor Q_i. Error bars are indicating fitting errors. (c) Transmission amplitude (red) with fitted curve (blue) of a weakly coupled microstrip resonator with a designed $Q_C \approx 50 \cdot 10^3$. Extracted resonator parameters are $Q_i = (14.7 \pm 0.6) \cdot 10^3$ and $Q_L = (8.96 \pm 0.22) \cdot 10^3$. (d) Power dependence of Q_i of the weakly coupled resonator.

Figures 31(a), (c) show measured high power transmission amplitude data of microstrip resonators with a designed coupling $Q_C = 5 \cdot 10^3$ (a) and $Q_C \approx 50 \cdot 10^3$ (c).

Table 2 summarizes the extracted parameters from the associated circle fit. The measured Q_i for the two stronger coupled resonators are well in accordance while a lower value is found for the weakly coupled resonator. This might mainly be due to a higher measurement temperature giving rise to a larger abundance of thermally excited quasi-particles. Measurements at the weakly coupled resonator were carried out at higher temperatures as the cryostat was already warming, caused by a blocking probably in the 1K-pot capillary.

Measured values of Q_L are well in accord with the designed coupling. It is interesting to note that Q_L of the weakly coupled resonator is limited by its internal quality factor in the measurement.

Respective power dependences of the resonance frequency and the internal quality factor are given in figures 31(b), (c). A flattening of Q_i is particularly visible in figure 31(b) at about $-20\,\mathrm{dBm}$. According to the estimation given in section 4.4, this roughly corresponds to the single photon regime, where $Q_{i,s} \approx 6 \cdot 10^3$. This single photon internal quality factor $Q_{i,s}$ is lower than expected. A main reason might be the extensive cleaning procedure, degrading the surface quality of the aluminum film. This could be avoided by including the patterning of the microstrip resonators in the second lithography step. Another possible explanation is an imperfect etching process, inducing edge spikes caused by redeposition. This can be ascribed to the ballistic argon etching process and a possible advancement is to employ pure chemical etching.

4.3.2 Qubit readout resonators

Figure 32(a) shows an overview of the readout resonators on the transmon sample. The smallest resonator with a frequency of about 9 GHz is not visible in the given transmission amplitude spectrum as it exceeds the VNA´s measurement range. Comparing the resonance frequencies with the design values given in table 1 reveals a systematic shift of about 150 MHz towards lower frequencies. This can be explained by uncertainties in the geometric size of sample features and a sample environment that does not exactly correspond to the conditions assumed in the simulation. A small kinetic contribution to the resonators´ inductances is also possible.

A detailed transmission amplitude spectrum of the 5.83 GHz resonator, mainly used for qubit measurements, is given in figure 32(b). Fitting data is summarized in table 2.

4.4 Qubit spectroscopy

To observe the dressed eigenstates of the resonator qubit system given in equation (75) and the dispersive shift occurring in the effective Jaynes-Cummings Hamilto-

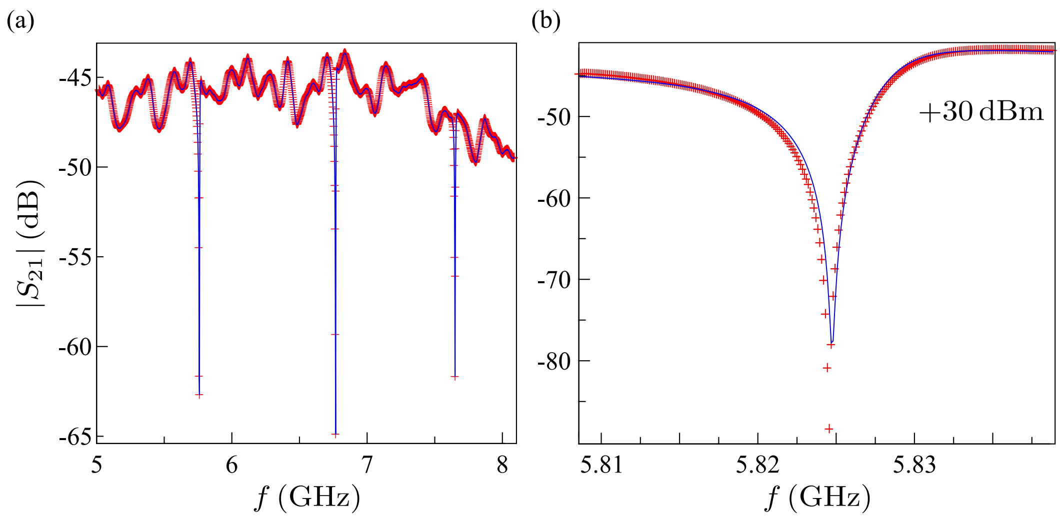

Figure 32: (a) Transmission amplitude $|S_{21}|$ giving an overview of the transmon readout resonators located at 5.83 GHz, 6.81 GHz and 7.67 GHz. (b) Transmission amplitude (red) with respective fit (blue) of the 5.83 GHz readout resonator. The applied microwave power is $P = +30\,\text{dBm}$. Extracted resonator characteristics are $Q_i = (24 \pm 6) \cdot 10^3$ and $Q_L = 669 \pm 7$.

nian, equation (78), measurements need to be performed in the single photon regime. This corresponds to an average occupation of the readout resonator with only a single photon, which can be achieved by strongly decreasing the probe tone power.

With a hardware attenuation of the probe signal of $-100\,\text{dB}$, as specified in figure 26, the microwave power P_{fl} at the feedline of the sample can be calculated to be

$$P_{fl} = 1 \cdot 10^{-13}\,\text{mW}, \tag{138}$$

assuming an applied probe tone power of $-30\,\text{dBm}$ and noting that $0\,\text{dBm} = 1\,\text{mW}$.

With the resonator quality factors extracted from the resonator fitting in section 4.3 and a resonator frequency of 6 GHz, the microwave power P_{res} in the resonator can be calculated with the approximate formula [Bar09]

$$P_{res} = \frac{2Q_L^2}{\pi Q_C} \cdot P_{fl}. \tag{139}$$

The average number $\langle n \rangle$ of photons in the resonator becomes

$$\langle n \rangle \approx 1.7, \tag{140}$$

clearly complying the single photon condition.

All power values given in this section are set values on the respective device without taking into account additional hardware attenuation.

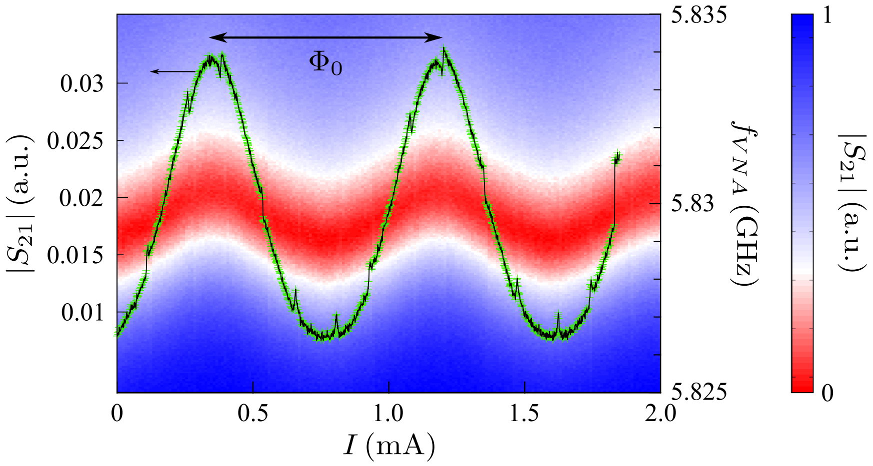

Figure 33: Shift in resonance frequency of the 5.83 GHz readout resonator dependent on the applied magnetic flux corresponding to a bias current I. Colours represent the transmission amplitude $|S_{21}|$. The observed periodicity is in close agreement with the calculated value for one flux quantum Φ_0, given in equation (141). A detailed scan of the shift is shown in green. Several features are visible.

4.4.1 Flux bias sweep

Sweeping the current of the flux coil gives rise to a change of the transmon´s resonance frequency due to the control of the effective critical current of the split Josephson junction. If the transmon frequency matches the frequency of its readout resonator, the detuning Δ vanishes and an avoided level crossing can be observed.

Figure 33 shows the transmission amplitude $|S_{21}|$ of the 5.83 GHz readout resonator dependent on the applied magnetic flux.

According to the specification of the utilized flux coil, an applied current of 1 mA corresponds to a magnetic induction of $2.15 \cdot 10^{-5}$ T at the position where the sample is located. With a designed inner area of the split Josephson junction of $120\,\mu\mathrm{m}^2$, one can calculate the coil current corresponding to one flux quantum Φ_0 to be

$$\Phi_0 \mathrel{\widehat{=}} 0.8\,\mathrm{mA}. \tag{141}$$

This value corresponds to the periodicity observed in the experiment of figure 33.

Since no clear avoided level crossing is visible, the transmon frequency never matches with the one of the readout resonator but rather comes in close proximity, giving rise to a repelling of the resonator´s resonance.

A detailed scan of the shift in the resonator´s frequency is depicted in green. The measured transmission amplitude $|S_{21}|$ corresponds to a frequency point close to the resonator´s dip minimum.

Several periodically occurring features are visible which may be ascribed to the coupling to a nearby quantum system. Since the periodicity is about 0.27 mA, this could be another qubit which is located close to the edge of the chip where

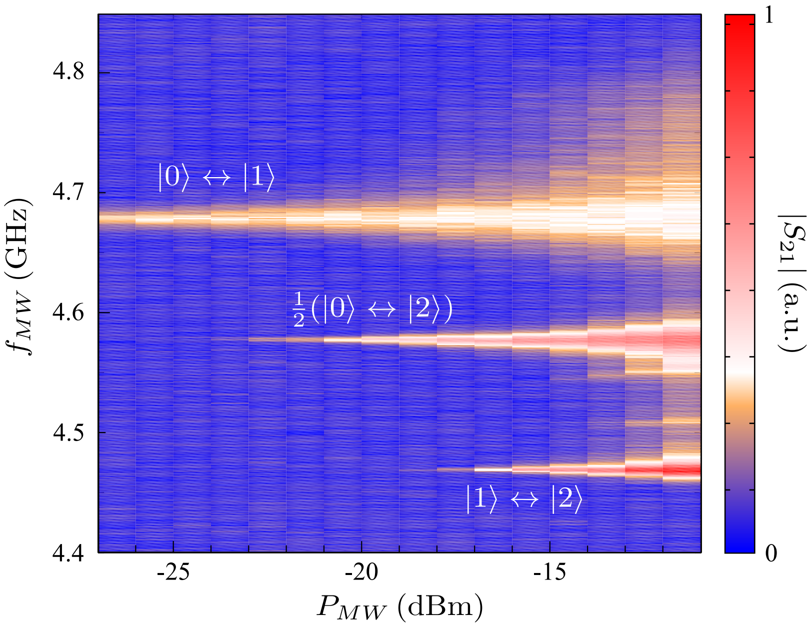

Figure 34: Dispersive shift of the transmission amplitude $|S_{21}|$ of the 5.83 GHz readout resonator dependent on the microwave driving frequency f_{MW} and its power P_{MW}. The VNA power is set to -30 dBm, corresponding to the single photon regime. With increasing microwave power, the distinct transmon transitions $|0\rangle \leftrightarrow |1\rangle$, $\frac{1}{2}(|0\rangle \leftrightarrow |2\rangle)$ and $|1\rangle \leftrightarrow |2\rangle$ appear successively, before higher order transitions are excited and become visible.

magnetic conditions are different. As the signatures do not occur at certain fixed frequencies, coupling to two-level systems (TLS) can be excluded, assuming that they do not respond to magnetic fields. Possible candidates roughly matching the observed frequencies are the $|0\rangle \leftrightarrow |2\rangle$ transition and similar higher order two-step transitions.

4.4.2 Driving the qubit in the dispersive regime

To observe a dispersive shift in resonance frequency dependent on the qubit state, and thereby locate the qubit frequency, a wide frequency range is scanned by sweeping the manipulation tone frequency and measuring the resonator response.

Biasing the transmon to its flux sweet spot at 0.35 mA, according to figure 33, a broad signature is observed at about 4.6 GHz. In the course of several measurements with different microwave driving powers P_{MW}, the existence of relatively strong flux noise is indicated. This can be explained by a malfunction of the utilized current source and the respective dc-wiring. Further possible error sources are a missing cryogenic filtering of the coil current or crosstalk between the current signal line and other dc-lines sharing the same cord when passing through the cryostat.

To resolve distinct transmon transitions which ultimately provides evidence for the existence of a quantum system, measurements are carried out at the non-tunable transmon sample mounted in the cryostat, which is not subject to flux noise.

Figure 34 shows the dispersive shift of the transmission amplitude $|S_{21}|$ of the 5.83 GHz readout resonator dependent on the microwave driving frequency f_{MW} and its power P_{MW}. The power of the probe tone coming from the VNA is set to -30 dBm, corresponding to the single photon regime.

For small driving powers, only the fundamental qubit transition $|0\rangle \leftrightarrow |1\rangle$ is excited by the manipulation tone. With increasing microwave power, two additional transitions occur at lower frequencies. Those correspond to half of the energy of the two-photon process $|0\rangle \leftrightarrow |2\rangle$ and the next order transmon transition $|1\rangle \leftrightarrow |2\rangle$, respectively. With further increasing microwave power, even more transitions are excited which partly overlap and could be addressed in a rigorous analysis.

Detailed vertical slices of figure 34 are given in figure 35. The absolute anharmonicity α of the transmon corresponds to the distance of the transitions $|0\rangle \leftrightarrow |1\rangle$ and $|1\rangle \leftrightarrow |2\rangle$. From figure 35,

$$\alpha = 210\,\mathrm{MHz} \tag{142}$$

can be extracted, matching the designed value from equation (134) within 7%.

The frequency position of the transitions measured in figures 34 and 35 are independent of the applied microwave power P_{MW}, which strongly supports the presented assignment of the transitions. Furthermore, the qualitative peak widths and heights are well in accord with the expectation that the two-photon process $|0\rangle \leftrightarrow |2\rangle$ shows a higher transition amplitude than the fundamental one-photon process $|0\rangle \leftrightarrow |1\rangle$ for larger driving powers and vice versa [Lis08].

As described in section II.2.1, small fluctuations in the energy level splitting of the qubit states give rise to dephasing due to fluctuations in the Larmor frequency. As a result, the observed peak width in figure 35 increases, which is called inhomogeneous broadening [Lis08]. This enables a rough estimate of the dephasing time T_2 of the transmon.

Since the measured full width σ, measured at half maximum of the dispersive excitation peak $|0\rangle \leftrightarrow |1\rangle$, shows a so called power broadening [Lis08] dependent on the manipulation tone power P_{MW}, the relevant quantity is the zero-power excitation peak width σ_0. It is obtained by measuring σ for different powers P_{MW} and extrapolating to vanishing power.

According to [Abr61], there is a linear dependence of the peak width σ and the applied microwave amplitude, which is proportional to $P_{MW}^{1/2}$. A linear regression of measured data points is given in figure 36(a). The extracted zero-power width $\sigma_0 = 2.4\,\mathrm{MHz}$ corresponds to a dephasing time

$$T_2 = \frac{1}{\pi\sigma_0} = 0.13\,\mu\mathrm{s}. \tag{143}$$

Assuming the relaxation time T_1 to be in the same region, this value is in good agreement with the estimation from simulated data given in equation (132).

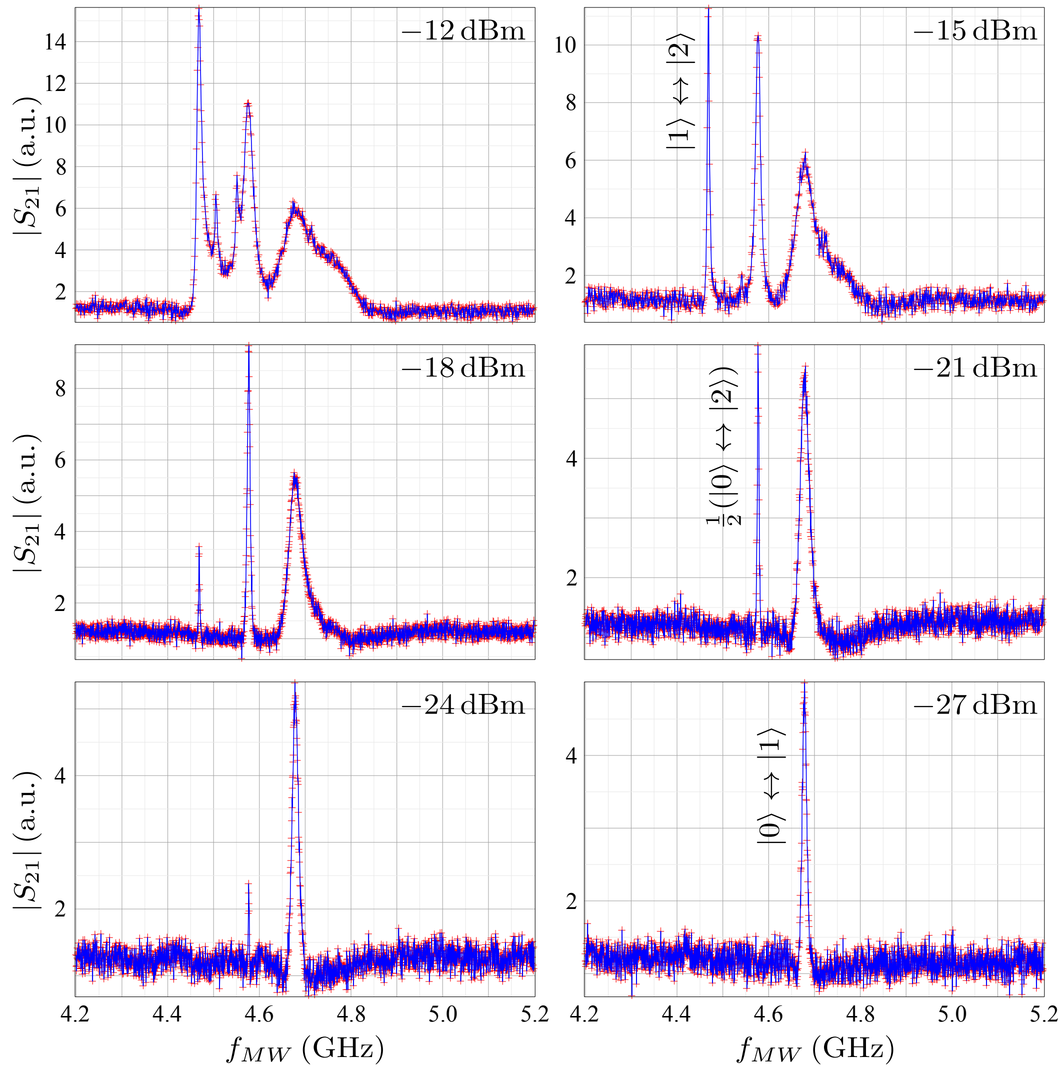

Figure 35: Dispersive shift of the transmission amplitude $|S_{21}|$ of the 5.83 GHz readout resonator dependent on the microwave driving frequency f_{MW} and its power P_{MW}. Small pictures are showing detailed slices of the colour plot given in figure 34.

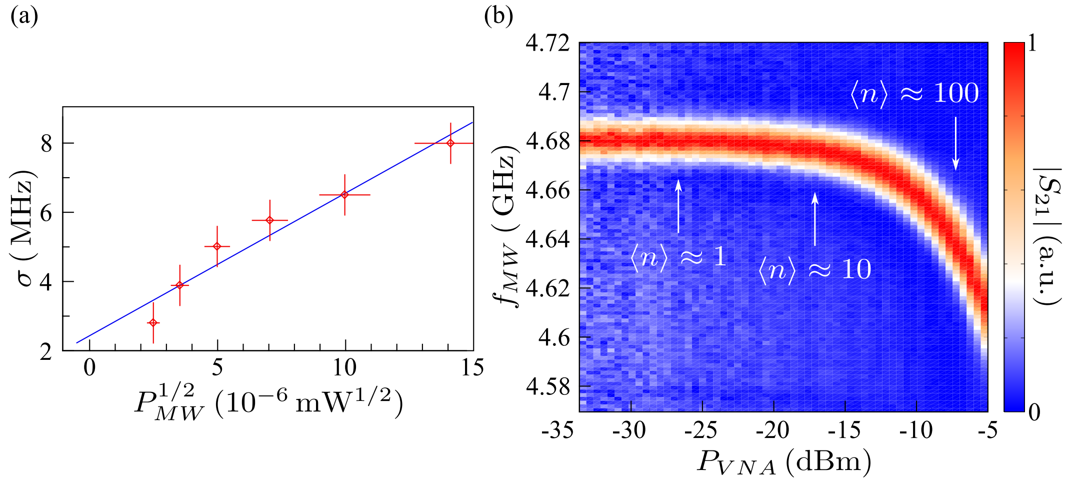

Figure 36: (a) Full width σ, measured at half maximum of the dispersive excitation peak dependent on the amplitude $P_{MW}^{1/2}$ of the driving microwave pulse. Data points correspond to microwave pulse powers in the range -42 dBm to -27 dBm. Vertical error bars occur due to an uncertainty in determining the line width σ. A linear regression allows extrapolation of the line width to vanishing driving amplitude, which yields $\sigma_0 = 2.4$ MHz. This corresponds to an approximate dephasing time of $T_2 = 0.13\,\mu$s. (b) Ac-Stark shift of the transmon $|0\rangle \leftrightarrow |1\rangle$ transition dependent on the probe tone power P_{VNA}, corresponding to the average number of photons $\langle n \rangle$ in the resonator. An ac-Stark shift of 80 MHz is observed in the scanned region. The manipulation tone power P_{MW} is set to -27 dBm and the 5.83 GHz resonator is investigated. The coloured transmission amplitude $|S_{21}|$ is normalized for each vertical line to obtain maximum resolution.

4.4.3 Ac-Stark shift

As shown in equation (80) in section II.3.1.2, the ac-Stark shift depends on the number of photons $\langle n \rangle$ in the readout resonator. It can be observed by sweeping the probe tone power applied by the VNA, which is proportional to $\langle n \rangle$, and measuring the shift in the excitation frequency of the $|0\rangle \leftrightarrow |1\rangle$ transition. Measured data is shown in figure 36(b).

Since the transmon frequency is below the resonator frequency, the detuning Δ is negative and therefore the ac-Stark shift, proportional to χ, is also negative as χ and Δ always have the same sign. This is in agreement with an observed ac-Stark shift towards smaller frequencies.

The influence of the qubit on the photon number in the resonator is neglected. This is a good approximation for a large detuning between qubit and resonator, as is the case in the present measurement.

While the shift is proportional to the coupling g between qubit and resonator, the observed ac-Stark shift of 80 MHz is in the range with the one measured in [Sch05, Sch07].

4.4.4 Qubit spectrum: 2d spectroscopy

While distinct transmon transitions cannot be resolved with the tunable transmon sample in the present setup due to flux noise, a broad excitation peak is visible for a large microwave driving power of -3 dBm.

Figure 37 shows the transmon spectrum where bias current I and microwave driving frequency f_{MW} are swept. The colour bar corresponds to the dispersive shift of the transmission amplitude of the readout resonator. The oscillation period matches the periodicity observed in figure 33. Herewith the tunability of the transmon due to its split Josephson junction is demonstrated.

The signal-to-noise ratio is worse close to half-integer multiples of the flux quantum Φ_0 as the transmon frequency there gets small and a thermal noise contribution becomes noticeable.

From a fit to equation (122), shown in figure 37 by the black curve, the effective critical current of the split Josephson junction can be estimated to be $I_{c,\Sigma} = 40.7$ nA, which is roughly by a factor of three smaller than designed. This deviation is ascribed to the strong sensitivity of I_c to oxygen exposure and Josephson junction area, both being parameters which are hard to exactly control during fabrication.

According to the fit, the asymmetry parameter d of the split Josephson junction indicates a difference in critical current of $\Delta I_c = 8.1$ nA. This corresponds to a relative asymmetry of about 20%, most likely owed to a spread in Josephson junction size.

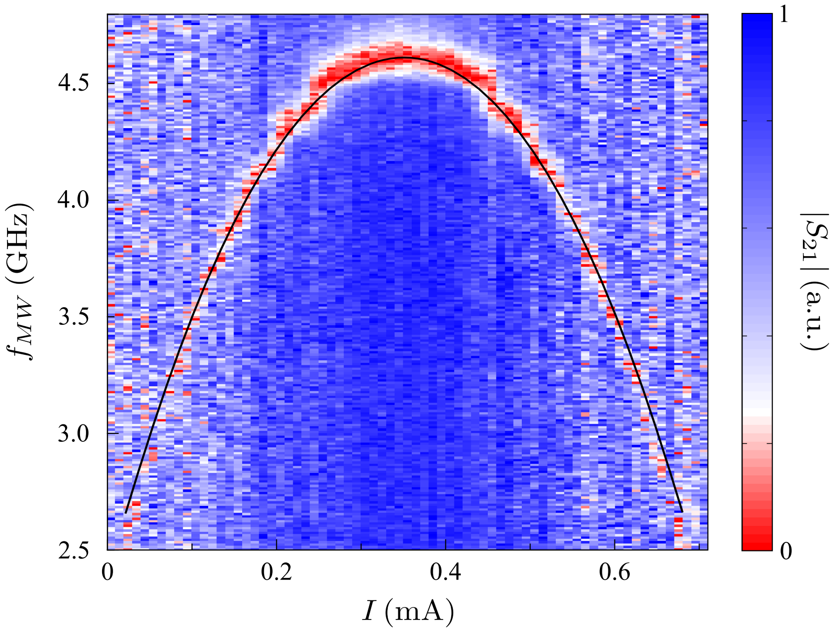

Figure 37: Transmon spectrum. Sweeping the bias current I and the microwave driving frequency f_{MW} reveals the tunability of the transmon frequency. The period of the oscillation equals the one observed in figure 33. The VNA power is $-30\,\mathrm{dBm}$ and the manipulation tone power is $-3\,\mathrm{dBm}$. Transmission amplitude is normalized for each column. The black curve shows a fit of measured data to equation (122). Extracted fit parameters are $I_{c,\Sigma} = 40.7\,\mathrm{nA}$ and $\Delta I_c = 8.1\,\mathrm{nA}$.

Chapter IV Summary and outlook

The aim of the present work was the development of a frequency tunable transmon qubit in microstrip geometry.

The transmon architecture promises a large dephasing time of the qubit due to its strongly reduced sensitivity to charge noise. This is achieved by employing the architecture of a conventional single Cooper pair box and inserting a large shunt capacitance in parallel to the Josephson junction. Due to an increase of the Josephson energy to charging energy ratio up to about 300, the operation point of the qubit is shifted into the phase regime, where the Josephson phase constitutes the good quantum number and therefore describes the state of the system.

The price that has to be paid to gain the insensitivity to charge noise is a reduction of the anharmonicity of the qubit. As the transmon can be regarded as a harmonic oscillator, possessing a slightly non-equidistant energy level splitting, it is not a real two-level quantum system. It is therefore crucial to sustain a large enough residual anharmonicity of the transmon, which allows to assign the two fundamental qubit states to well defined distinct energy levels and thereby operate it as a qubit. In general, this is possible as long as the excitation peak broadening, roughly corresponding to the inverse dephasing time of the qubit, is smaller than the absolute anharmonicity of the transmon.

As the charge noise sensitivity decreases with higher algebraic complexity compared to the loss in anharmonicity, a good compromise can be found when designing a transmon qubit.

The employed microstrip design features several advantages compared to the commonly used coplanar structure. As the reference ground potential of the center strip is fairly distant, electric fields are small, leading to a strong reduction of loss, especially at surface oxides. Furthermore, field lines are mainly focussed into the substrate by the ground plane of the microstrip, where nearly no defect states, potentially contributing to loss, exist. This is why the geometry is often called “2.5d”.

While the microstrip design is a relatively easy and elegant approach to design a transmon CQED system, dimensions are in general larger than in a coplanar structure, which is a drawback when it comes to scalability or even the implementation of a many qubit printed circuit system.

In the present work, a transmon CQED system is designed and simulated to start with. The geometry features four mutually frequency detuned $\frac{\lambda}{2}$-resonators, each capacitively coupled to a transmon qubit. The design allows for frequency multiplexed simultaneous qubit readout and provides good statistics of qubit parameters.

Tunability of the transmon qubits is enabled by the implementation of a split Josephson junction forming a dc-SQUID loop. The effective critical current and therefore the qubit frequency is controlled by external magnetic flux.

Sample preparation is done by aluminum sputter deposition and optical lithography. A major challenge in preparing the qubit samples investigated in the present work is the fabrication of high quality Josephson junctions. Since Josephson junction fabrication with the present setup was not an available technology in the group before, parameters in the cleanroom and particularly for the sputter deposition tool needed to be optimized. During that process, several mechanical changes of the equipment were necessary until the desired behaviour could be observed.

In the course of optimizing Josephson junctions, aluminum film quality and in particular its surface roughness were investigated. A smooth surface allows for a good quality interface between electrode and oxide barrier which is ultimately required for a high quality Josephson junction. The surface roughness is investigated by means of atomic force microscopy (AFM) measurements.

Josephson junction transport measurements are presented, measured at room temperature as well as at cryogenic temperatures.

The characteristic non-ohmic behaviour of the current-voltage characteristic at room temperature and a good scaling of the Josephson junction sheet resistance with its area is observed. A good accordance of the resistance-area product of the prepared Josephson junctions with the literature expectation for the applied oxygen exposure is demonstrated.

The low-temperature transport characteristic of the prepared Josephson junction complies with the theoretical prediction and the underdamped nature of the fabricated Josephson junctions is verified.

Investigation of the microstrip resonators demonstrates that the resonance frequencies comply with the designed values apart from a small systematic shift towards lower frequencies. The extracted single photon internal quality factor, obtained in a complex circle fit, is smaller than expected, showing the potential in improving aluminum film quality. According to the expectation, it is demonstrated to be independent of the applied microwave power within the single photon regime.

Spectroscopic qubit measurements unambiguously provide evidence of a quantum system and the existence of a transmon qubit.

Performing a flux bias sweep, a clear oscillation of the resonator frequency can be observed. This is due to the close proximity of the transmon to the resonator in frequency and the effect is given rise by a repelling of levels as can be observed in an avoided level crossing. The oscillation period exactly matches the current corresponding to one flux quantum, confirming the functioning of the split Josephson junction.

Definite proof for the quantum nature of the transmon qubit is given by the observation of distinct transition peaks that can be unambiguously assigned to transmon transitions. The driving power dependence of the peak height and width is in perfect accordance with the expectation.

From the excitation peak broadening of the fundamental qubit transition, the dephasing time of the transmon can be estimated to be $0.13\,\mu$s. The relaxation time of the qubit is expected to be in the same range and therefore agrees with the prediction from the simulation.

The observation of the ac-Stark shift of the fundamental qubit transition frequency indicates the validity of the underlying Jaynes-Cummings Hamiltonian.

A qubit spectrum explicitly gives the tunable frequency range of the transmon by measuring the dispersive shift at a driving frequency dependent on external magnetic flux. The observed periodicity matches the one of the resonator signal and the spectrum is fitted to the theoretical expectation.

In a logical subsequent step, spectroscopic qubit measurements performed in this work could be further substantiated by measurements in the time domain. While most spectroscopic measurement techniques have their analogue in the time domain, the mentioned standard experiments like Rabi and Ramsey experiments can be performed to obtain precise information about the transmon´s dynamical behaviour.

Due to the comparatively large area Josephson junctions, the present sample is a suitable candidate to study and analyse the potentially large number of two-level systems (TLS) in the oxide barriers.

Implementing a slightly modified chip design with two or more weakly detuned qubits being coupled to the same resonator promises interesting physics, as the qubits can be addressed independently by individual manipulation tones. In this way, entangled qubit states can be created, which opens up the possibility of performing multi-qubit gate operations, representing the most primitive form of quantum computation. An elegant scheme to implement such a multi-plexed simultaneous qubit manipulation and readout with one arbitrary waveform generator was demonstrated recently [Jer13].

Another intriguing possibility to explore new physics within close reach is the coupling of two or more resonators to a single qubit. This offers the opportunity to create entangled single photon states, mediated and controlled by the common qubit. In the extreme case of many resonators, this corresponds to a bosonic bath, coupled to a single fermionic quantum system, being the qubit. Such a system, constituting a quantum simulator is of special interest also from the theoretical point of view, since the validity of complex theoretical models can be investigated. An experimental implementation is proposed in [Hou12] for instance.

Decreasing the overlap area of the Josephson junctions by employing electron beam lithography directly translates into an enhancement of the qubit´s coherence behaviour. Together with a weaker coupling between the readout resonators and the feedline, to avoid running into the Purcell limitation of the relaxation time, this promises a huge potential for a high quality long-lived transmon qubit that can compete with similar planar architectures.

Such a transmon qubit, whose properties can quickly be adjusted depending on the demands of the particular circuit, is a basic module for a great variety of possible applications to investigate intriguing physics and ultimately the laws of nature.

References

[Abr61] A. Abragam: *The Principles of Nuclear Magnetism.* Oxford University Press, Glassgow (1961)

[Amb63] V. Ambegaokar and A. Baratoff: *Tunneling between superconductors.* Phys. Rev. Lett. **10**, 486 (1963)

[Ann11] J. F. Annett: *Supraleitung, Suprafluidität und Kondensate.* Oldenbourg Verlag, München (2011)

[AsMe76] N. W. Ashcroft and N. D. Mermin: *Solid State Physics.* International Edition. Saunders Company (1976)

[Asl65] L. G. Aslamazov and A. I. Larkin, Pis´ma Zh. Eksp. Teor. Fiz. **48**, 976 (1965)

[Ast64] A. V. Astin, edited by M. Abramowitz and I. A. Stegun: *Handbook of Mathematical Functions with Formulas, Graphs, and Mathematical Tables.* National Bureau of Standards, Washington, D.C. (1964)

[Bar57] J. Bardeen, L. N. Cooper, and J. R. Schrieffer: *Theory of Superconductivity.* Phys. Rev. **108**, 5 (1957)

[Bar09] R. Barends: *Photon-detecting superconducting resonators.* Ph.D. thesis, Technische Universiteit Delft (2009)

[Bar13] R. Barends, J. Kelly, A. Megrant, D. Sank, E. Jeffrey, Y. Chen, Y. Yin, B. Chiaro, J. Mutus, C. Neill, P. O'Malley, P. Roushan, J. Wenner, T. C. White, A. N. Cleland, and J. M. Martinis: *Coherent Josephson qubit suitable for scalable quantum integrated circuits.* Phys. Rev. Lett. **111**, 080502 (2013)

[Bea01] R. Beals, H. Buhrman, R. Cleve, M. Mosca, and R. de Wolf: *Quantum Lower Bounds by Polynomials.* Journ. of the ACM **48**, 778 (2001)

[Ben84] C. H. Bennett and G. Brassard: *Quantum cryptography: Public key distribution and coin tossing.* Proceedings of the IEEE International Conference on Computers, Systems and Signal processing, Bangalore, India (1984)

[Bla04] A. Blais, R. Huang, A. Wallraff, S. M. Girvin, and R. J. Schoelkopf: *Cavity quantum electrodynamics for superconducting electrical circuits: An architecture for quantum computation.* Phys. Rev. A **69**, 062320 (2004)

[Bri70] W. F. Brinkman, R. C. Dynes, and J. M. Rowell: *Tunneling Conductance of Asymmetrical Barriers.* Journ. of Appl. Phys. **41**, 1915 (1970)

[Cla08] J. Clarke and F. K. Wilhelm: *Superconducting quantum bits.* Nature **453**, 1031 (2008)

[Coo56] L. N. Cooper, Phys. Rev. **104**, 1189 (1956)

[Cri91] M. D. Crisp: *Jaynes-Cummings model without the rotating-wave approximation.* Phys. Rev. A **43**, 5 (1991)

[Deu85] D. Deutsch: *Quantum theory, the Church-Turing principle and the universal quantum computer.* Proc. R. Soc. London A 400, **97** (1985)

[Dev92] M. H. Devoret, D. Esteve, and C. Urbina: *Single-electron transfer in metallic nanostructures.* Nature **360**, 547 (1992)

[Dev95] M. H. Devoret, edited by S. Reynaud, E. Giacobino, and J. Zinn-Justin: *Quantum fluctuations in electrical circuits (Les Houches, Session LXIII).* Elsevier Science, 351 (1995)

[Dev13] M. H. Devoret and R. J. Schoelkopf: *Superconducting Circuits for Quantum Information: An Outlook.* Science **339**, 1169 (2013)

[DiV00] D. P. DiVincenzo: *The Physical Implementation of Quantum Computation.* Fortschr. d. Phys. **48**, 771 (2000)

[Dre03] Dressler® HF-Technik GmbH: CESAR™ Generator Model 136. User Manual (2003)

[Ens00] C. Enss and S. Hunklinger: *Tieftemperaturphysik.* Springer-Verlag, Berlin, Heidelberg, New York (2000)

[Fey65] R. P. Feynman, R. B. Leighton, and M. Sands: *The Feynman Lectures on Physics.* Addison-Wesley, Reading (1965)

[Fey82] R. P. Feynman: *Simulating Physics with Computers.* Int. J. Theor. Phys. **21**, 467 (1982)

[Gao08] J. Gao: *The physics of superconducting microwave resonators.* Ph.D. thesis, California Institute of Technology, Pasadena (2008)

[Gin50] V. L. Ginzburg and L. D. Landau, Zh. Eksp. Teor. Fiz **20**, 1064 (1950)

[Gol97] E. Goldobin: *GoldExI.* Data acquisition software for superconductors and Josephson junctions. Version 3.11 (1997)

[Gop08] M. Göppl, A. Fragner, M. Baur, R. Bianchetti, S. Filipp, J. M. Fink, P. J. Leel, G. Puebla, L. Steffen, and A. Wallraff: *Coplanar waveguide resonators for circuit quantum electrodynamics.* Journ. of Appl. Phys. **104**, 113904 (2008)

[Gra91] H. Grabert: *Single charge tunneling: a brief introduction.* Z. Phys. B Cond. Mat. **85**, 319 (1991)

[Gup96] K. C. Gupta: *Microstrip Lines and Slotlines. Second edition.* Artech House Inc., Boston (1996)

[Har06] S. Haroche and J.-M. Raimond: *Exploring the Quantum. Atoms, Cavities, and Photons.* Oxford University Press, Oxford (2006)

[Hor07] I. Horcas, R. Fernandez, J.M. Gomez-Rodriguez, J. Colchero, J. Gomez-Herrero, and A. M. Baro, Rev. Sci. Instrum. **78**, 013705 (2007)

[Hou12] A. A. Houck, H. E. Türeci, and J. Koch: *On-chip quantum simulation with superconducting circuits.* Nature Phys. **8**, 292 (2012)

[Jay63] E. T. Jaynes and F. W. Cummings: *Comparison of Quantum and Semiclassical Radiation Theories with Application to the Beam Maser.* Proc. of the IEEE **51**, 89 (1963)

[Jer13] M. Jerger: *Experiments on Superconducting Qubits Coupled to Resonators.* Ph.D. thesis, Karlsruhe Institute of Technology, Karlsruhe (2013)

[Jos62] B. D. Josephson, Phys. Lett. **1**, 251 (1962)

[Kam11] H. Kammerlingh-Onnes, Comm. Phys. Lab. Univ. Leiden **122**, 124 (1911)

[Kai10] H. Kaiju, K. Kondo, and A. Ishibashi: *Current-Voltage Characteristics in Nanoscale Tunnel Junctions Utilizing Thin-Film Edges.* Jpn. J. Appl. Phys. **49**, 105203 (2010)

[Kan98] B. E. Kane: *A silicon-based nuclear spin quantum computer.* Nature **393**, 133 (1998)

[Kha12] M. S. Khalil, M. J. A. Stoutimore, F. C. Wellstood, and K. D. Osborn: *An analysis method for asymmetric resonator transmission applied to superconducting devices.* J. Appl. Phys. **111**, 054510 (2012)

[Kle95] A. W. Kleinsasser, R. E. Miller, and W. H. Mallison: *Dependence of Critical Current Density on Oxygen Exposure in Nb-AlO_x-Nb Tunnel Junctions.* IEEE Transactions on applied superconductivity **5**, 1051 (1995)

[Kni01] E. Knill, R. Laflamme, and G. J. Milburn: *A scheme for efficient quantum computation with linear optics.* Nature **409**, 46 (2001)

[Koc07] J. Koch, T. M. Yu, J. Gambetta, A. A. Houck, D. I. Schuster, J. Majer, A. Blais, M. H. Devoret, S. M. Girvin, and R. J Schoelkopf: *Charge-insensitive qubit design derived from the Cooper pair box.* Phys. Rev. A **76**, 042319 (2007)

[Laf93] P. Lafarge, P. Joyez, D. Esteve, C. Urbina, and M. H. Devoret: *Two-electron quantization of the charge on a superconductor.* Nature **365**, 422 (1993)

[Lis08] J. Lisenfeld: *Experiments on Superconducting Josephson Phase Quantum Bits.* Ph.D. thesis, Friedrich-Alexander-Universität, Erlangen-Nürnberg (2008)

[Los98] D. Loss and D. P. DiVincenzo: *Quantum computation with quantum dots.* Phys. Rev. A **57**, 120 (1998)

[Man09] V. E. Manucharyan, J. Koch, L. I. Glazman, and M. H. Devoret: Fluxonium: *Single Cooper-Pair Circuit Free of Charge Offsets.* Science **326**, 113 (2009)

[Maz04] B. A. Mazin: *Microwave Kinetic Inductance Detectors.* Ph.D. thesis, California Institute of Technology, Pasadena (2004)

[McC68] D. E. McCumber: *Effect of ac impedance on dc voltage-current characteristics of superconductor weak-link junctions.* Journ. of Appl. Phys. **39**, 3113 (1968)

[Mic12] MicroChemicals GmbH: *Photolithography. Theory and Application of Photoresists, Etchants and Solvents.* Ulm (2012)

[Mei33] W. Meissner and R. Ochsenfeld, Naturwiss. **21**, 787 (1933)

[Nak99] Y. Nakamura, Yu. A. Pashkin, and J. S. Tsai: *Coherent control of macroscopic quantum states in a single-Cooper-pair box.* Nature **398**, 786 (1999)

[Nor06] C. Nordling and J. Österman: *Physics Handbook. For Science and Engineering.* Studentlitteratur AB, edition 8:5, Lund (2006)

[Ohr02] M. Ohring: *Materials Science of Thin Films. Deposition and Structure. Second Edition.* Academic Press, San Diego (2002)

[Pai10] H. Paik and K. D. Osborn: *Reducing quantum-regime dielectric loss of silicon nitride for superconducting quantum circuits.* Appl. Phys. Lett. **96**, 072505 (2010)

[Poz98] D. M. Pozar: *Microwave Engineering. Second edition.* John Wiley & Sons, Inc., New York, Chichester, Weinheim, Brisbane, Singapore, Toronto (1998)

[Pro13] S. Probst, F. B. Song, P. A. Bushev, A. V. Ustinov, and M. Weides: *Efficient and reliable analysis of noisy complex scattering resonator data for superconducting quantum circuits.* Publ. in preparation (2013)

[Pur46] E. M. Purcell: *Spontaneous Emission Probabilities at Radio Frequencies.* Phys. Rev. **69**, 681 (1946)

[Rab38] I. I. Rabi, J. R. Zacharias, S. Millman, and P. Kusch: *A New Method of Measuring Nuclear Magnetic Moment.* Phys. Rev. **53**, 318 (1938)

[Ram49] N. F. Ramsey: *A New Molecular Beam Resonance Method.* Phys. Rev. **76**, 996 (1949)

[Rig12] C. Rigetti, J. M. Gambetta, S. Poletto, B. L. T. Plourde, J. M. Chow, A. D. Córcoles, J. A. Smolin, S. T. Merkel, J. R. Rozen, G. A. Keefe, M. B. Rothwell, M. B. Ketchen, and M. Steffen: *Superconducting qubit in a waveguide cavity with a coherence time approaching 0.1 ms.* Phys. Rev. B **86**, 100506 (2012)

[Rod07] D. L. Rode, V. R. Gaddam, and J. H. Yi: *Subnanometer surface roughness of dc magnetron sputtered Al films.* Journ. of Appl. Phys. **102**, 024303 (2007)

[Sak68] J. J. Sakurai: *Modern Quantum Mechanics, Revised Edition.* Addison-Wesley Publishing Company (1994)

[San13] M. Sandberg, M. R. Vissers, T. A. Ohki, J. Gao, J. Aumentado, M. Weides, and D. P. Pappas: *Radiation-suppressed superconducting quantum bit in a planar geometry.* Appl. Phys. Lett. **102**, 072601 (2013)

[Sch11] D. M. Schaefer, P. F. P. Fichtner, M. Carara, L. F. Schelp, and L. S. Dorneles: *Dielectric breakdown in AlO_x tunnelling barriers.* Journ. of Phys. D: Appl. Phys. **44**, 135403 (2011)

[Sch97] V. V. Schmidt, edited by P. Müller, and A. V. Ustinov: *The Physics of Superconductors.* Springer-Verlag, Berlin, Heidelberg (1997)

[Sch05] D. I. Schuster, A. Wallraff, A. Blais, L. Frunzio, R.-S. Huang, J. Majer, S. M Girvin, and R. J. Schoelkopf: *ac Stark Shift and Dephasing of a Superconducting Qubit Strongly Coupled to a Cavity Field.* Phys. Rev. Lett. **94**, 123602 (2005)

[Sch07] D. I. Schuster: *Circuit Quantum Electrodynamics.* Ph.D. thesis, Yale University (2007)

[Sho95] P. W. Shor: *Scheme for reducing decoherence in quantum computer memory.* Phys. Rev. A **52**, 2493 (1995)

[Sho97] P. W. Shor: *Polynomial-time algorithms for prime factorization and discrete logarithms on a quantum computer.* SIAM J. Comput. **26**, 1484 (1997)

[Sim63] J. G. Simmons: *Generalized Formula for the Electric Tunnel Effect between Similar Electrodes Separated by a Thin Insulating Film.* Journ. of Appl. Phys. **34**, 1793 (1963)

[Sim63+] J. G. Simmons: *Electric Tunnel Effect between Dissimilar Electrodes Separated by a Thin Insulating Film.* Journ. of Appl. Phys. **34**, 2581 (1963)

[Sli90] C. P. Slichter: *Principles of Nuclear Magnetic Resonance.* 3. Aufl., Springer Verlag, Berlin Heidelberg New York (1990)

[Son11] Sonnet Software Inc., 100 Elwood Davis Road, North Syracuse, NY 13212 (2011)

[Ste68] W. C. Stewart: *Current-voltage characteristics of Josephson junctions.* Appl. Phys. Lett. **12**, 277 (1968)

[TiSc91] U. Tietze, C. Schenk: *Halbleiter-Schaltungstechnik.* Springer Verlag, Berlin Heidelberg New York (1991)

[Tin04] M. Tinkham: *Introduction to Superconductivity. Second edition.* Dover, United States of America (2004)

[Vio02] D. Vion, A. Aassime, A. Cottet, P. Joyez, H. Pothier, C. Urbina, D. Esteve, and M. H. Devoret: *Manipulating the Quantum State of an Electrical Circuit.* Science **296**, 886 (2002)

[Vis10] M. R. Vissers, J. Gao, D.S. Wisbey, D.A. Hite, C. C. Tsuei, A. D. Corcoles, M. Steffen, and D. P. Pappas: *Low loss superconducting titanium nitride coplanar waveguide resonators.* Appl. Phys. Lett. **97**, 232509 (2010)

[Wal04] A. Wallraff, D. I. Schuster, A. Blais, L. Frunzio, R.-S. Huang, J. Mayer, S. Kumar, S. M. Girvin, and R. J. Schoelkopf: *Strong coupling of a single photon to a superconducting qubit using circuit quantum electrodynamics.* Nature **431**, 162 (2004)

[Wan09] H. Wang, M. Hofheinz, J. Wenner, M. Ansmann, R. C. Bialczak, M. Lenander, Erik Lucero, M. Neeley, A. D. O'Connell, D. Sank, M. Weides, A. N. Cleland, and John M. Martinis: *Improving the coherence time of superconducting coplanar resonators.* Appl. Phys. Lett. **95**, 233508 (2009)

[Was04] K. Wasa, M. Kitabatake, and H. Adachi: *Thin film materials technology. Sputtering of Compound Materials.* William Andreq Inc., Norwich, NY; Springer-Verlag, Heidelberg (2004)

[Wen05] G. Wendin and V. S. Shumeiko: *Superconducting Quantum Circuits, Qubits and Computing.* arXiv:cond-mat/0508729 (2005)

[Wol13] Wolfram Mathematica 9 Documentation center: *Mathieu and Related Functions*, *http://reference.wolfram.com/ mathematica/tutorial/MathieuAndRelatedFunctions.html* (07/2013)

A Fabrication parameters

A.1 Process overview

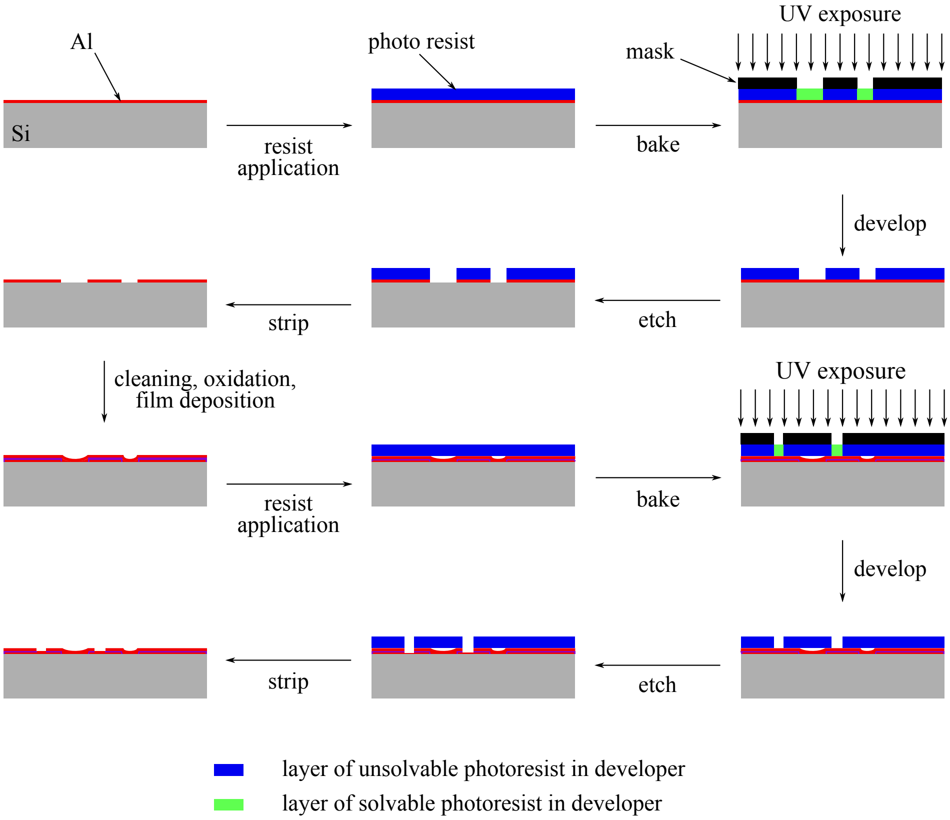

Figure 38: Overview of the applied two-step process for sample preparation. Aluminum layers are depicted in red and the substrate in grey. Photoresist is shown in green if it is soluble in the developer and in blue otherwise.

Figure 38 shows a schematic overview of the two-step optical lithography process applied in this work for sample preparation.

A.2 Aluminum deposition, cleaning and oxidation

Table 3: Argon cleaning in loadlock to remove water residuals

Cleaning power	Loadlock pressure	Cleaning time
20 W	0.13 mbar	120 s

Table 4: Deposition parameters of first aluminum layer M1. Presputtering of the utilized gun takes place with the sample outside the main chamber (MC, 1) to clean the target as well as after inserting the sample (2) to avoid target contamination from the sample transfer.

MC pressure	Sputter power	Presputter time 1	Presputter time 2	Sputter time	Gun
$1.3 \cdot 10^{-3}$ mbar	300 W	120 s	50 s	360 s	extended

Before metal deposition, the substrates are cleaned in the loadlock of the sputter deposition tool to remove water residuals and organic remnants. This process can be regarded as low power etching. The utilized process parameters are summarized in table 3.

The employed parameters for aluminum deposition are given in table 4.

Table 5: Intensive argon cleaning in the loadlock to remove the native oxide. The turbo pump of the loadlock is adjusted half turn open to reduce the pumping power.

Cleaning power	Loadlock pressure	Cleaning time
100 W	$2.3 \cdot 10^{-2}$ mbar	18 min eff. 2 min clean, 30 s pause

Table 6: Deposition parameters of second aluminum layer M2

MC pressure	Sputter power	Presputter time 1	Presputter time 2	Sputter time	Gun
$1.3 \cdot 10^{-3}$ mbar	300 W	120 s	50 s	240 s	extended

Table 7: Oxidation exposure

Static pressure	Oxidation time
31.5 mbar	60 min

After structuring the first aluminum layer of the sample ex-situ, the native surface oxide needs to be removed before controlled reoxidation. This is done in an intensive cleaning step in the loadlock of the sputter deposition tool. As indicated in table 5, the plasma is switched off every two minutes for 30 seconds to prevent the sample from heating up.

Deposition parameters for the second aluminum layer given in table 6 match those from table 4 apart from the adjusted sputtering time.

Oxidation exposure is given in table 7. The loadlock turbo pump is switched off and slowed down by the oxygen streaming into the chamber. This allows to evacuate the loadlock after oxidation with the turbo pump and respective roughening pump which is suited for pumping reactive gases.

A.3 Resist application

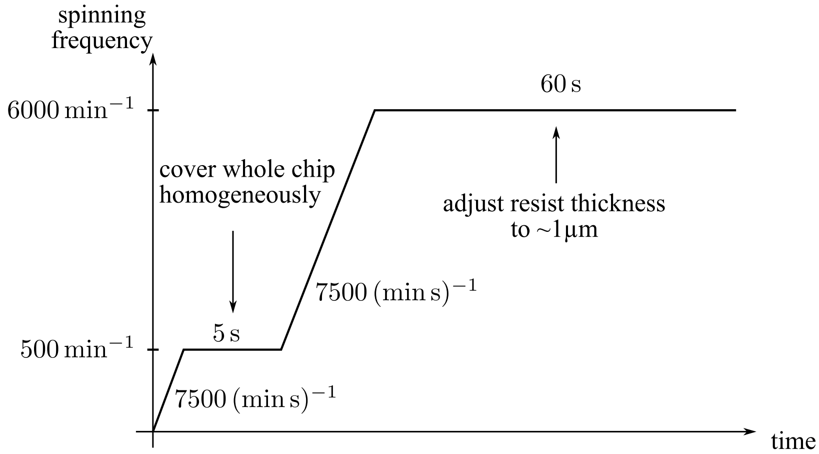

Figure 39: Schematic graph showing the two ramps during resist application. In a first step, the resist is distributed over the whole chip homogeneously, while the thickness is adjusted in a longer subsequent step.

Table 8: Parameters for resist application using the spin coater

Resist	Ramp speed, time	Full speed, time	Acceleration	Hot plate temperature, time
AZ5214E	500 rpm, 5 s	6000 rpm, 60 s	7500 rpm/s	110 °C, 50 s

A.4 Optical lithography

Table 9: Exposure parameters for optical lithography using the mask aligner

Mask	Exposure power	Exposure intensity	Exposure time	Radiation wavelength
chrome/soda	260 W	$5.0\,\frac{\mathrm{mW}}{\mathrm{cm}^2}$	5.5 s	$(360 - 440)$ nm

Table 10: Development

Developer	time
MIF726	50 s

A.5 Resist strip

Table 11: Resist strip

Stripper	Ultrasonic bath time	Ultrasonic bath power	Cleaning
NMP/NEP	5 min	2 (a.u.)	isopropyl H_2O, bidest.

A.6 ICP etching

Table 12: Etching parameters for the inductively coupled plasma reactive ion etch (ICP)

Chamber pressure	Gas flow	RF bias power	ICP power	Chiller temperature
10.0 mTorr	Ar: 20 sccm Cl_2: 2 sccm	100 W $C_1 = 68.9\%$ $C_2 = 57.2\%$	100 W $C_1 = 36.0\%$ $C_2 = 38.6\%$	20 °C

Table 13: Recipe for the etching process

Time	Process
5 min	O_2-clean
5 min	conditioning
$\approx 0.5\,\frac{\text{s}}{\text{nm}}$ in steps of 15 s	main etch
5 min	O_2-clean

Before starting the actual etching process of the sample, the chamber is cleaned with an oxygen plasma and subsequently conditioned with the parameters given in table 12.

Depending on the thickness of the aluminum film to be etched, the etching steps shown in table 13 can be increased up to about 30 s. During these steps, the etching progress can be checked optically.

To guarantee a proper etching behaviour, the surface of the utilized etching wafer needs to be clean and unspoiled.

B Implementation of computer control for the sputter deposition tool

To operate the sputter deposition tool in an effective way and to obtain process reproducibility, a computer control of the relevant instruments is implemented.

The computer control of the radio frequency (RF) source Cesar136 [Dre03] is mainly used in the intensive cleaning process mentioned in sections III.2.1 and III.2.3. It allows to introduce regular pauses in the cleaning process, continuously check the process for potentially occurring errors and logging of the relevant parameters.

The python script used for the cleaning process runs on pi-us56 and is called

```
/home/evaporate/devel/evaporate/scripts/er_cesar_control02.py
```

Log files are written to

```
/home/evaporate/devel/evaporate/logs/
```

Pressures of the loadlock and the main chamber are read out every few seconds and written in a separate log file in the same folder. The pressure logging script is called

```
/home/evaporate/devel/evaporate/scripts/er_pressure_control.py
```

The pressure log files of the format

```
pressurelogDDMMYYYY.txt
```

are copied to the group server pi-us28 two times a month by means of a *cronjob* and the respective shell script

```
/home/evaporate/bin/log_upload.sh
```

running on pi-us56. The location of the log files on pi-us28 is

```
/home/exchange/Fabrication/logfiles/plasma1/
```

The mentioned cronjob also checks for the pressure logging still being executed once per day and automatically restarts the python script after a termination caused by a kernel reboot for instance.

An instant remote pressure readout is provided by the script

```
/home/evaporate/devel/evaporate/scripts/er_pressure_readout.py
```

also running on pi-us56.

With the installation of the new gas handling system, the MKS mass flow controller is included in the computer control. Directly executing the instrument library, located at

```
/home/evaporate/devel/evaporate/lib/er_MKS_647C.py
```

sets the controller to its defaults adapted to the setup in use. Additionally, remote setting the gas flow of all channels as well as reading out the Baratron pressure is supported.

Acknowledgements

I want to express my gratitude to Prof. Dr. Alexey V. Ustinov for giving me the opportunity to work on the intriguing topic of my master thesis in his group. I am thankful for getting the chance to participate at the ski seminar, the DPG conference in Regensburg and the doctoral training session “Frontiers of Condensed Matter” in Les Houches, France.

I am grateful to Prof. Dr. Gerd Schön for being the second reviewer of this master thesis.

My special thanks go to Dr. Martin Weides. As my supervisor, he was supporting me to any time in instructive and enlightening discussions and was a great contact for any kind of question that arose. Apart from providing technical scientific support, he also taught me general scientific working methods and how to approach scientific problems in general. I appreciate that he led my project into the right direction whenever necessary while allowing me to work independently. Furthermore I am thankful for careful proofreading of this thesis.

I want to thank Dr. Hannes Rotzinger for listening to different kinds of problems, giving me many very useful hints and stimulations concerning my project and teaching me a professional way of working. He gave me a great introduction on how to operate Unix and python programming and supported me when it came to implementing the computer control of the sputter deposition tool. In addition, I enjoyed his open ear concerning problems going beyond physics.

I am very thankful to Lucas Radtke who is doing an incredible job in the cleanroom and was helping me throughout my thesis in every respect he could. He contributed to a decisive extent to the success of this work.

I want to specially thank Dr. Oleksandr Lukashenko for cooling down the dilution refrigerator and generously keeping his countenance in any occurring critical situation. Throughout my work, he was a very competent contact for any questions concerning the cryogenic setup.

I am thankful to Roland Jehle who was a great support whenever it came to electronics problems or questions.

My thanks go to Dr. Jürgen Lisenfeld and Dr. Michael Marthaler for interesting and very useful theoretical discussions.

I want to thank Sebastian Probst for providing the circle fit algorithm.

I am thankful to Saskia Meißner for taking SEM pictures of the fabricated tunnel junctions.

I want to thank all members of the group for the friendly and pleasant atmosphere, especially my office mates in room 410.

Finally I would like to thank my mother for her support and her willingness to help with any problem during this work.